DOT/FAA/TCTT-22/33

Federal Aviation Administration
William J. Hughes Technical Center
Aviation Research Division
Atlantic City International Airport
New Jersey 08405

Investigations into Ductile Fracture and Deformation of Metals Under Combined Quasi-static Loading and Under Extremely High-rate Compressive Impact Loading

October 2020

Technical Thesis

The research described in this report was funded by the FAA as part of its mission to improve aircraft safety. The views and opinions expressed are those of the author alone and do not necessarily represent the views of the FAA. The FAA assumes no liability for the contents or use thereof. The FAA has not edited or modified the contents of the report in any manner.

U.S. Department of Transportation
Federal Aviation Administration

NOTICE

This document is disseminated under the sponsorship of the U.S. Department of Transportation in the interest of information exchange. The U.S. Government assumes no liability for the contents or use thereof. The U.S. Government does not endorse products or manufacturers. Trade or manufacturers' names appear herein solely because they are considered essential to the objective of this report. The findings and conclusions in this report are those of the author(s) and do not necessarily represent the views of the funding agency. This document does not constitute FAA policy. Consult the FAA sponsoring organization listed on the Technical Documentation page as to its use.

This report is available at the Federal Aviation Administration William J. Hughes Technical Center's Full-Text Technical Reports page: actlibrary.tc.faa.gov in Adobe Acrobat portable document format (PDF).

Form DOT F 1700.7 (8-72) Reproduction of completed page authorized

1. Report No.	2. Government Accession No.	3. Recipient's Catalog No.
DOT/FAA/TCTT-22/33		

4. Title and Subtitle	5. Report Date
Investigations into ductile fracture and deformation of metals under combined quasi-static loading and under extremely high-rate compressive impact loading	October 2022
	6. Performing Organization Code ANG-E282
7. Author(s) Nathan Spulak	8. Performing Organization Report No. DOT/FAA/TCTT-22/33
9. Performing Organization Name and Address Federal Aviation Administration William J. Hughes Technical Center Aviation Research Division Atlantic City International Airport, NJ 08405	10. Work Unit No. (TRAIS) 11. Contract or Grant No.
12. Sponsoring Agency Name and Address Federal Aviation Administration William J. Hughes Technical Center Aviation Research Division Atlantic City International Airport, NJ 08405	13. Type of Report and Period Covered Technical Thesis 14. Sponsoring Agency Code ANG-E2

15. Supplementary Notes
Presented in Partial Fulfillment of the Requirements for the Degree Doctor of Philosophy in the Graduate School of The Ohio State University

16. Abstract

Materials experiencing impact loading deform under complex three dimensional states of stress and at high strain rates. Accurately simulating impact events using finite element modeling requires material models capable of depicting the material behavior under these same conditions. In order to create accurate material models, this material behavior must first be determined experimentally. It is of particular interest to determine the equivalent plastic fracture strain at stress states consisting of in-plane biaxial tension and out-of-plane compression, and the plastic stress strain response at strain rates on the order of 10^4 s^{-1}. Both of these conditions are found during impact loading, and are outside the scope of current testing techniques. A new test technique is used to investigate Aluminum 2024, Titanium 6Al-4V, and Inconel 718 under in-plane biaxial tension and out-of-plane compression. The test consists of a small spherical or elliptical punch that is advanced into a thin specimen plate to induce in-plane biaxial tension on the back surface of the specimen. A second plate of an appropriate material is placed against the back surface of the specimen plate during loading in order to create out-of-plane compression. The equivalent plastic fracture strain at these stress states is determined from the experimental data and simulations using the commercial finite element software LS-DYNA. The same materials mentioned above are also tested using a modified, direct impact split-Hopkinson bar testing technique to induce strain rates greater than 10^4 s^{-1}. For these tests, a small cylindrical specimen is placed in contact with the end of a larger cylindrical bar. The specimen is then impacted with a free flying cylindrical projectile to compress the specimen at a high rate of deformation. The stress-strain response of the material at these high strain rates is then investigated from the experimental data and in conjunction with LS-DYNA finite element simulations.

17. Key Words	18. Distribution Statement
	This document is available to the U.S. public through the National Technical Information Service (NTIS), Springfield, Virginia 22161. This document is also available from the Federal Aviation Administration William J. Hughes Technical Center at actlibrary.tc.faa.gov.

19. Security Classif. (of this report)	20. Security Classif. (of this page)	21. No. of Pages	19. Security Classif. (of this report)
Unclassified	Unclassified	165	Unclassified

Investigations into ductile fracture and deformation of metals under combined quasi-static loading and under extremely high-rate compressive impact loading

Dissertation

Presented in Partial Fulfillment of the Requirements for the Degree Doctor of Philosophy in the Graduate School of The Ohio State University

By

Nathan Spulak, M.S.

Graduate Program in Mechanical Engineering

The Ohio State University

2022

Dissertation Committee:

Dr. Amos Gilat, Advisor

Dr. Jeremy Seidt

Dr. Prasad Mokashi

Abstract

Materials experiencing impact loading deform under complex three dimensional states of stress and at high strain rates. Accurately simulating impact events using finite element modeling requires material models capable of depicting the material behavior under these same conditions. In order to create accurate material models, this material behavior must first be determined experimentally. It is of particular interest to determine the equivalent plastic fracture strain at stress states consisting of in-plane biaxial tension and out-of-plane compression, and the plastic stress-strain response at strain rates on the order of 10^4 s^{-1}. Both of these conditions are found during impact loading, and are outside the scope of current testing techniques.

A new test technique is used to investigate Aluminum 2024, Titanium 6Al-4V, and Inconel 718 under in-plane biaxial tension and out-of-plane compression. The test consists of a small spherical or elliptical punch that is advanced into a thin specimen plate to induce in-plane biaxial tension on the back surface of the specimen. A second plate of an appropriate material is placed against the back surface of the specimen plate during loading in order to create out-of-plane compression. The equivalent plastic fracture strain at these stress states is determined from the experimental data and simulations using the commercial finite element software LS-DYNA.

The same materials mentioned above are also tested using a modified, direct impact split-Hopkinson bar testing technique to induce strain rates greater than 10^4 s^{-1}. For these tests, a small cylindrical specimen is placed in contact with the end of a larger cylindrical bar. The specimen is then impacted with a free flying cylindrical projectile to compress the specimen at a high rate of

deformation. The stress-strain response of the material at these high strain rates is then investigated from the experimental data and in conjunction with LS-DYNA finite element simulations.

Dedication

Dedicated to my family, who has always been there for me.

Acknowledgements

Many people have helped me to reach this point in my life, to whom I am extremely grateful and indebted. I would like to thank my mother, Patricia, for her love, support, and encouragement. I would like to thank my sister Grace for teaching me what resolve and determination look like; my sister Mary, for being an example of patience and humble kindness; my brother Kevin, for teaching me how necessary it is to respect and help others; and my sister Emily for showing me how to follow my passions and dreams. I would also like to thank my grandfather, Richard Yeggy, who taught me the importance of courage and protecting those we love. His calm guidance throughout my life has been instrumental in forming me into who I am today.

My advisor, Dr. Amos Gilat, has been incredibly supportive of me during my time at Ohio State, and it has been an honor to work with him. Dr. Jeremy Seidt has also been incredibly supportive as a mentor and I am grateful for the advice and help he has given me. I would also like to thank my many colleagues in the Dynamic Mechanics of Materials Laboratory: Stuart Brand, Kelton Rieske, Jarrod Smith, Mark Konieczny, Peiyu Yang, Jeremy Massie, and Bryson Knott. These researchers and fellow students have been immensely helpful through their technical expertise, advice, and friendship.

This research was supported by the Federal Aviation Administration, in collaboration with the National Aeronautics and Space Administration, George Mason University, and the University of Dayton. I would like to thank the many members of the FAA Aerospace Working Group whose support and collaboration made this research possible: William Emmerling, Dr. Daniel Cordasco, Dr. Tom Vasko, Dr.Michael Pereira, Charles Ruggeri, Duane Revilock, Dr.

Kelly Carney, Paul Du Bois, Dr. Cing-Dao (Steve) Kan, Dr. C.K. Park, Stefano Dolci, and Dr. Robert Lowe.

Vita

2012……St. Pius X High School

Albuquerque, NM

2016……B.S. Mechanical Engineering

The University of Notre Dame

2016-present……Graduate Research Associate

Dynamic Mechanics of Materials Laboratory

Department of Mechanical and Aerospace Engineering

The Ohio State University

2020……M.S. Mechanical Engineering

The Ohio State University

Publications

Spulak, N., Lowe, R. L., Seidt, J. D., Gilat, A., Park, C. K., and Carney, K. S.. Ductile fracture under in-plane biaxial tension and out-of-plane compression. *International Journal of Solids and Structures*, *202*, pp. 234-242. 2020.

Spulak, N., Lowe, R., Seidt, J. and Gilat, A.. Failure Testing Under In-Plane Biaxial Tension and Out-of-Plane Compression. In *Fracture, Fatigue, Failure and Damage Evolution, Volume 6* Editors: Carroll, J., Shuman, X., Beese, A.M., Berke, R.B., Pataky, G.J. (Eds.), pp. 17-19, Springer, Cham., 2019

Gilat, A., Seidt, J.D., Spulak, N., and Smith, J. New Testing in Support of LS-DYNA MAT 224 Material Model. 12th European LS-DYNA Conference, Koblenz, Germany, May 2019.

Spulak, N., Foeldi, S., Koller, M., Niemier, M., Schmiedeler, J. and Cserey, G.. Wrist pulse detection and analysis using three in-line sensors and linear actuators. In *CNNA 2016; 15th International Workshop on Cellular Nanoscale Networks and their Applications*. 2016.

Fields of Study

Major Field: Mechanical Engineering

Specializations: Experimental Mechanics, Finite Element Analysis, Computational Mechanics, Plasticity, Ductile Fracture, Dynamic Behavior of Materials

Table of Contents

List of Tables

List of Figures

Chapter 1 Introduction

1.1 Significance of the Problem

In 1989, a DC-10 commercial aircraft at cruising altitude experienced an uncontained engine blade out event. Multiple fragments from the engine penetrated through the engine casing and damaged the redundant flight control systems, resulting in the loss of the hydraulic systems. The resulting crash caused the deaths of 112 passengers [1]. In response, the Federal Aviation Administration's (FAA) Uncontained Engine Debris Mitigation program was created with the goal of preventing uncontained blade out events [2]. However the problem is far from solved as these events still occur with fatal results. In 2018 debris from an engine blade out event impacted the fuselage of a Boeing 737, resulting in the death of a passenger after they were partially sucked out of the aircraft through the damaged section [3]. In 2021, a Boeing 777 experienced an engine blade out event caused by fatigue failure, generating significant debris that fell over heavily populated areas of Denver, Colorado [4]. Damage from such incidents is show in Figure 1.1 below.

Federal Aviation Regulation FAR/JAR 25.903(d)(1) states that "design precautions must be taken to minimize the hazards to the airplane in the event of an engine rotor failure" [5]. In order to effectively design engine components that are capable of preventing debris from penetrating through the engine casing and damaging other critical systems on the aircraft or from causing direct injury to the passengers, it is necessary to have accurate material models of the components involved. Blade out events are complex, involving debris of numerous shapes and sizes traveling at various speeds, all at elevated temperatures. Therefore any material model used to simulate these

events must be able to reflect the strain rate dependency, thermal softening, and the effect that different stress states have on the plasticity and fracture response.

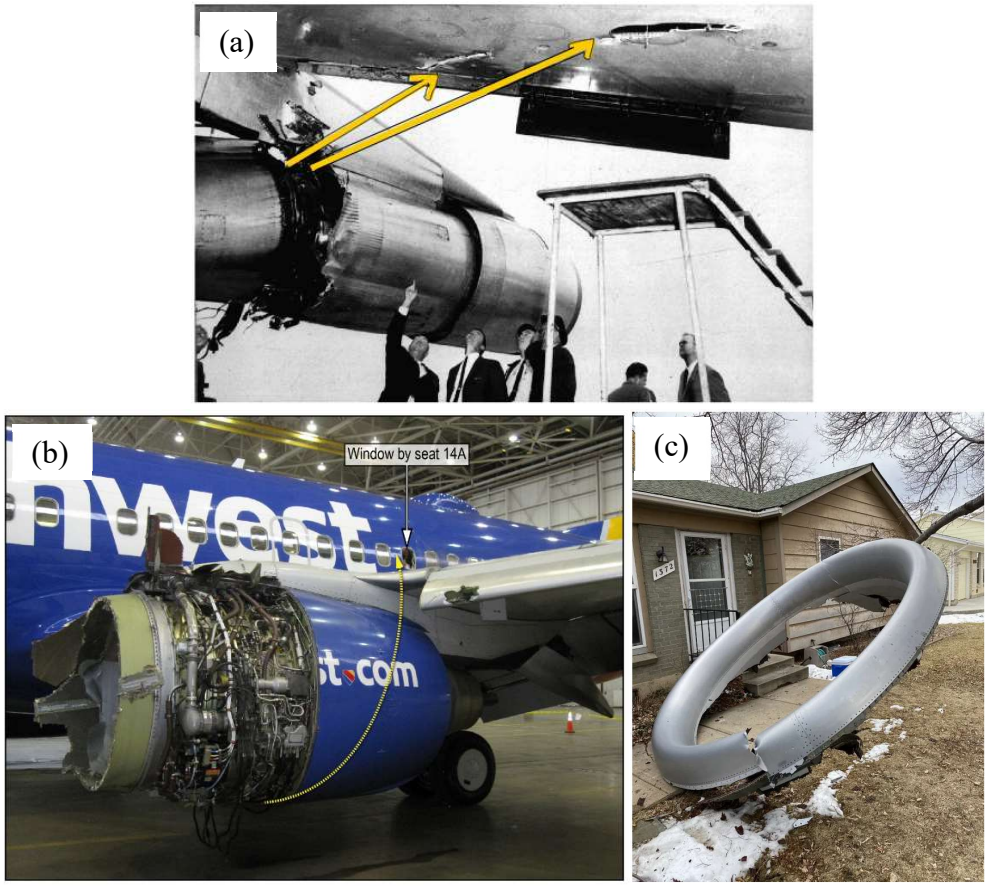

Figure 1.1 Damage from engine blade out events showing (a) damage to wing [6], (b) damage to fuselage [3], and (c) debris generated that fell over residential areas [7]

One such material model capable of capturing the complexity involved in an engine blade out event is LS-DYNA material model *MAT_224, a tabulated Johnson-Cook material model that interpolates between tabulated test data [8]. In order for this model to correctly predict the material response, it requires the input of accurate experimental data. The stress-strain behavior of a material must be experimentally determined at numerous strain rates and temperatures, and likewise the equivalent plastic fracture strain must be determined over a wide range of stress states.

This model has recently been developed by the FAA Aerospace Working Group (AWG) [9][9][11]. Using this material model to simulate projectiles impacting into flat plates revealed that the simulated material was failing prematurely at states of in-plane tension and out-of-plane compression [12]. However, no previous independent tests have been done at these stress states due to a lack of a viable testing techniques. In addition, no tests with strain rates higher than 10^4 s^{-1} were performed, yet actual blade out events may see strain rates of that magnitude. Therefore, in order to increase the accuracy of the *MAT_224 material model, development and implementation of new testing techniques that capture these stress states and higher strain rates are necessary.

1.2 Scope and Objectives of this Research

The objective of this research is to determine the strain at fracture under various ratios of in-plane biaxial tension and out-of-plane compression for Aluminum 2024, Titanium 6Al-4V, and Inconel 718. An additional objective is to determine the stress-strain response of each of these materials to compressive loading at strain rates in excess of 10^4 s^{-1}. This data is necessary in order to increase the accuracy of the *MAT_224 material models being created by the FAA's Uncontained Engine Debris Mitigation program.

The experimental program to determine strain to fracture under in-plane biaxial tension and out-of-plane compression consists of punch tests on thin specimen plates of each material. A small spherical or elliptical punch is displaced into the specimen plate to induce in-plane biaxial tension on the back surface of the specimen (opposite the punch). To add out-of-plane compression, a second thin plate of a different material is placed behind the specimen in some tests. The load and displacement of the punch is measured in each test, and cameras are used to capture images of the back surface of the specimen for full field Digital Image Correlation (DIC) analysis to determine

the strain at the fracture point. For tests without an additional backing plate, DIC images are taken continuously during loading. For the tests with a backing plate, there is no optical path to the specimen surface during loading since the backing plate blocks the line of sight to the cameras. Therefore, additional backed tests are performed where the loading is performed in sequential increments and a DIC image of the specimen is taken between each increment.

For testing of materials at strain rates of 10^4 s^{-1} or higher, a modified direct impact split-Hopkinson bar (SHB) experimental technique is used. A small cylindrical compression specimen is placed at one end of a shortened transmitter bar instrumented with strain gages. The specimen is then impacted with a free flying projectile of the same diameter and material as the transmitter bar. The average strain rate across the specimen is dependent on the specimen length and the velocity of the projectile, with nominal strain rates close to 40,000 s^{-1} possible. The force between the specimen and the transmitter bar can be determined from the transmitter bar strain gage voltage output. A high speed digital camera is used to capture images of the test. DIC is used to find the relative displacement between the projectile and transmitter bar, and to determine displacement and strain data on the specimen.

In addition to the experimental portion of this research, numerical analysis is performed using LS-DYNA. In the punch tests, the punch force, punch displacement, strain on the back surface of the specimen, and the time and location of fracture are compared to the finite element analysis (FEA) to determine the accuracy of the simulations and verify the fracture strain found from the experiments. In the modified SHB tests, the measured force between the specimen and transmitter bar, and the displacement and strain on the specimen are compared to FEA simulations to investigate the stress-strain behavior of the specimen at high strain rates.

1.3 Literature Review

It has been shown that material stress-strain response and fracture can be dependent on the applied stress triaxiality [13][14][15], the strain rate [16][17], and the material temperature [18][19]. Johnson and Cook [20] proposed a phenomological material model to describe the plastic stress-strain response of a material and the effect that strain hardening, strain rate, and temperature play on material behavior, as shown in Eq. (1-1):

$$\bar{\sigma} = \left[A + B\left(\bar{\varepsilon}_p\right)^N\right][1 + C\ln(\dot{\varepsilon})][1 - (T_H)^M], \tag{1-1}$$

where $\bar{\sigma}$ is the equivalent true stress, $\bar{\varepsilon}_p$ is the equivalent plastic strain, and $\dot{\varepsilon}$ is the equivalent plastic strain rate. $T_H = \frac{T - T_R}{T_M - T_R}$ is the homologous temperature where T is the temperature, T_R is the reference temperature (usually room temperature), and T_M is the melt temperature. $A, B, C, M,$ and N are tuning parameters that allow for the model to be fitted to test data for a specific material. In Eq. (1-1), the first bracketed term is a hardening function capable of capturing the strain-hardening behavior of a material. The second bracketed term scales the hardening curve to account for strain rate sensitivity, and similarly the third bracketed term scales the hardening curve to account for thermal softening.

Johnson and Cook expanded the plasticity model to include prediction of fracture [20] by the introduction of a damage parameter to account for the effects of the stress triaxiality, strain rate, and temperature on the equivalent plastic fracture strain through the following:

$$D = \sum \frac{\Delta\bar{\varepsilon}}{\bar{\varepsilon}_p^f}, \tag{1-2}$$

$$\bar{\varepsilon}_p^f = [D_1 + D_2\exp(D_3\sigma^*)][1 + D_4\ln(\dot{\varepsilon})][1 + D_5 T_H], \tag{1-3}$$

where D is the damage parameter, $\Delta\bar{\varepsilon}$ is the increment in equivalent plastic strain over one numerical integration cycle, $\bar{\varepsilon}_p^f$ is the equivalent plastic strain at fracture, and $\sigma^* = \frac{\sigma_m}{\sigma_{vm}}$ is the

triaxiality defined as the ratio of the mean stress to the von Mises stress. D_1, D_2, D_3, D_4, and D_5 are tuning parameters. When the damage parameter reaches a value of 1, failure has occurred. Because $\bar{\varepsilon}_p^f$ is a function of the triaxiality, the strain rate, and the temperature, its value can change during the simulation as these variables change. If the triaxiality, strain rate, or temperature change such that $\bar{\varepsilon}_p^f$ increases, the ratio $\frac{\Delta\bar{\varepsilon}}{\bar{\varepsilon}_p^f}$ will be smaller and damage will accumulate more slowly. Conversely if $\bar{\varepsilon}_p^f$ decreases, the damage increment ratio will become larger and damage will accumulate more quickly. This permits the damage model to take the loading history of the material into account when determining when material failure will occur.

Since its introduction, the Johnson-Cook material and fracture models have been widely used. However, these models have several key limitations. As mentioned, Eq. (1-1) is capable of scaling the magnitude of a stress-strain curve to account for strain rate and thermal effects. However, if the material's strain hardening behavior changes due to the strain rate or thermal effects (i.e., the shape of the stress-strain curve changes), this model is not capable of capturing that change. Another limitation is that the fracture model in Eq. (1-3) assumes that the fracture strain will exponentially decrease as triaxiality increases. However, experiments have shown that this is not necessarily the case. In testing of 2024 aluminum, Bao [21] found that the fracture strain decreased as triaxiality changed from a value of $-\frac{1}{3}$ to 0, then began to increase and reached a local peak at a triaxiality of 0.4, before decreasing again at higher triaxialities. Such complexity cannot be captured by the Johnson-Cook model.

To address this issue Bao and Wierzbicki [22] split the triaxiality regime into three sections and fit a separate mathematical curve to each section. Another proposed solution is to take into account the effects of shear by the introduction of a deviatoric state parameter. Barsoum and

Faleskog [23] used a deviatoric state parameter called the Lode parameter, μ, defined by Eq. (1-4), which is based on the principal stresses.

$$\mu = \frac{2\sigma_2 - \sigma_1 - \sigma_3}{\sigma_1 - \sigma_3} \tag{1-4}$$

Wierzbicki et al [24] defined a similar, but not identical, deviatoric state parameter as an alternative Lode parameter, L:

$$L = \frac{27}{2}\frac{J_3}{\sigma_{vm}^3}, \tag{1-5}$$

where J_3 is the third invariant of the deviatoric stress tensor.

These parameters correspond to the applied stress state and the material failure mechanism. The triaxiality describes the relative amount of hydrostatic tension or compression, which determines the rate of void growth and coalescence. The Lode parameter is related to the amount of shear stresses present, which cause internal shearing of the necked material ligaments between voids [25].

When the fracture strain is assumed to be dependent on both the triaxiality and Lode parameter, it is represented as a three dimensional fracture surface. Creation of such a fracture surface requires experimental testing to determine the fracture strain at numerous combinations of triaxiality and Lode parameter values. Examples of such experiments include uniaxial tension, uniaxial compression, torsion, combined tension-torsion or compression-torsion, punch tests and tension tests of axisymmetric round bars [9][22][23][26][27].

Once fracture data has been obtained through experiments, one method of constructing a fracture surface is to fit the experimental data points to underlying mathematical governing equations. Examples of this method include the extended Mohr-Coulomb model and the Hosford-Coulomb model [28][29]. An advantage of this method is that it requires relatively few tests to

calibrate the shape and level of the fracture surface. However, a disadvantage is that the underlying mathematical governing equations cannot capture all the complexities of how the fracture strain changes depending on the stress state, which limits the accuracy of these models. Another approach is to construct a fracture surface by interpolating between tabulated experimental data points, such as is done in LS-DYNA material model *MAT_224 [8]. This approach allows for the creation of a more complex fracture surface to better capture the material behavior. However, it requires extensive testing over a wider range of stress states in order to accurately predict ductile fracture. It is also important to note that *MAT_224 defines triaxiality as $\sigma^* = -\frac{\sigma_m}{\sigma_{vm}}$, (positive triaxiality in compression) which is the opposite sign convention used by many other researchers.

In addition to allowing for the input of a tabulated fracture surface, *MAT_224 also allows for the input of tabulated stress-strain curves at different strain rates and temperatures [8]. Because multiple curves can be added to the model, changes in the shape of the stress-strain curve at different strain rates or temperatures can be captured. This is in contrast to the classical Johnson-Cook model and other similar mathematical models, which only scale the hardening curve up or down and cannot capture changes to the shape of the curve.

In order to calibrate models and account for strain rate sensitivity, materials must be tested at different strain rates. Strain rates of 10^{-4} s^{-1} through 1 s^{-1} can be achieved using hydraulic or servo-hydraulic load frames. Rates on the order of 10^1 through 10^2 s^{-1} can be achieved through the use of a specialized testing device such as a modified split-Hopkinson bar (SHB) apparatus with an elongated transmitter bar [30], while rates on the order of 10^3 s^{-1} can be achieved through conventional SHB experiments [17].

In a conventional SHB compression test, a specimen is placed between two long slender bars, called the incident and transmitter bars. The incident bar is then impacted with a third bar, called the striker bar. This impact generates an elastic compressive strain wave that travels down the incident bar towards the specimen with wave speed $c = \sqrt{\frac{E}{\rho}}$, where E is the elastic modulus and ρ is the density of the incident bar material. When the incident wave impacts the specimen, part of the wave is reflected back in the opposite direction and the remainder of the wave is transmitted through the specimen and into the transmitter bar. The amplitude of the compressive strain wave in the bar can be measured using strain gages, and it is proportional to the velocity of the end of the bar with $\varepsilon_b = \frac{\dot{u_b}}{2c}$. Assuming elastic deformation of the bar, the force in the bar, *F*, can be found using Hooke's law and the definition of engineering stress as the force divided by the bar cross-sectional area, A_b. The velocity of the bar can then be found from the measured force as $\dot{u_b} = \frac{2cF}{EA_b}$, and the average strain rate of the specimen can be found by the difference in velocity of the incident bar, $\dot{u_i}$, and the transmitter bar, $\dot{u_t}$, divided by the specimen gage length L_s such that $\dot{\varepsilon} = \frac{\dot{u_i} - \dot{u_t}}{L_s}$. The strain in the specimen is then found by integrating the strain rate in time [9].

The force on the specimen can be found from the magnitude of the reflected and transmitted strain waves, which should have equal magnitude if the specimen is not accelerating and the forces from the incident and transmitter bar are balanced. The engineering stress of the specimen can then be found by dividing the force by the initial specimen cross-sectional area, and a stress-strain curve for the specimen can be constructed. In addition to using just the elastic wave data to find the engineering strain, recent tests have also utilized high speed photography to capture images for DIC analysis to determine localized displacements and strain on the surface of the specimen.

A limiting factor for the SHB test is that the waves generated in the bars must remain elastic. Because of this, stress-strain data at strain rates greater than 10^3 s^{-1} cannot generally be achieved, since higher strain rates would require higher impact velocities of the striker bar that would exceed the elastic limit and cause plastic deformation of the bars. Dharan [31] proposed a modified SHB experiment where the striker bar is replaced with a free flying projectile in order to achieve strain rates higher than 10^3 s^{-1}, and this technique has since been utilized by Couque [32] to investigate the high strain rate behavior of face centered cubic and body centered cubic materials using elastic wave theory. However, investigations utilizing DIC to determine the localized displacement and strain during direct impact experiments have not previously been performed.

Chapter 2 Experimental Procedures and Techniques

This chapter presents the experimental program used to determine the strain to fracture under stress states of in-plane biaxial tension coupled with out-of-plane compression, and the experimental program used to investigate the plasticity response of materials at strain rates in excess of 10^4 s^{-1}. The experimental procedures, including the loading techniques and optical displacement and strain measurements, are described.

2.1 Material Selection

Test are performed on Aluminum 2024-T351, Titanium 6Al-4V and Inconel 718. These tests are performed as part of the FAA's Uncontained Engine Debris Mitigation program, and therefore the material used is taken from the same batch of plate stock used for previous characterization tests in this program [9][10][33] in order to mitigate the effect of variations in the material composition and performance between different manufacturing batches. The chemical makeup of the aluminum purchased from Kaiser Aluminum, the titanium purchased from Titanium Industries Inc., and the Inconel purchased from Allegheny Ludlum are summarized in Table 2.1, Table 2.2, and Table 2.3, respectively. In addition, the heat treatment of the Inconel 718 is summarized in Table 2.4.

Table 2.1 Chemical Composition of Aluminum 2024-T351

Si	Fe	Cu	Mn	Cr	Zn	Ti	V	Zr	Al
0.08	0.22	4.47	0.59	1.37	0.01	0.18	0.02	0.01	bal

Table 2.2 Chemical Composition of Titanium 6Al-4V

Al	V	Fe	O	C	N	Ti
6.64	4.04	0.13	0.19	0.011	0.006	bal

Table 2.3 Chemical Composition of Inconel 718

C	Mn	P	S	Si	Ni	Cr	Mo	Co	Cu	Al	Ti	Cb	B	Fe	Ta
0.048	0.08	0.008	0.0001	0.072	52.6	18.32	2.87	0.2	0.034	0.54	1.02	4.94	0.0029	9.25	0.01

Table 2.4 Heat Treatment of Inconel 718

Phase	Duration (hrs.)	Description
Temperature Hold	8	Hold at 718°C
Ramp Cool	1.76	Ramp Cool at 55°C/hr
Temperature Hold	8	Hold at 621°C

2.2 Small Diameter Backed Punch Experiments

Small diameter backed punch tests are performed to determine the equivalent plastic fracture strain, $\bar{\varepsilon}_f^p$, under stress states of in-plane biaxial tension and out-of-plane compression. These tests consist of advancing a small diameter punch into a thin specimen plate, as illustrated in Figure 2.1. In some tests a second plate of a different, suitable material is placed in back of the specimen. The specimen and backing plate are rigidly clamped around the circumference.

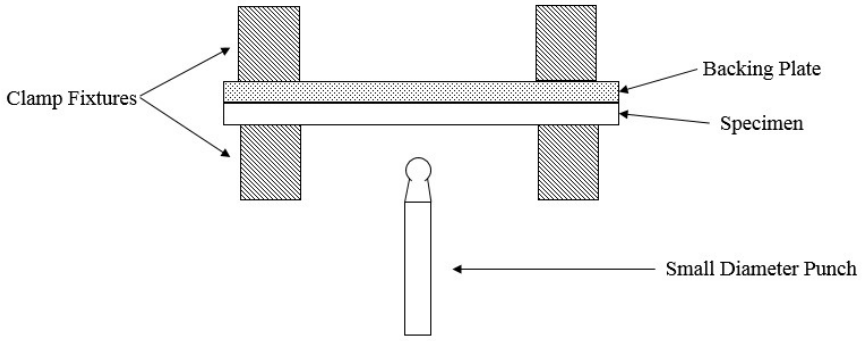

Figure 2.1 Schematic of a small diameter backed punch test

The small diameter punch induces in-plane biaxial tension on the back surface of the specimen opposite the punch. A small diameter punch is used to minimize the effect of the clamped boundary condition on the stress state and to induce fracture as close to the center displaced area as possible. This center region is where the material experiences in-plane biaxial tension. A hemispherical punch is used to induce an equal amount of in-plane tension along the two major in-plane axes. Such loading with equi-biaxial in-plane tension results in a Lode parameter equal to

$L = -1$. An elliptical shaped punch is used to induce unequal amounts of tension along the in-plane axes. Such an induced stress state no longer has $L = -1$. In these tests, an elliptical punch with a 6 mm major diameter and a 2 mm minor diameter is used in an attempt to induce a stress state with an average Lode parameter of $L = -0.5$. The geometry and dimensions of each punch are shown in Figure 2.2.

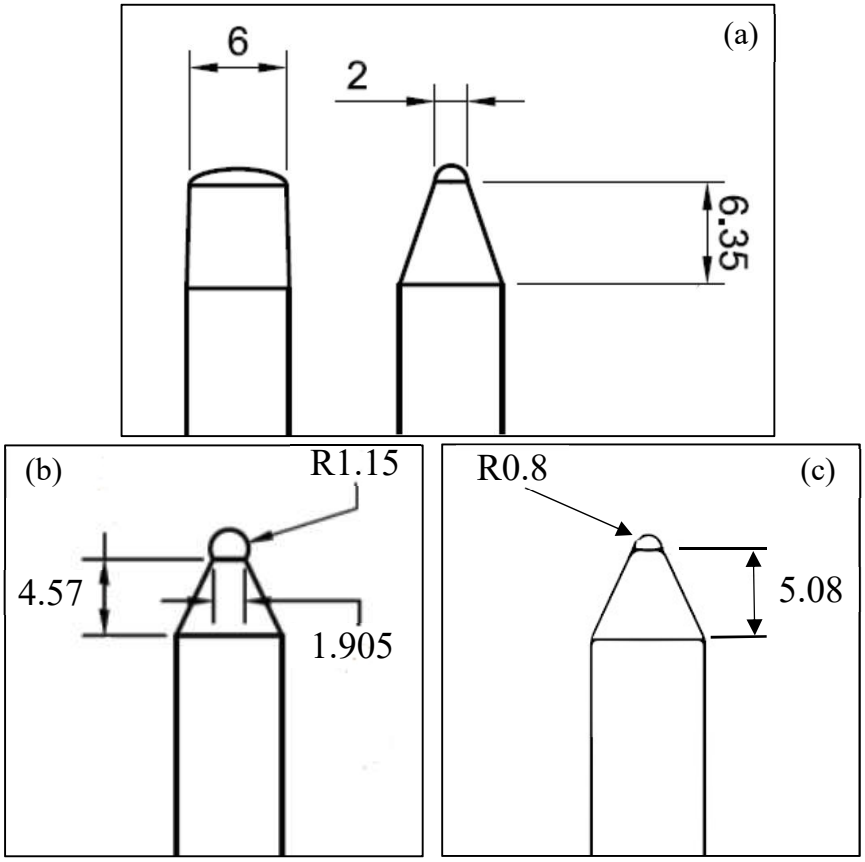

Figure 2.2 Geometry of (a) 2x6 mm elliptical punch, (b) 2.3 mm hemispherical punch and (c) 1.6 mm hemispherical punch

The backing plates are used to induce out-of-plane compression, with a thicker backing plate inducing more compression. Unbacked tests conducted with no backing plate (and therefore no out-of-plane compression) have a triaxiality of $\sigma^* = -\frac{2}{3}$. Note that this analysis uses the LS-DYNA sign convention of triaxiality, where $\sigma^* = -\frac{\sigma_m}{\sigma_{vm}}$. This sign convention results in tension

dominated stress states having negative triaxialities, and compression dominated stress states having positive triaxialities. Therefore higher amounts of out-of-plane compression due to thicker backing plates yield more compressive (i.e., more positive) values of triaxiality. However as thicker backing plates are used, it becomes more difficult to induce equi-biaxial in-plane tension as the compressive forces inhibit the specimen plate from bulging outward and undergoing biaxial tension loading. Consequently, with thicker backing plates the hemispherical punch diameter must be decreased in order to successfully induce equi-biaxial in-plane tension.

The specimen plates are machined using wire Electrical Discharge Machining (EDM) from 12.7 mm plate stock, and the recast layer is ground off. The backing plate material is purchased as annealed sheets, ideally at the desired thickness for the test. However, a small amount of material is removed through milling for some cases to obtain the desired backing plate thickness. The backing plates are machined from the annealed sheets using a waterjet. The specimens and backing plates have identical side lengths and bolt circles for attachment to the loading fixtures, and differ only in plate thickness and material. This geometry (of both the specimens and backing plates) is shown in Figure 2.3, with all length dimensions in millimeters. Specimens with a 2.5 mm diameter bolt circle are used with the loading fixture clamp having a diameter of 25.4 mm, and specimens with a 2.75 mm diameter bolt circle are used with the loading fixture clamp of diameter 50.8 mm.

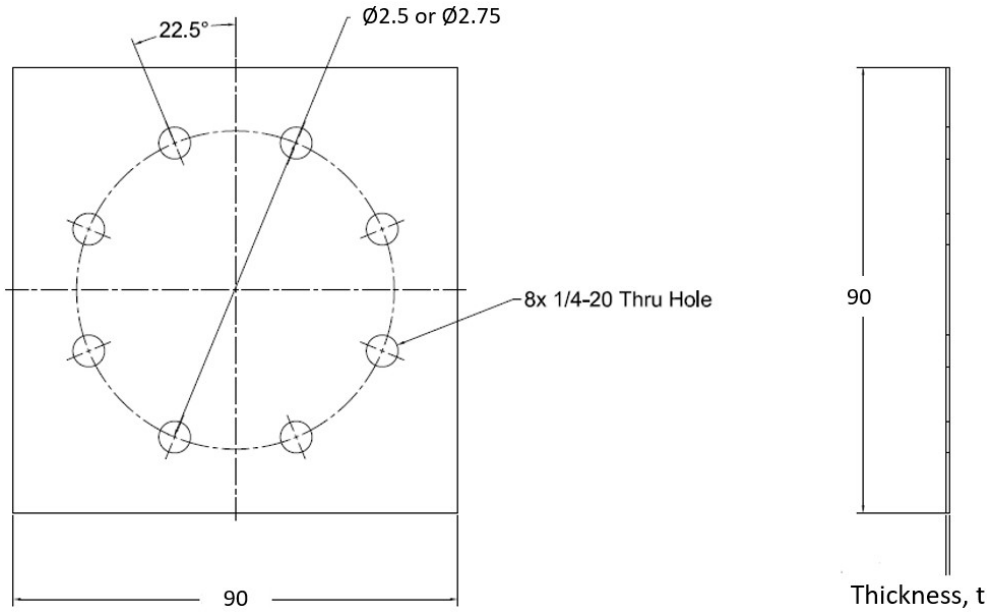

Figure 2.3 Punch test specimen and backing plate geometry

The punch tests are performed on an MTS 793 hydraulic load frame. The clamp and die fixture to hold the specimen and backing plate is attached to the top of the load frame by the use of MTS647.02B-22 hydraulic wedge grips. The small diameter punch is likewise attached to the bottom actuator using the hydraulic wedge grips, and it is then advanced into the specimen plate at a constant rate of 0.08 mm/s. The load between the punch and the specimen is recorded by a load cell in the hydraulic load frame, and the punch displacement is recorded by a Linear Variable Differential Transformer (LVDT).

In order for these tests to achieve the desired stress state, a suitable backing plate material must be chosen. The backing plate material must have a lower yield stress and greater ductility than the specimen material. Backing plates of annealed 110 copper are used for tests on Al2024, and backing plates of annealed AISI 1075 spring steel are used for tests on Ti64 and In718. Each backing plate material is characterized by uniaxial tension tests to determine the yield stress and the post-yield plastic behavior. Tension specimens, the geometry of which is shown in Figure 2.4, are machined from the annealed sheet of backing plate material using a waterjet and tested on the

MTS 793 hydraulic load frame. The axial force and displacement are recorded by the frame, and two Point Grey Gazelle digital cameras with 35 mm lenses are used to take synchronized images of the tension specimens during the test for analysis using Digital Image Correlation (DIC).

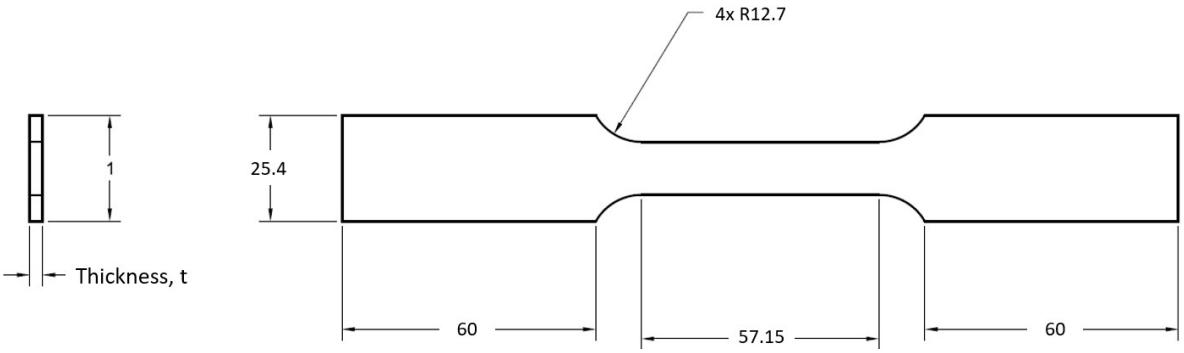

Figure 2.4 Geometry of tension specimens used to characterize the backing plate material properties

DIC is an optical measuring technique where deformation is tracked by taking consecutive images of the specimen as it deforms. A speckle pattern is applied to the surface of each specimen prior to the test, and software is used to track movement and deformation of the speckles in the images. This is done by tracking a square subset of pixels over consecutive images. A user defined step parameter, n, tells the software to place a subset center at every n^{th} pixel. Each individual subset is identified and tracked by assigning grayscale values to the unique black and white speckle pattern inside of that subset. Correlated Solutions VIC-2D or VIC-3D software is used to obtain the displacement and strains from the images [34]. A logarithmic Hencky strain tensor is used to resolve the measured displacements into strain values. A 90% center weighted Gaussian filter is used to smooth the strains over a number of displacement data points, defined by a user chosen filter size. A virtual strain gage length (VSGL) can be found by $VSGL = \frac{mm}{pixel} \times Step \times Filter$, where the $\frac{mm}{pixel}$ is simply the physical length in millimeters of each pixel in the image. The VSGL is necessary for accurate comparisons between strain values calculated by DIC and those simulated using FEA. The DIC and FEA strains should be compared at the same size resolution (i.e.,

matching VSGL and mesh size) in order to avoid discrepancies due to the higher resolution measurement being able to better capture strain localization. A comprehensive overview of DIC techniques and theory can be found in Sutton et. al. [35].

A black and white speckle pattern is applied to the surface of the specimens with spray paint. For the unbacked punch tests, the specimen is loaded continuously until fracture occurs. During the test, the back surface of the specimen is reflected in a mirror placed at a 45° angle on the top clamping fixture, as shown in Figure 2.5. A pair of Point Grey Gazelle GZL-CL-41C6M-C digital cameras with 35 mm lenses are used to take synchronized images of the reflected back surface for 3D DIC analysis.

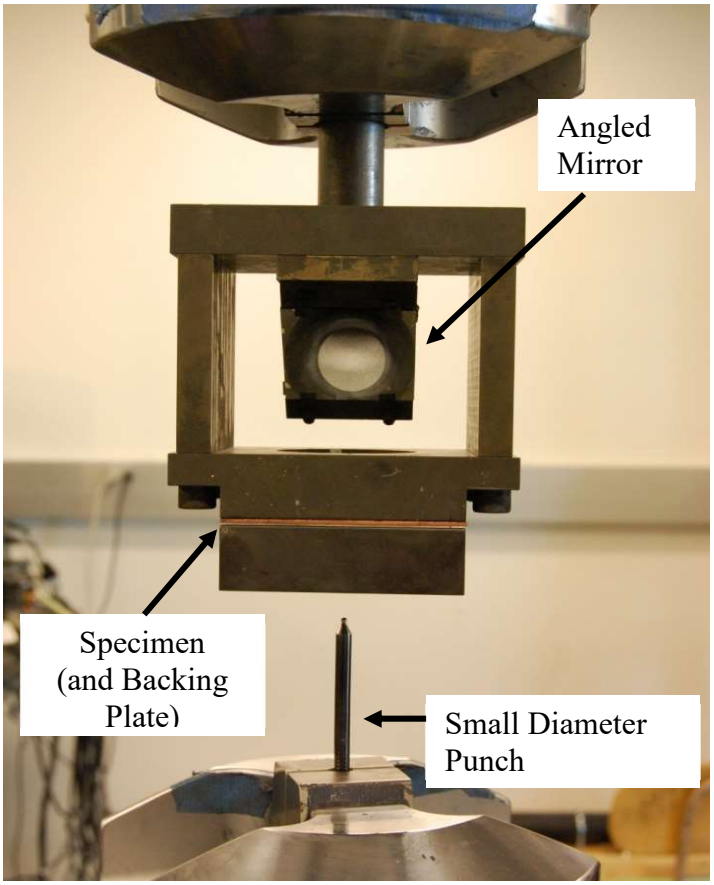

Figure 2.5 Experimental setup on the MTS 793 load frame of a small diameter backed punch test

For tests performed with a backing plate, the backing plate blocks the view of the specimen in the mirror during the test. Therefore DIC images cannot be obtained during loading, and additional interrupted tests are performed to capture DIC images. During interrupted tests the punch is displaced a set increment into the specimen and then stopped. The specimen is unloaded and removed from the loading fixtures, placed in a separate fixture where an image of the back surface of the specimen is taken for DIC analysis, and then placed back into the loading fixtures and another loading increment is applied. This process is illustrated in Figure 2.6. The process is repeated until fracture of the specimen is observed. Images are taken using two Point Grey Gazelle GZL-CL-41C6M-C digital cameras with 35 mm lenses and linear polarizing filters, and the specimen is illuminated with a polarized light source.

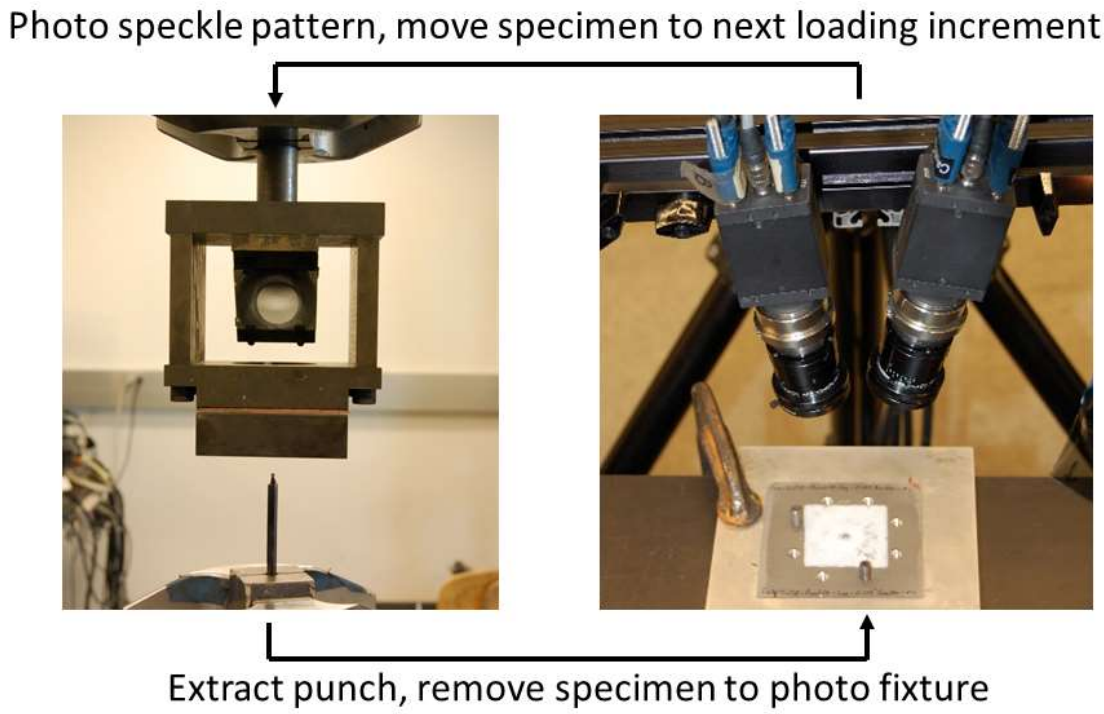

Figure 2.6 Experimental procedure of an interrupted, sequentially loaded backed punch test showing the loading fixture (left) and the photo fixture (right)

The polarized light source and filters are used to reduce the glare caused from a clear Teflon spray lubricant that coats the rear surface of the specimen. This lubricant is used to reduce friction,

and also to protect the DIC speckle pattern from wearing off and being degraded due to contact with the backing plate. The Al2024 tests with a hemispherical shaped punch used solely a Teflon lubricant coating on top of the DIC speckle pattern, as did initial tests on Ti64 and In718. Later tests on Al2024 using an elliptical punch and additional tests on Ti64 and In718 utilized a thin protective layer of clear M-Bond 200 strain gage adhesive on top of the painted speckle pattern. The clear adhesive layer was added to provide additional protection for the speckle pattern against wear and degradation due to contact with the backing plate. The clear Teflon lubricant was then coated on top of the adhesive layer to minimize friction.

In addition to DIC, acoustic emissions (AE) sensing was used to detect fracture for the Al2024 elliptical backed punch tests loaded continuously until fracture. A piezoelectric transducer is placed on or near the specimen, as shown in Figure 2.7. The transducer detects vibrations and converts them into a voltage signal, which is then sent to and analyzed by a Micro II PCI-2 Acoustic Emission System. When the voltage signal crosses a set decibel threshold, it is registered as an AE hit and the signal is recorded for a set period of time, as shown in Figure 2.8.

Each AE hit can be analyzed to determine the maximum amplitude, the time duration until the signal returns to below the threshold, and the frequency components. In addition, the detected energy of each hit can be calculated from the area between the voltage signal and the baseline.

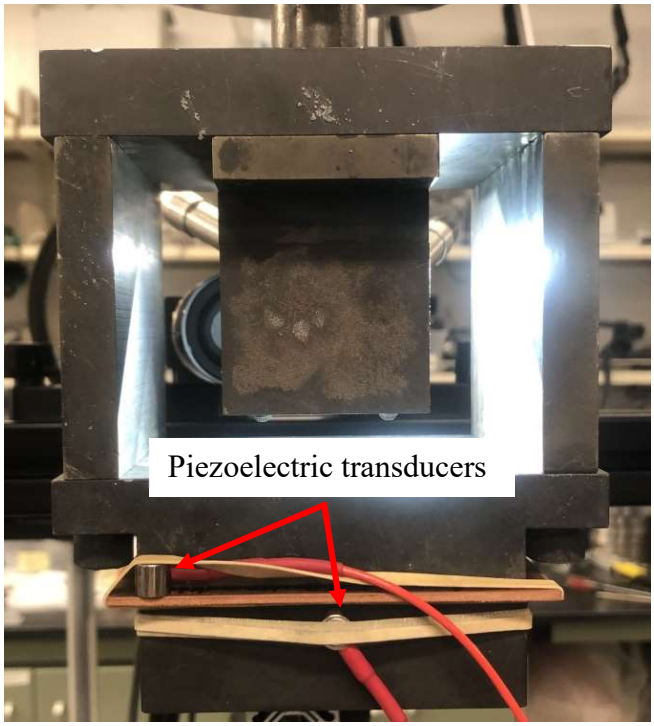

Figure 2.7 Piezoelectric transducers for acoustic emissions detection attached to the punch test loading fixtures

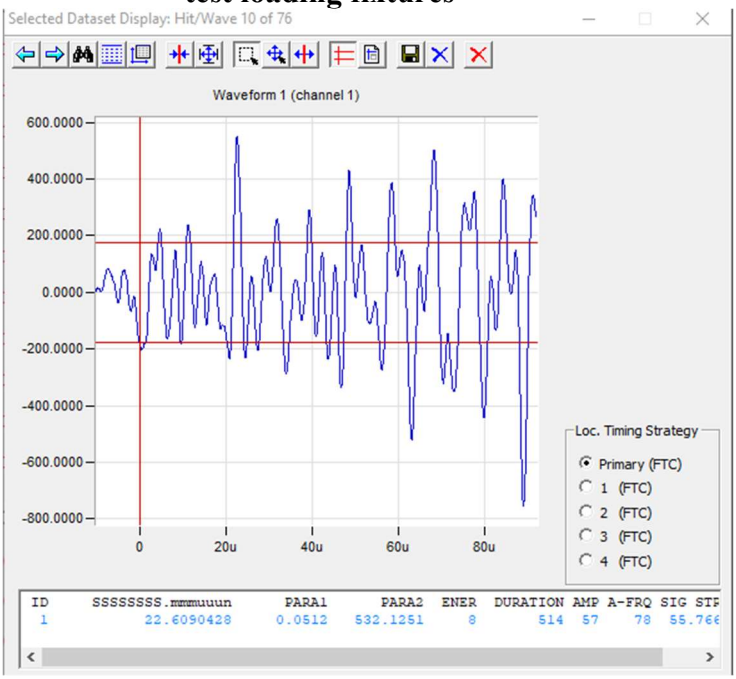

Figure 2.8 Detected acoustic emissions hit from Micro-II PCI Acoustic Emission System

The different small diameter backed punch tests performed and the relevant test geometries are summarized in Table 2.5.

Table 2.5 Small Diameter Backed Punch Test Experimental Program Overview

Material	Punch Diameter (mm)	Specimen Thickness (mm)	Backing Plate Thickness (mm)	Loading Fixture Clamp Diameter (mm)
Al2024	2.3 (spherical)	1.27	N/A (unbacked)	50.8
		0.635	1.27	25.4
	1.6 (spherical)	0.635	2.54	25.4
	2x6 (elliptical)	1.27	N/A (unbacked)	25.4
		1.27	1.575	25.4
		1.27	2.36	25.4
		1.27	3.175	25.4
Ti64	2.3 (spherical)	0.635	N/A (unbacked)	25.4
		0.635	0.889	25.4
		0.635	1.27	25.4
	1.6 (spherical)	0.635	1.83	25.4
In718	2.3 (spherical)	0.635	N/A (unbacked)	25.4
	1.6 (spherical)	0.635	1.83	25.4
		0.635	2.77	25.4

2.3 Direct Impact Split Hopkinson Bar Experiments

To test materials at strain rates on the order of 10^4 s^{-1}, modified direct impact split-Hopkinson bar (SHB) experiments are performed. These experiments are performed using the high pressure gas gun at the NASA Glenn Research Center's (GRC) Ballistics Impact Laboratory. A schematic of the test is shown in Figure 2.9.

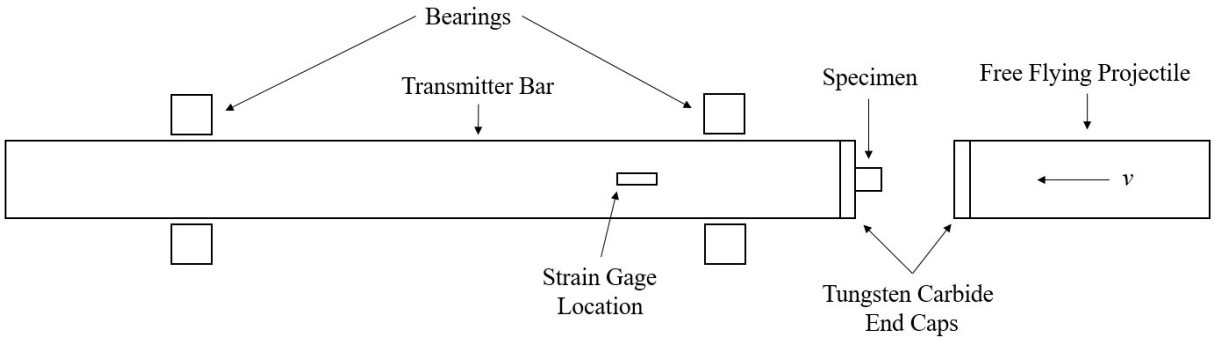

Figure 2.9 Schematic of a modified direct impact split Hopkinson bar test

A cylindrical specimen is placed on the front end of a transmitter bar and is impacted with a free flying projectile traveling at approximately 200 m/s. The transmitter bar and projectile are

made of Titanium 6Al-4V, with 2.54 mm thick tungsten carbide caps to avoid localized plastic deformation at the projectile-specimen and transmitter-specimen contact surfaces. The end caps are attached on the ends using JB-Weld steel reinforced epoxy. The transmitter bar has a length of 304.8 mm and a 12.7 mm diameter, while the projectile has a length of 50.8 mm and a 12.7 mm diameter. The projectiles have an average mass of 33.7 g, and the polycarbonate sabots used to house the projectiles in the barrel have an average mass of 79.7 g.

The transmitter bar and projectile are placed inside a vacuum containment chamber during the impact, as shown in Figure 2.10(a). A vacuum containment chamber is used in order to eliminate the effects of air resistance on the free-flying projectile and to contain debris. The transmitter bar is situated in two Teflon bearings allowing it to translate axially with minimal resistance. Grease is applied to both ends of the specimen to minimize the effects of friction as well as to hold it in place on the end of the transmitter bar.

The gas gun has a 6.4 m long barrel with a 50.8 mm inner diameter, and uses a pressure vessel with volume 3.07×10^{-2} m^3. A Mylar disk is used to separate the pressurized gas in the pressure vessel from the gun barrel. The gun is then fired by running an electrical charge through a nichrome wire embedded in the Mylar disk. This heats the wire and causes the disk to melt and burst, releasing the pressurized gas down the gun barrel. Prior to releasing the gas, a polycarbonate sabot holding the projectile, shown in Figure 2.10(b), is placed inside the gun barrel in front of the Mylar disk. The pressurized gas propels the sabot and projectile down the barrel towards the vacuum chamber. A sabot stripper is used on the end the barrel to catch and stop the sabot, while allowing the projectile to continue unimpeded out of the barrel and into the target.

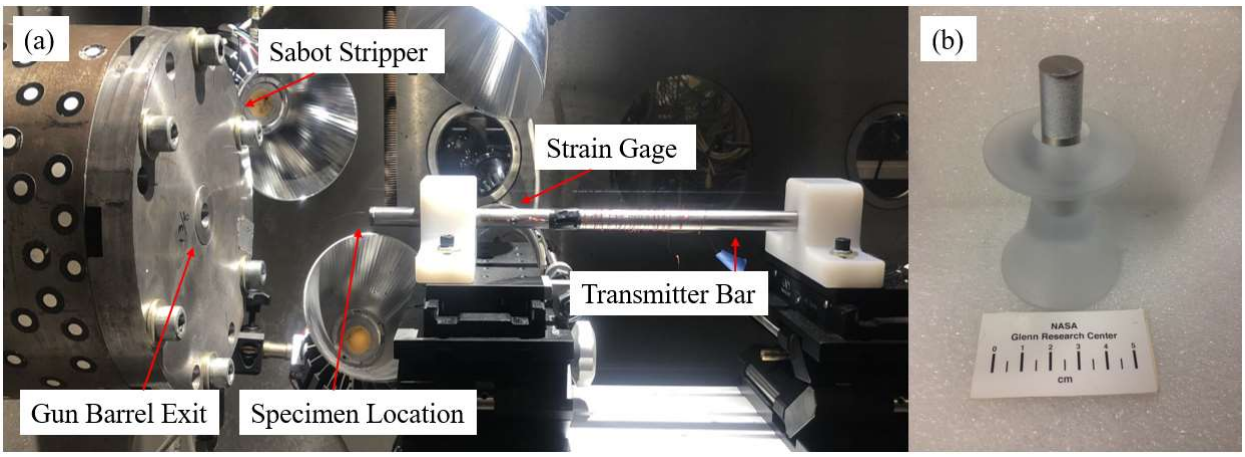

Figure 2.10 Photographs of (a) the test setup inside the vacuum containment chamber and (b) the titanium projectile and polycarbonate sabot

The transmitter bar is instrumented with 350 Ω strain gages in a half-bridge configuration at a distance of 75 mm from the impacted end. Upon impact the voltage output of these strain gages is recorded using an oscilloscope and is then converted into values for the force between the specimen and transmitter bar using a previously calibrated 1780 N/mV conversion value (assuming elastic deformation of the transmitter bar). To determine this conversion value, the transmitter bar is placed under tensile load using an MTS 793 load frame. The applied force is recorded by a load cell in the frame, and the voltage output of the strain gages is recorded using an oscilloscope. The conversion value from voltage output to the applied force can be determined by plotting the applied force vs. voltage and finding the slope, as illustrated in Figure 2.11.

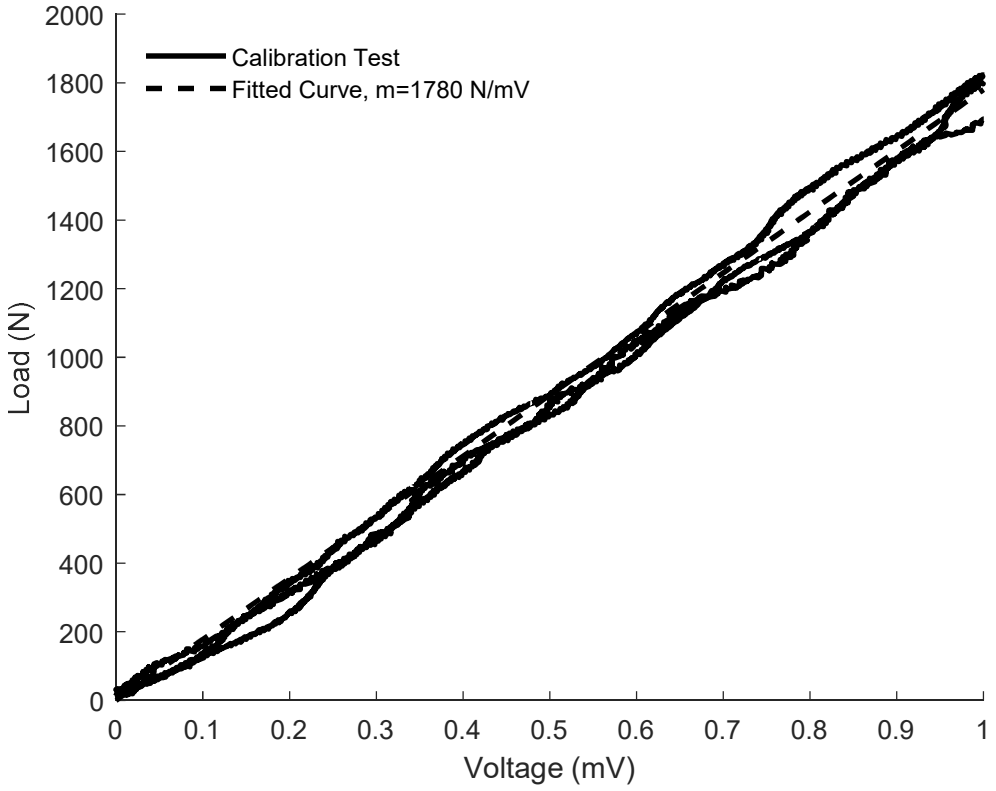

Figure 2.11 Calibration of applied force vs. strain gage voltage output of Ti64 transmitter bar used for direct impact tests

The strain gage voltage output is also used as the trigger input for a Shimadzu HPV-X2 high speed digital camera outfitted with a 200 mm Nikon lens. The camera is positioned outside the vacuum chamber to take images through one of the chamber viewports of the side view of the projectile impact, as shown in Figure 2.12. The camera is set in continuous record mode, and when the memory buffer becomes full it discards the oldest image as it takes a new image. Once the voltage input from the strain gage passes a set threshold, indicating impact has occurred, the camera is signaled to stop recording images and to save those it has already taken of the impact. Images are taken at a rate of 2,000,000 or 5,000,000 frames per second and used for 2D DIC analysis using Correlated Solutions VIC-2D software.

Figure 2.12 Shimadzu HPV-X2 high speed camera positioned outside the vacuum containment chamber

Because of the high frame rate, the camera has a very short exposure time, between 200 and 500 nanoseconds. Therefore, a large amount of light is necessary in order to capture useable images for DIC analysis. 6 Cree CXA2790 LED lights, each with an output of 15,000 lumens, are used to illuminate the specimen. The specimen, transmitter bar, and projectile are given a black and white speckle pattern using spray paint. The relative displacement between the projectile and the transmitter bar, the projectile velocity, and the strain and displacement field on the specimen are then determined using DIC.

An estimate of the nominal engineering strain rate experienced by the specimen during these tests can be calculated by assuming minimal change in the projectile velocity after impact and that the transmitter bar remains relatively stationary. This yields that the projectile velocity, V_{proj}, is equal to the rate of change in length of the specimen. Dividing this rate of change in specimen length by the original specimen length gives the engineering strain rate, as shown in Eq. 2-1. This calculation assumes uniform deformation of the specimen across its length.

$$\dot{\varepsilon} = \frac{\Delta \dot{L}}{L_o} = \frac{V_{proj}}{L_o} \tag{2-1}$$

The specimen material, specimen geometry, nominal engineering strain rate and the camera frame rate for each test are summarized in Table 2.6.

Table 2.6 Direct Impact split-Hopkinson bar Test Program Overview

Specimen Material	Specimen Geometry (mm)	Nominal Strain rate (s^{-1})	Frame Rate (frames/s)
Al2024	Ø5.08 x 5.08 Length	39,370	5,000,000
	Ø5.08 x 10.16 Length	19,685	2,000,000
Ti64	Ø5.08 x 5.08 Length	39,370	5,000,000
In718	Ø5.08 x 5.08 Length	39,370	5,000,000

Chapter 3 Numerical Analysis

3.1 Numerical Analysis of Small Diameter Backed Punch Tests

The small diameter backed punch tests are simulated using the finite element code LS-DYNA. The hemispherical punch tests are simulated using 2D axisymmetric solid, volume weighted shell elements with a 0.05 mm mesh size. Quarter symmetry is used to simulate the elliptical punch tests, using 0.15 mm constant stress solid elements. Both types of simulations are shown in Figure 3.1.

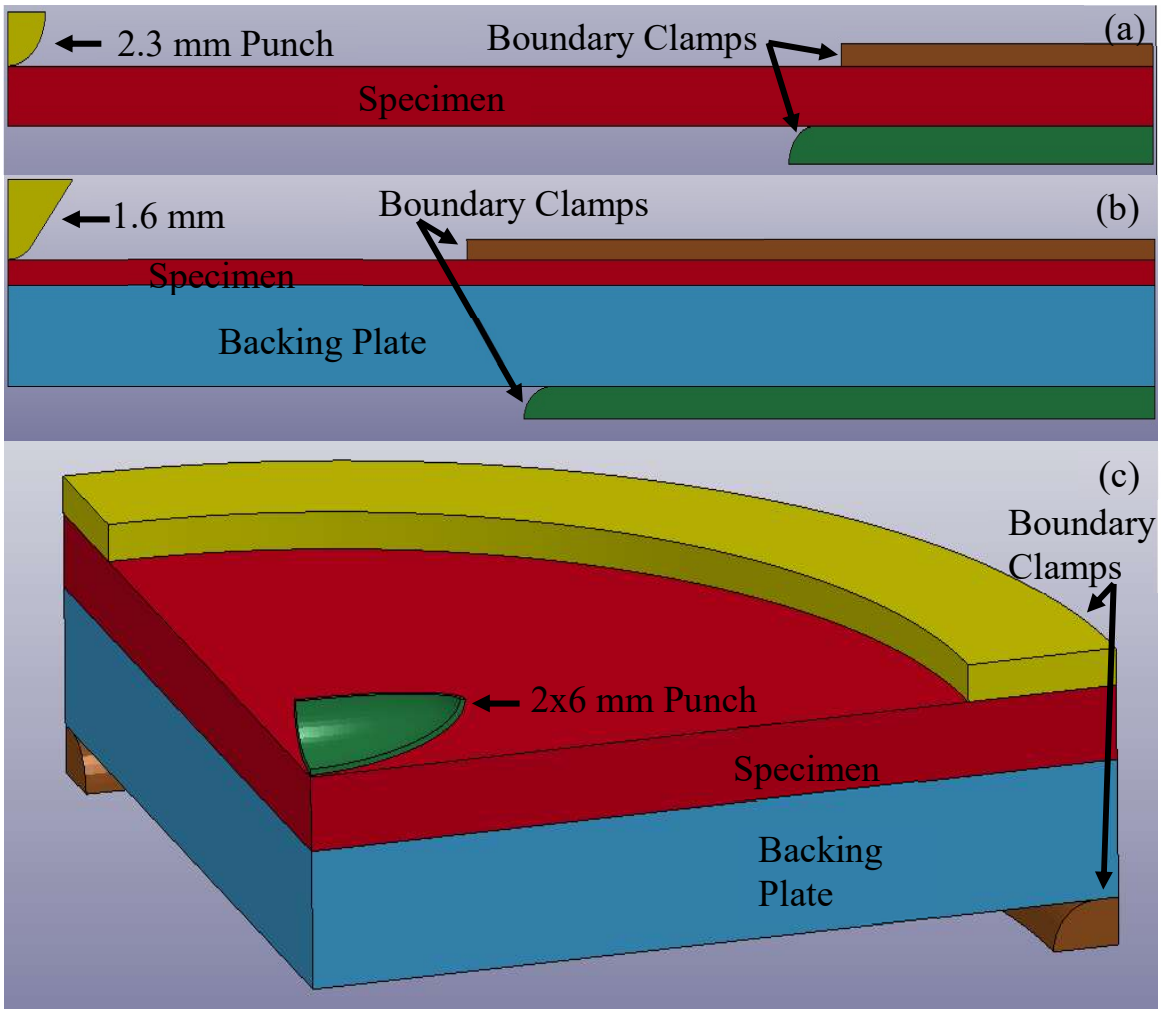

Figure 3.1 Depictions of (a) 2D axisymmetric simulation of an unbacked test with a 2.3 mm hemispherical punch, (b) 2D axisymmetric simulation of a backed test with a 1.6 mm hemispherical punch, and (c) quarter symmetric simulation of a backed test with a 2x6 mm elliptical punch

The punch and clamp fixtures are modeled using rigid material model *MAT_20. The clamps are fully constrained in a fixed position, and the punch is constrained so that it can only translate in the direction perpendicular to the specimen surface. The nodes at the outermost circumference of the specimen and backing plate are fully constrained to simulate the clamped boundary condition that rigidly holds the specimen and backing plate in place. Friction is not considered, as the contact interfaces in the tests are lubricated.

The specimen and backing plate materials are modeled using *MAT_24, a linear piecewise plasticity model. The linear elastic behavior of each material is defined by the elastic modulus, *E,* and Poisson's ratio, ν, summarized in Table 3.1 along with the yield stress. The post-yield behavior of each material is defined by a true stress-plastic true strain curve derived from uniaxial test data using the method described in Park et. al. [11].

Table 3.1 Elastic modulus, Poisson's ratio, and yield stress of simulated materials

Material	Elastic modulus (GPa)	Poisson's ratio	Yield Stress (MPa)
Annealed copper	117	0.343	68.2
AISI 1075 steel	200	0.290	342.5
2024 aluminum	70	0.339	381.2
Titanium 6Al 4V	110	0.342	718.2
Inconel 718	210	0.290	996.7

While the engineering stress and engineering strain are defined by the original cross-sectional area and original length, respectively, the true stress and true strain are based upon the instantaneous cross-section and length. The engineering stress and engineering strain can be converted into true stress and true strain by Equations. 3-1 and 3-2:

$$\sigma = \sigma_{eng}(1 + \varepsilon_{eng}) \tag{3-1}$$

$$\varepsilon = \ln(1 + \varepsilon_{eng}) \tag{3-2}$$

The above formulas assume material incompressibility and uniform deformation along the gage length. These assumption remain valid up until necking occurs, defined as when the true

stress is equal to the tangent modulus, $\sigma(\varepsilon) = \frac{d\sigma(\varepsilon)}{d\varepsilon}$. After necking the deformation along the gage length is no longer uniform and the post-necking true stress-true strain curve must be derived separately. This is done by assuming multiple post-necking curves that follow a power law hardening behavior. These curves are used as material models to simulate the tension test. The force-displacement behavior is compared between the test and the simulations, and the material model that best matches the experimental data is assumed to have correctly captured the post-necking stress-strain behavior. This material model is then used as the input for the punch test simulations.

Tests of Al2024, Ti64, and In718 were performed and the true stress-true strain curves derived in previous research for the development of the *MAT_224 material models [9][10][11][33][36] are used. Tension tests are used to derive the input stress-strain curves for Al2024, In718, annealed C110 copper, and annealed AISI 1075 steel. However, Ti64 exhibits tension-compression asymmetry, where the observed stress-strain response differs between loading in tension versus compression. Because the punch tests will place the majority of the specimen material under compression, the compression test data is used to derive the true stress-true strain curve for the Ti64 *MAT_24 post-yield material model. The true stress-true strain curves used as the simulation input are shown in Figure 3.2. Rate sensitivity and temperature effects are not considered in the simulations, as the tests were performed at a slow loading rate and at room temperature.

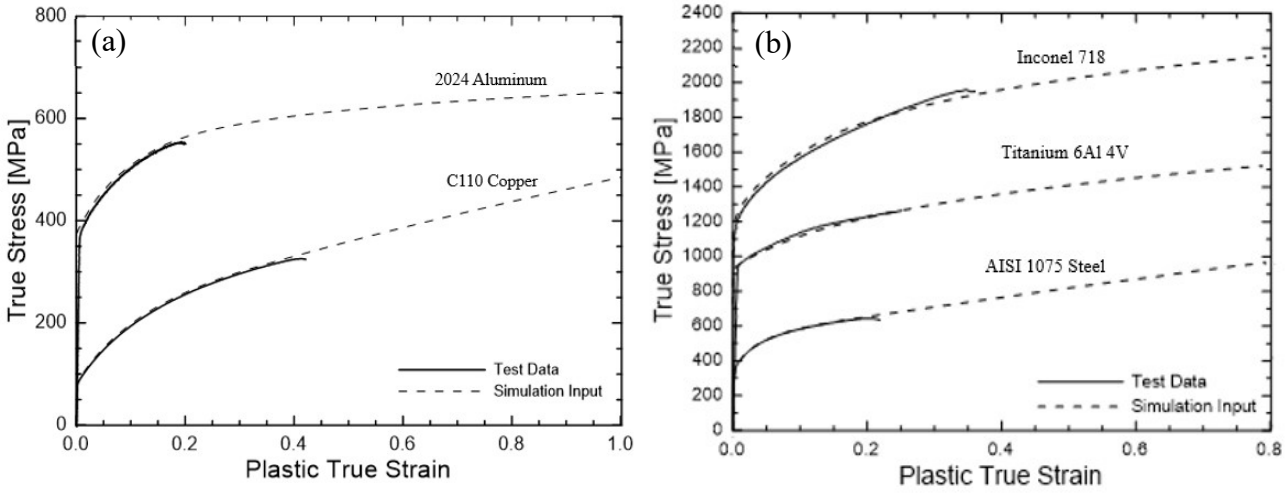

Figure 3.2 True stress-true strain curves used for material model input for (a) Al2024 punch tests with annealed C110 copper backing plates and (b) Ti64 and In718 punch tests with AISI 1075 steel backing plate

The punch force, punch displacement, and strain on the back surface of the specimen are compared between the tests and simulations. If these values agree it is assumed that the simulation is accurately modeling the material behavior. The simulated equivalent plastic strain, triaxiality and Lode parameter of the element corresponding to the location where fracture is initially observed in the tests are recorded. The simulations are ran until they reach the point where fracture is observed in the tests, and the final calculated value of the equivalent plastic strain at the fracture location is taken to be the equivalent plastic fracture strain.

3.2 Numerical Analysis of Direct Impact SHB Tests

The direct impact SHB tests are simulated in LS-DYNA using constant stress solid elements, as shown in Figure 3.3. The mesh composing the specimen and tungsten carbide end caps is approximately cubic with side length of 0.25 mm. The mesh composing the transmitter bar and projectile are slightly skewed along the axial direction, with side lengths of 0.25×0.25×0.762 mm. This is done in order to reduce the number of elements and decrease the simulation runtime.

The transmitter bar and projectile undergo only relatively small elastic deformation, and therefore any error due to the skewed mesh should be minimal.

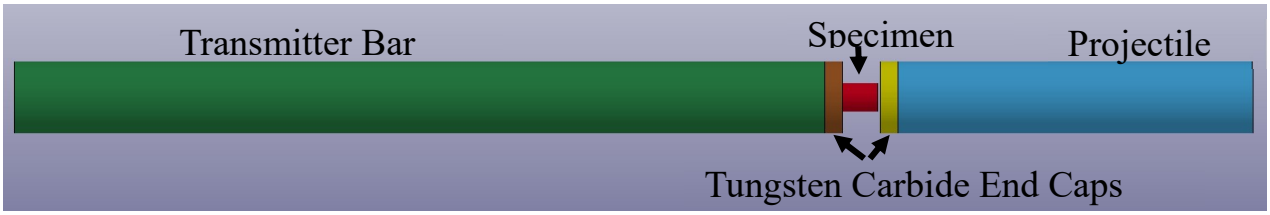

Figure 3.3 LS-DYNA simulation of a direct impact SHB experiment

While a 304.8 mm long transmitter bar is used in the tests, a 152.4 mm long transmitter bar is used in the simulations. This shorter transmitter bar is used to further decrease the simulation runtime. Using a shorter 152.4 mm long simulated transmitter bar does not affect the simulation since the experiment is finished before the reflected wave from the end of the transmitter bar reaches the strain gages.

The projectile and attached tungsten carbide end cap are given an initial velocity matching the values measured in the tests. Friction is not considered during the simulations, as lubrication is used on both ends of the specimen. No constraints or boundary conditions are used, as the projectile, specimen, and transmitter bar are free to move during the test. While the transmitter bar is globally constrained axially by the bearings in the test, it is not constrained at a local scale (i.e., at individual elements and nodes). Attempting to constrain the individual nodes would result in an artificially stiffening of the simulated transmitter bar material, which in turn would affect the simulated elastic stress waves.

The specimen material is modeled by the *MAT_224 material models for Al2024, Ti64, and In718 developed by the FAA's Uncontained Engine Debris Mitigation program [11][33][36], including temperature and strain rate effects. The simulated strain rate hardening and thermal softening behavior of each of these materials are shown in Figure 3.4 and Figure 3.5. Additional

simulations using specimen material models derived from the direct impact SHB experimental data are also performed, and the details of those material models are described in Chapter 4.2.

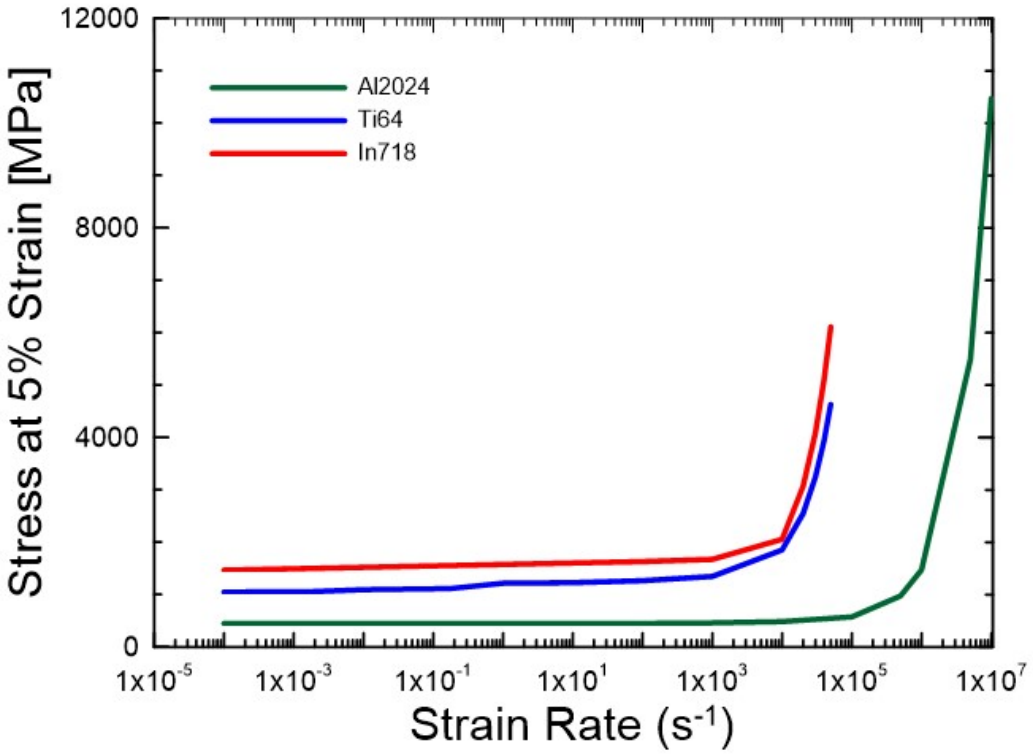

Figure 3.4 Strain rate sensitivity used in AWG *MAT_224 material models for Al2024, Ti64, and In718, characterized as the true stress at 5% plastic true strain for each strain rate

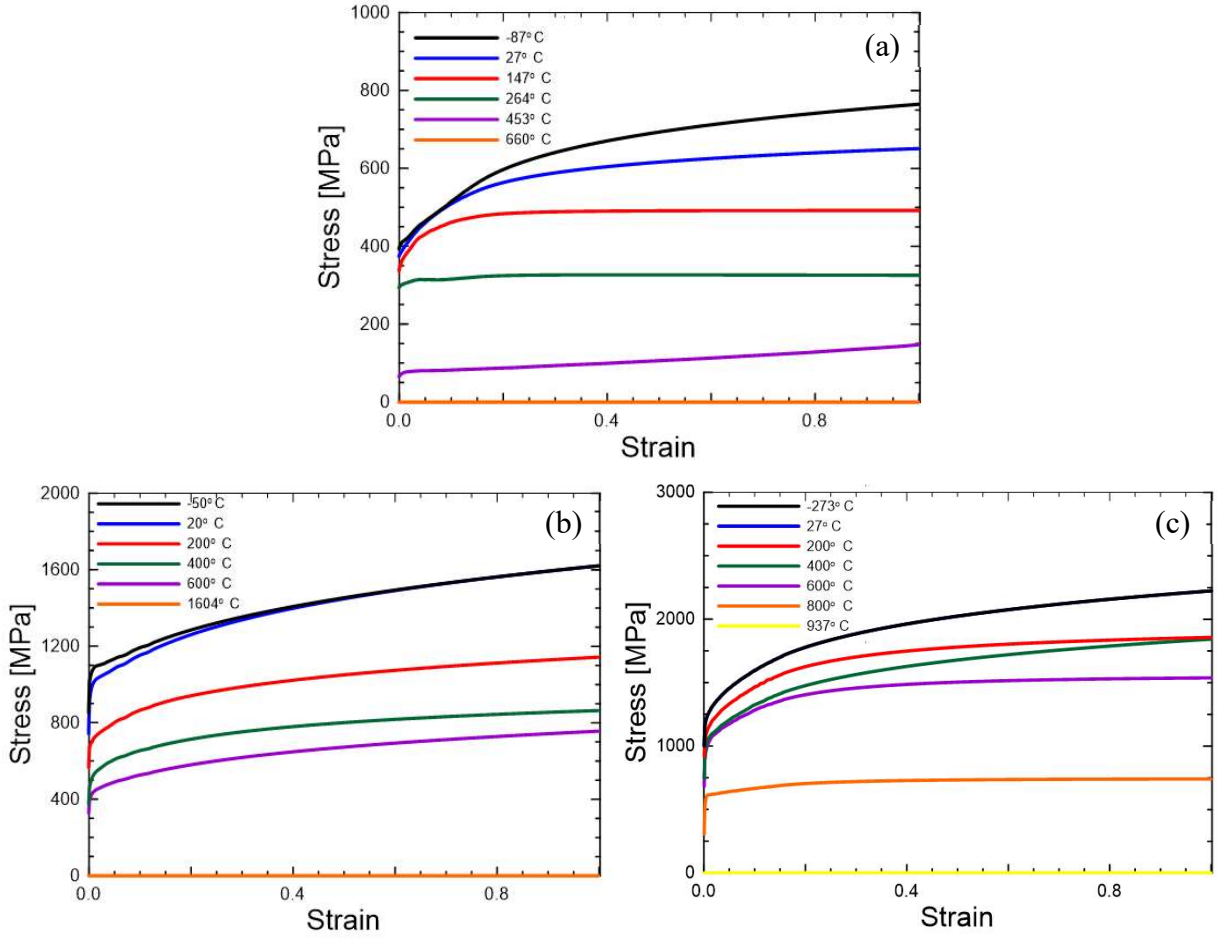

Figure 3.5 Thermal softening behavior in AWG *MAT_224 material models derived from elevated temperature tests for (a) Al2024, (b) Ti64, and (c) In718

The Ti64 transmitter bar and projectile are modeled as an elastic-perfectly plastic material utilized through a simplified *MAT_224 model. The elastic constants used are the same as those shown for Ti64 in Table 3.1. Because previous tests on Ti64 have shown it to be highly rate sensitive, the yield stress is set as $\sigma_y = 1.715$ GPa, which is the yield stress observed in the highest rate testing previously done on Ti64 [10]. The tungsten carbide end caps are also modeled as elastic-perfectly plastic utilizing *MAT_224, with elastic modulus E =670 GPa, Poisson's ratio ν =0.342, and yield stress σ_y =4 GPa. The simple elastic-perfectly plastic models are implemented through *MAT_224 in order to take advantage of the thermal solving capabilities

present in this material model. This allows the simulations to take into account potential heat transfer between the specimen and the projectile and transmitter bar.

The force through a cross-section of nodes and elements in the transmitter bar at a distance of 76.2 mm from the impacted end is recorded. This corresponds to the same location where the strain gages are located in the experiments. The displacement of the projectile, transmitter bar, and the displacement and strain on the specimen are also recorded in the simulations for comparison to the test data.

Chapter 4 Experimental and Numerical Results

4.1 Punch Test Results: Determination of Equivalent Plastic Fracture Strain

The data obtained from the small diameter punch experiments is compared to the LS-DYNA simulations. If the simulated force, displacement, and strains agree with the experimentally measured values, then it is assumed that the simulations are accurately capturing the physical material behavior. The simulated values of the triaxiality, Lode parameter, and equivalent plastic fracture strain are then taken as the true values. This assumption is necessary to determine the stress state parameters, as the local stress at the fracture location cannot be measured. The only way to determine the triaxiality and Lode parameter at that location is through numerical analysis. While the strain at the fracture location can sometimes be directly measured using DIC, it is generally considered best practices to use the simulated value of equivalent plastic fracture strain when constructing the fracture surface, even if that value is slightly different than the experimentally measured value. This is to maintain consistency between the simulated and experimental results, and to ensure that the simulated fracture behavior matches the physical material behavior by having element failure and erosion occur at the same applied load and displacement as observed in the experiments.

Figure 4.1-Figure 4.4 compare the force-displacement curves between the experiments and simulations of the Al2024 hemispherical and elliptical backed punch tests, the Ti64 hemispherical backed punch tests, and the In718 hemispherical backed punch tests, respectively. The solid curves correspond to tests loaded continuously until fracture, and the dashed lines are from a representative sequential test loaded in interrupted steps until fracture. The more vertical portions of the sequential curves correspond to the unloading and re-loading portions of the tests, where the

material has been strain hardened by the plastic deformation in the previous loading increment. Sequential loading is not performed for the unbacked tests because it is unnecessary, as fracture can be directly observed in the DIC images taken during continuous loading until fracture.

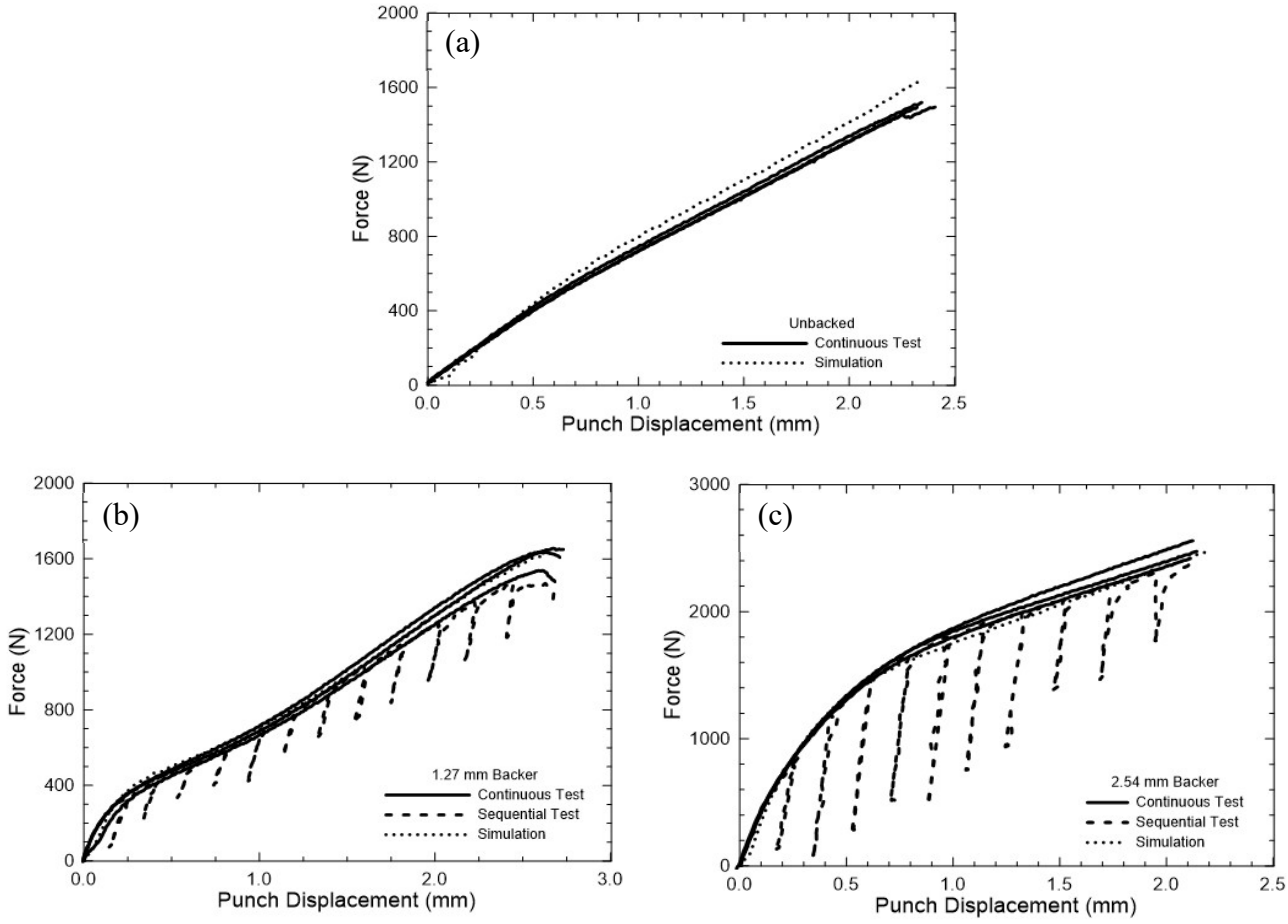

Figure 4.1 Comparison of experimental and simulated force-displacement curves of Al2024 hemispherical backed punch tests for (a) unbacked, (b) 1.27 mm and (c) 2.54 mm thick backing plates

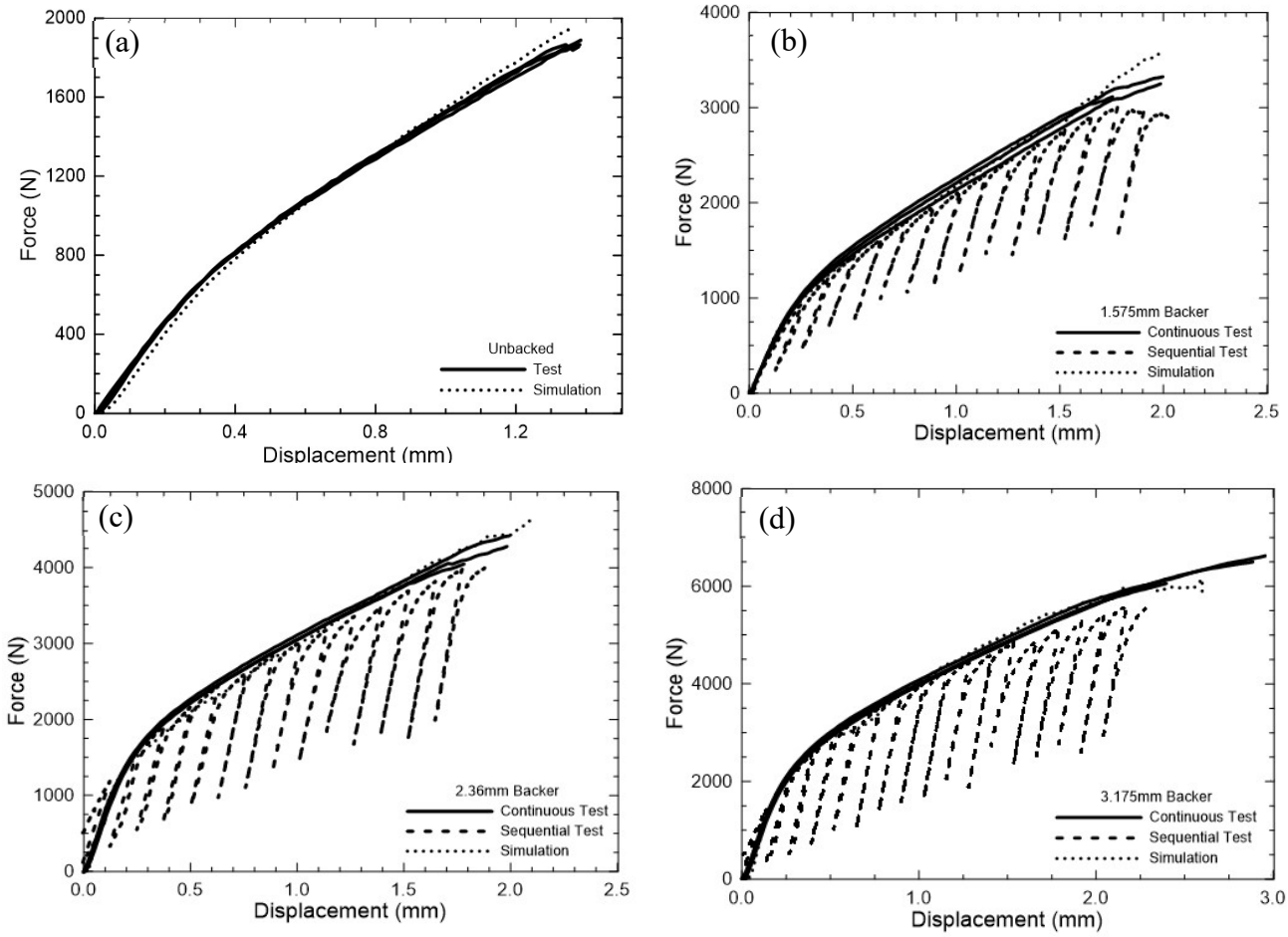

Figure 4.2 Comparison of experimental and simulated force-displacement curves of Al2024 elliptical backed punch tests for (a) unbacked, (b) 1.575 mm thick, (c) 2.36 mm and (d) 3.175 mm thick backing plates

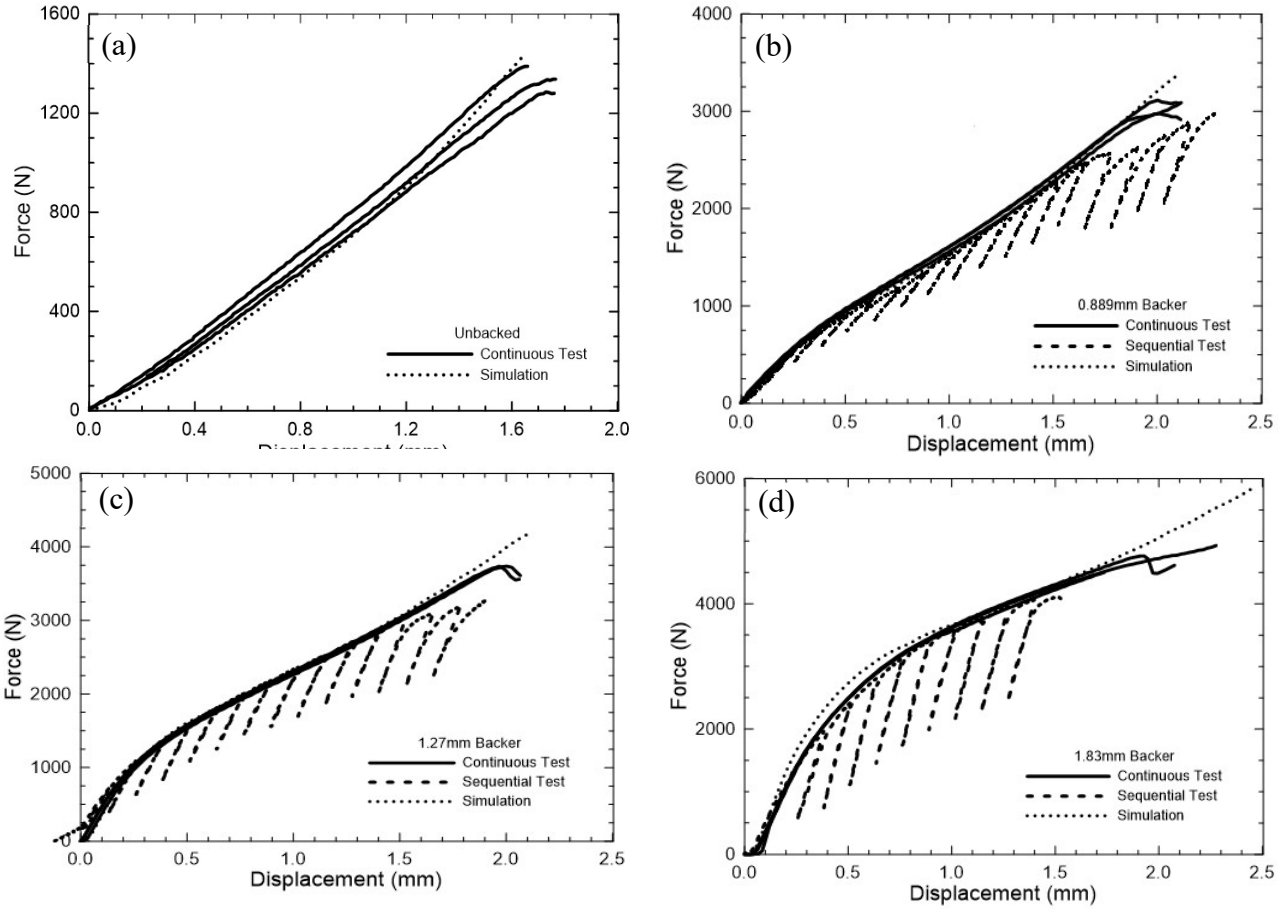

Figure 4.3 Comparison of experimental and simulated force-displacement curves of Ti64 hemispherical backed punch tests for (a) unbacked, (b) 0.889 mm, (c) 1.27 mm and (d) 1.83 mm thick backing plates

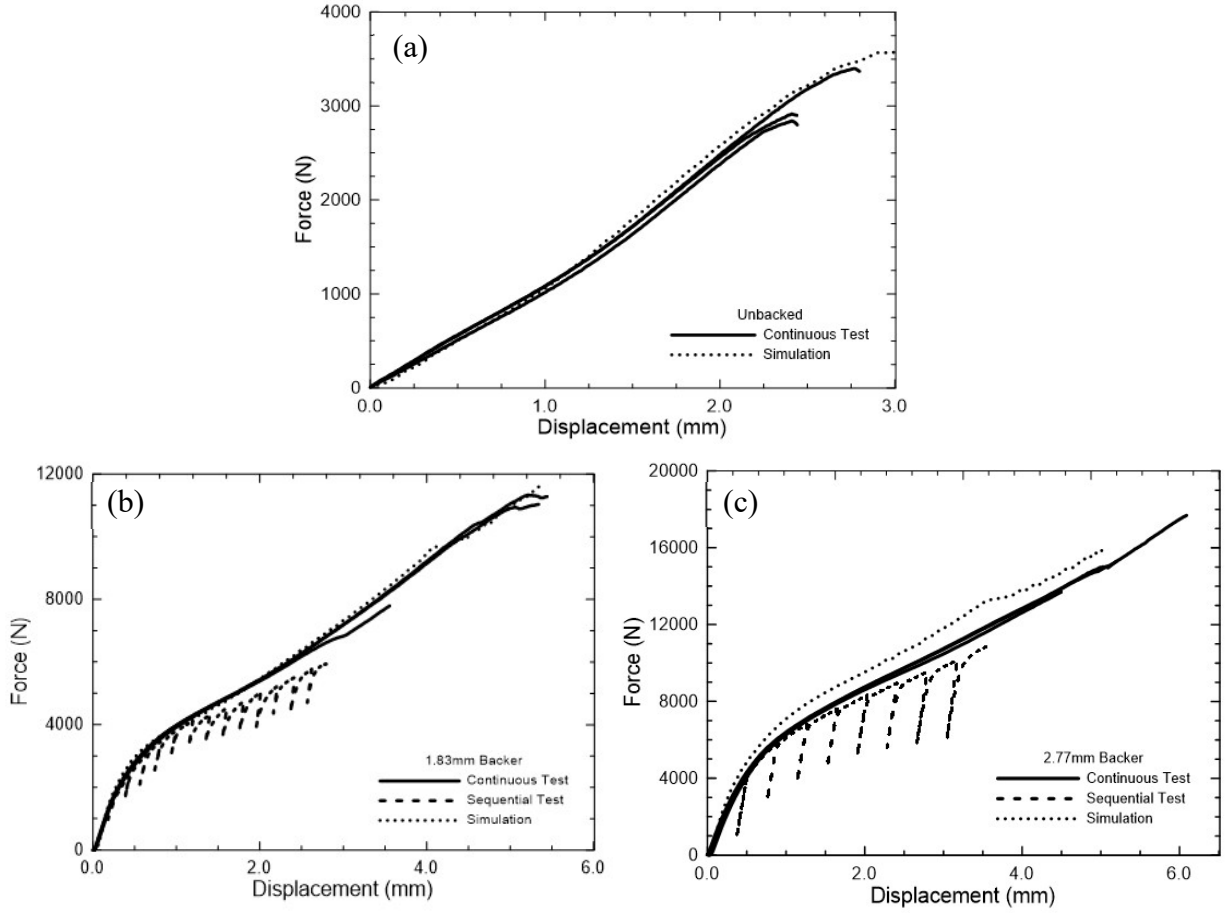

Figure 4.4 Comparison of experimental and simulated force-displacement curves of In718 hemispherical backed punch tests for (a) unbacked, (b) 1.83 mm and (c) 2.77 mm thick backing plates

As can be seen in Figure 4.1 - Figure 4.3, there is good agreement between the continuous tests, sequential tests, and the simulations for the Al2024 hemispherical and elliptical punch tests and the Ti64 hemispherical punch tests up until the point of fracture seen in the tests. The plastic deformation of the sequential tests (the portions of the curve above the unloading and reloading sections) aligns well with the plastic deformation seen in the continuous tests. This indicates that the sequential nature of loading is not significantly altering the material response compared to continuous loading for the Al2024 and Ti64 experiments.

However, this is not the case for In718. While Figure 4.4(a) and (b) show good agreement between the continuous tests and the simulations, Figure 4.4(c) shows that the simulated force is slightly above the force measured in the continuous test. It can also be seen in Figure 4.4(b) and (c) that the In718 sequential and continuous tests do not agree. The sequential tests show a lower load level compared to tests loaded continuously until fracture.

In addition, the In718 sequential tests experience fracture earlier than the continuous tests. The sequential tests fail at an average punch displacement of 2.58 mm and average load of 5,507 N when a 1.83 mm backing plate is used, and at an average punch displacement of 2.24 mm and average load of 8,658 N when a 2.77 mm backing plate is used. Examining the post-test specimens from the continuous tests, shown in Figure 4.5 and Figure 4.6, shows that fracture during continuous loading occurs later. Fracture occurs between 3.55 mm and 5.34 mm of punch displacement with a 1.83 mm backing plate, and between 4.49 mm and 5.2 mm punch displacement with a 2.77 mm backing plate. This corresponds to fracture occurring between load levels of 7,796 N and 11,025 N for the 1.83 mm backed tests, and between 13,674 N and 15,303 N for the 2.77 mm backed tests.

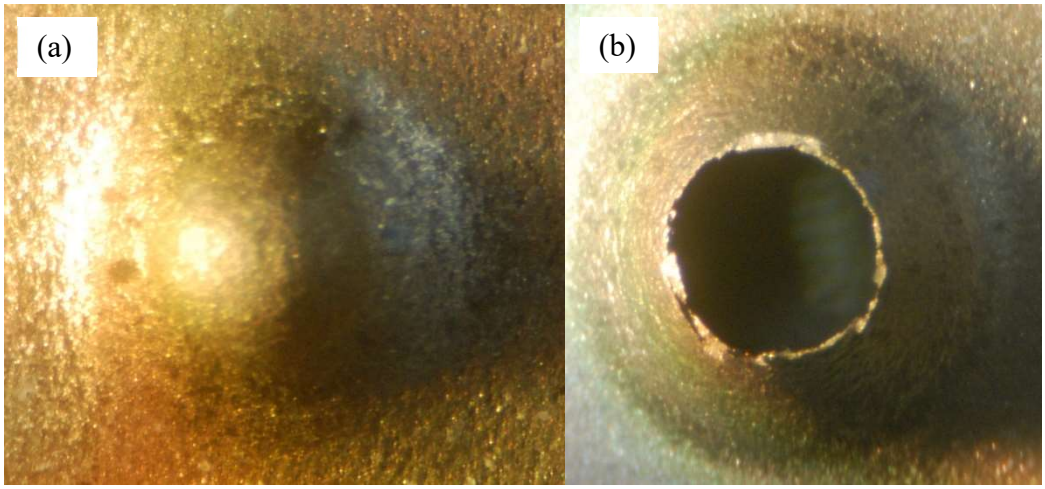

Figure 4.5 Post-test In718, 1.83 mm backed test specimens at punch displacements of (a) 3.55 mm-no fracture and (b) 5.34 mm - fracture

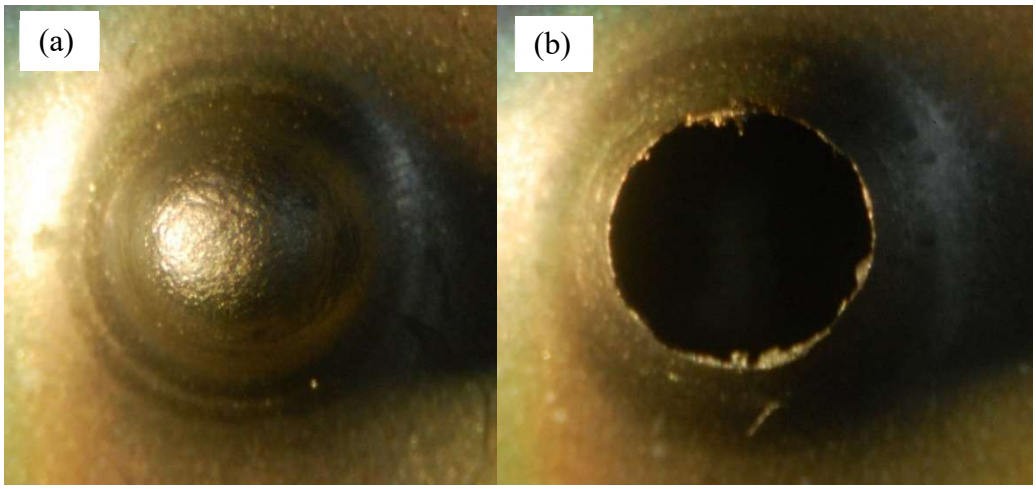

Figure 4.6 Post-test In718, 2.77 mm backed test specimens at punch displacements of (a) 4.49 mm-no fracture and (b) 5.20 mm - fracture

Therefore, for In718, the sequential nature of loading is clearly causing a different material response compared to continuous loading. This is likely due to how thin the In718 specimens become before fracture occurs. Post-test measurements of the specimens from the sequential tests shows an average thickness of 0.23 mm with a 1.83 mm backing plate and 0.094 mm with a 2.77 mm backing plate in the deformed area. The fact that the In718 specimens become so thin during these tests means that they are no longer structurally sound. The process of extracting the punch, removing the specimen for DIC imaging and replacing it, then re-engaging the punch with the specimen causes this extremely thin section of In718 material to fail prematurely compared to the tests loaded continuously until fracture.

An additional complication that arises when comparing the sequential and continuous tests is the added compliance caused by the layer of adhesive coated on top of the speckle pattern. The cyanoacrylate adhesive is much weaker than the metal specimen and backing plate, and therefore the adhesive begins to deform and compress at much lower loads. This introduces an additional compliance for the sequential tests (that use this adhesive layer) compared to the continuous tests (that do not have this adhesive layer). This additional compliance causes an artificial increase in

the measured punch displacement of approximately 0.15 mm in the sequential tests. Therefore the force-displacement curves from the sequential tests appear shifted to the right compared to the continuous tests, as shown in Figure 4.7(a) below.

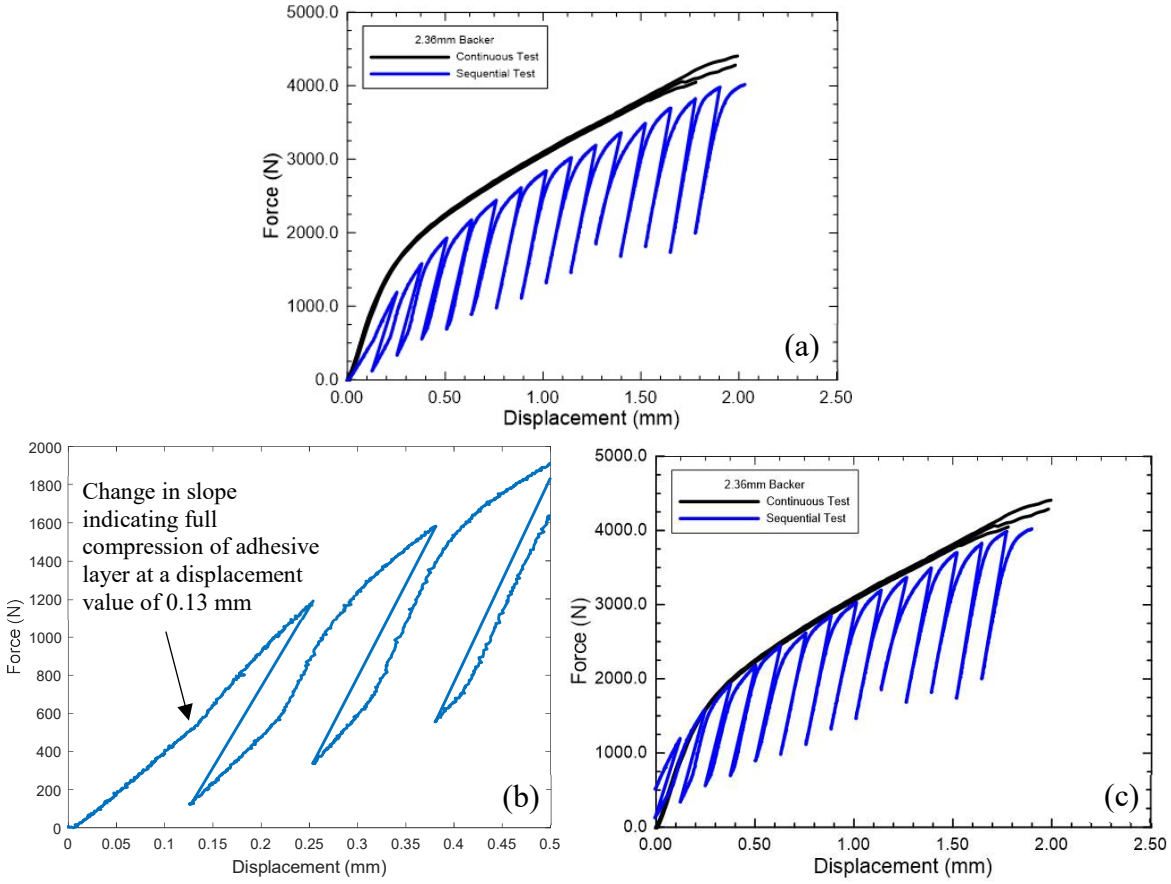

Figure 4.7 Additional compliance in sequential tests due of adhesive layer showing (a) uncorrected force-displacement curve, (b) identification of change in slope indicating onset of specimen and backing plate deformation and (c) corrected curve with additional compliance subtracted

However, the point where the adhesive layer becomes fully compressed can be easily identified by a change in slope in the early sequential loading increments, seen in Figure 4.7(b). The displacement value at this point, which corresponds to where the specimen and backing plate begin to deform, can be subtracted to correct for the additional compliance due to the compression of the adhesive layer. Doing so results in the force-displacement curves from the sequential tests

to align well with those of the continuous tests, as shown in Figure 4.7(c). This correction has been applied when necessary in Figure 4.1 - Figure 4.4, as well as in any of the following figures where the punch displacement values of the sequential tests are presented.

Post-test photographs of the failed specimens are shown in Figure 4.8 - Figure 4.11. The images show that fracture occurs on the back surface of the specimen, directly opposite the punch or very close to this location. As previously noted, the Al2024 and Ti64 tests in Figure 4.1 - Figure 4.3 show very similar force-displacement and fracture behavior between the sequential and continuous tests. Therefore, it is a reasonable assumption that the fracture location for Al2024 and Ti64 also remains similar between the continuous and sequential tests.

It is not as clear, however, that the fracture location of the In718 sequential backed tests corresponds to the same location where fracture occurs in the same tests loaded continuously until fracture. Recall that the In718 sequential backed punch tests show premature fracture compared to the continuous tests. So while the post-test photographs in Figure 4.11 show that the In718 sequential tests failed directly opposite the punch, it is not certain that this same behavior is exhibited in tests loaded continuously until fracture.

In Figure 4.5 and Figure 4.6, the failed In718 specimens from continuously backed tests show that fracture occurs in the region underneath the punch tip. Yet it is not certain if fracture initiates directly opposite the punch tip or slightly offset from this location. However, because fracture is observed directly opposite the punch tip in the In718 sequential tests as well as in the tests on the other materials, it seems probable that fracture would initiate in this same location in these tests as well. This region would experience the greatest amount of biaxial in-plane tension stresses, which would tend to encourage fracture. Therefore, the location on the back surface of the specimen directly opposite the punch tip is taken as the fracture location for Al2024, Ti64, and

In718. The stress state parameters and equivalent plastic strain are calculated at the element in the LS-DYNA simulations that corresponds to this location.

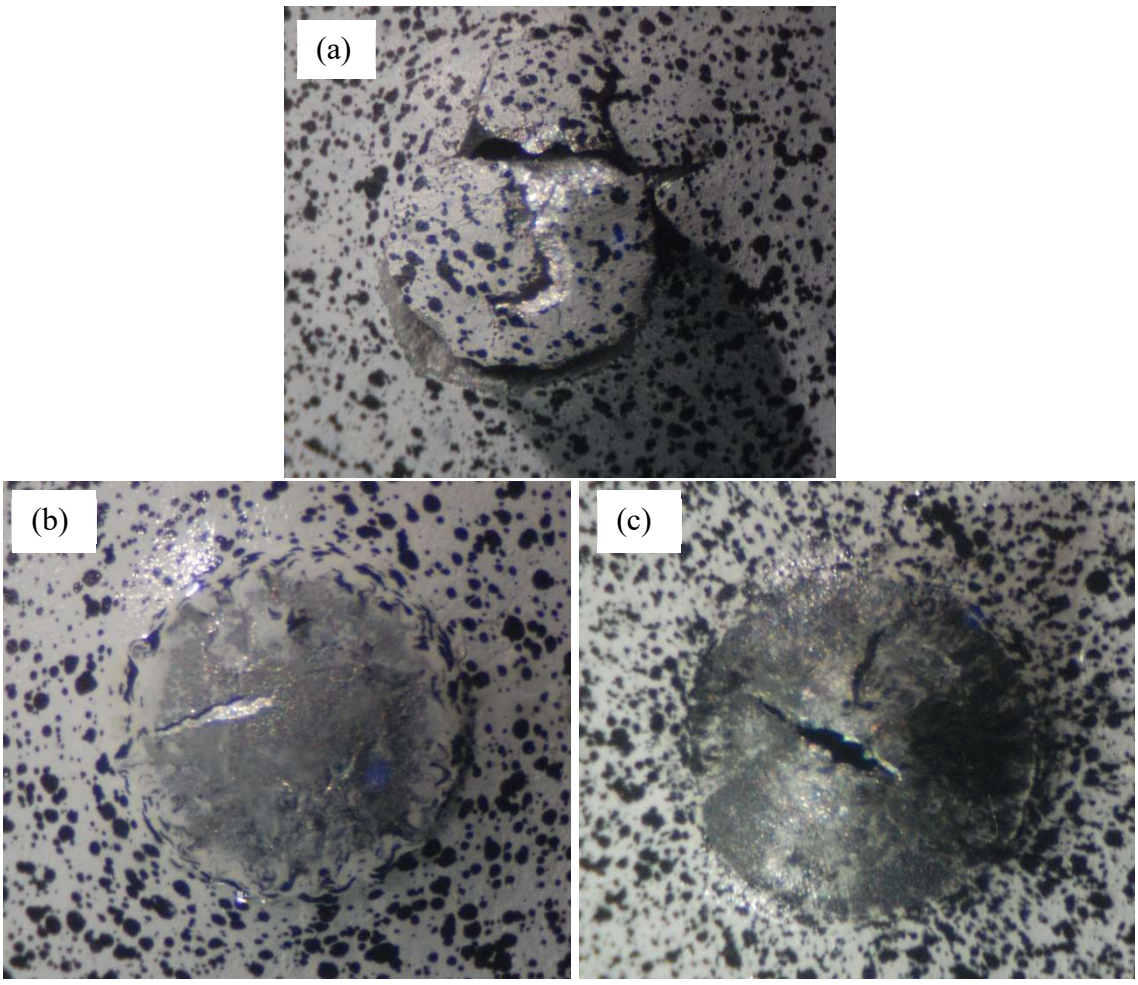

Figure 4.8 Post-test Al2024 hemispherical punch test specimens showing fracture locations for (a) unbacked, (b) 1.27 mm backing plate and (c) 2.54 mm backing plate

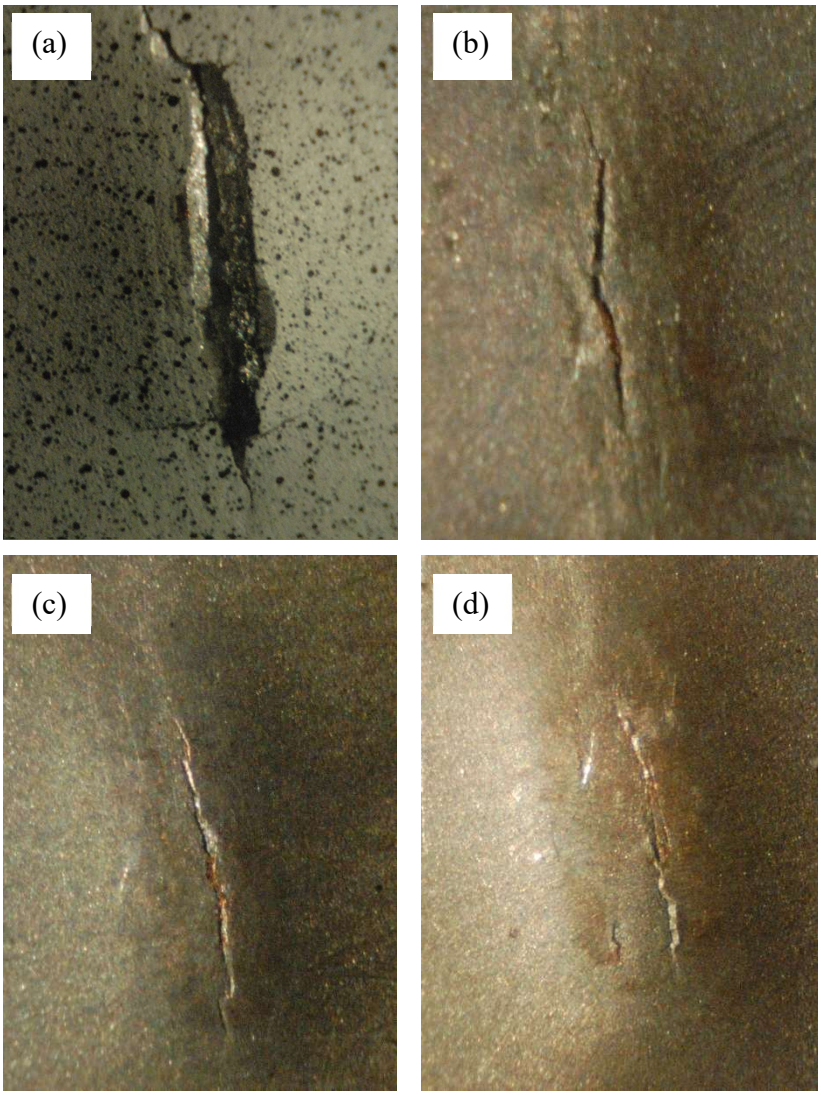

Figure 4.9 Post-test Al2024 elliptical punch test specimens showing fracture locations for (a) unbacked, (b) 1.575 mm backing plate, (c) 2.36 mm backing plate and (d) 3.175 mm backing plate

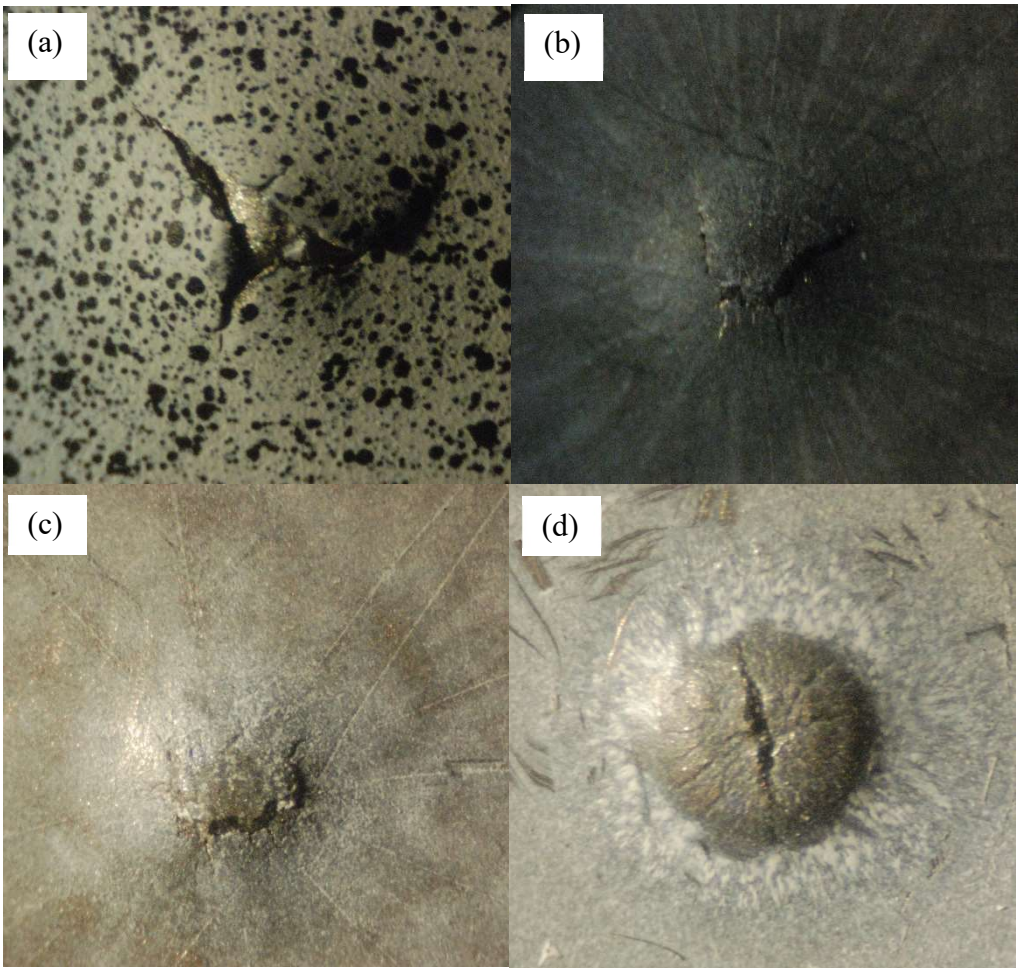

Figure 4.10 Post-test Ti64 punch test specimens showing fracture locations for (a) unbacked, (b) 0.889 mm backing plate, (c) 1.27 mm backing plate and (d) 1.83 mm backing plate

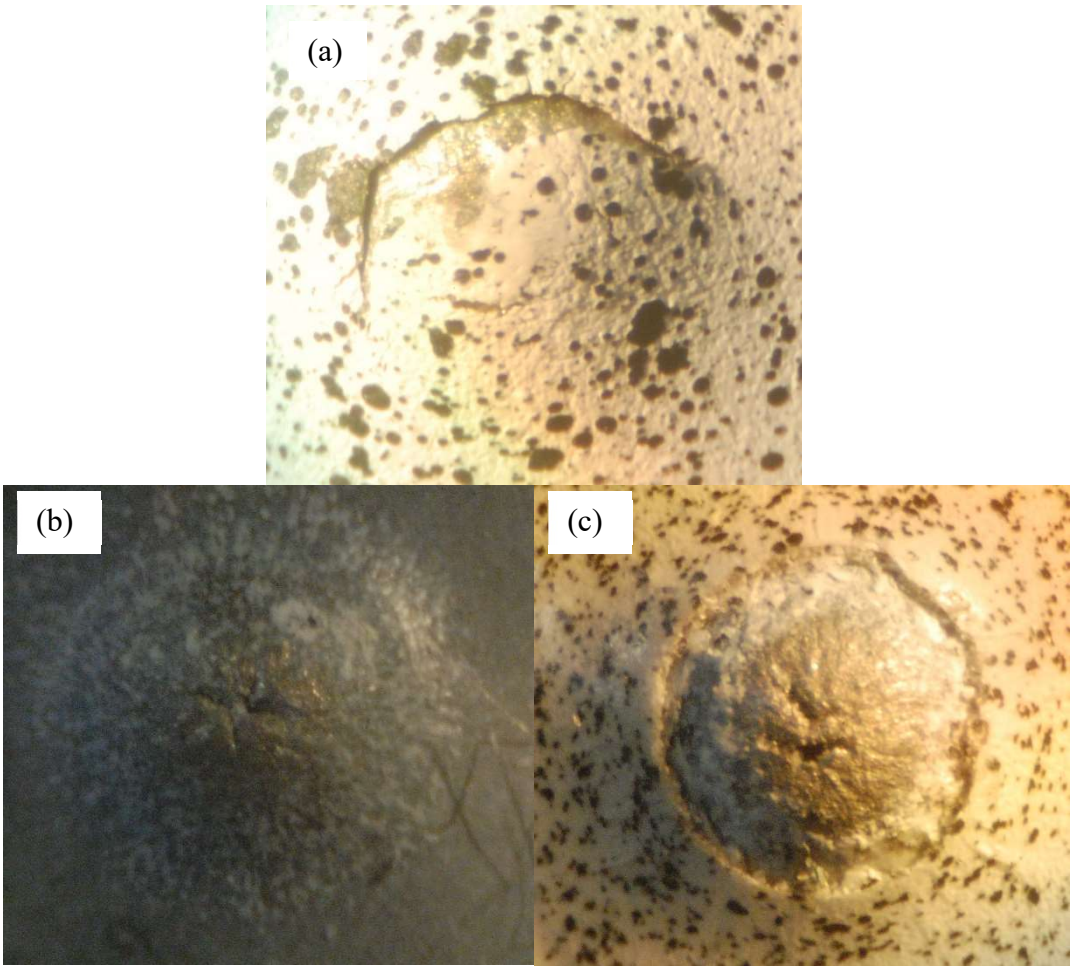

Figure 4.11 Post-test In718 punch test specimens showing fracture locations for (a) unbacked, (b) 1.83 mm backing plate and (c) 2.77 mm backing plate

Acoustic emissions sensing is used to detect fracture for the Al2024 elliptical backed punch tests loaded continuously until fracture. The normalized cumulative energy from the detected AE hits versus the corresponding load is shown in Figure 4.12. The normalized cumulative energy is found by adding the individual energy of each AE hit (i.e., the area between the waveform and the baseline) to the energy detected from each previous AE hit as the test progresses. These values are then divided by the final value of cumulative energy to create the normalized cumulative energy. Sharp jumps or spikes in the normalized cumulative energy can be used to determine when fracture has occurred, as the vibrations and detected AE hits due to material fracture tend to have higher amplitude and longer duration (and consequently higher energy) than those due to noise or friction.

It can clearly be seen that spikes in detected energy occur at an average load of 3,043 N for tests with 1.575 mm backing plates, 4,000 N with 2.36 mm backing plates, and 5,969 N with 3.175 mm backing plates. These correspond to the same loads when fracture is visibly observed in the same tests loaded sequentially until fracture.

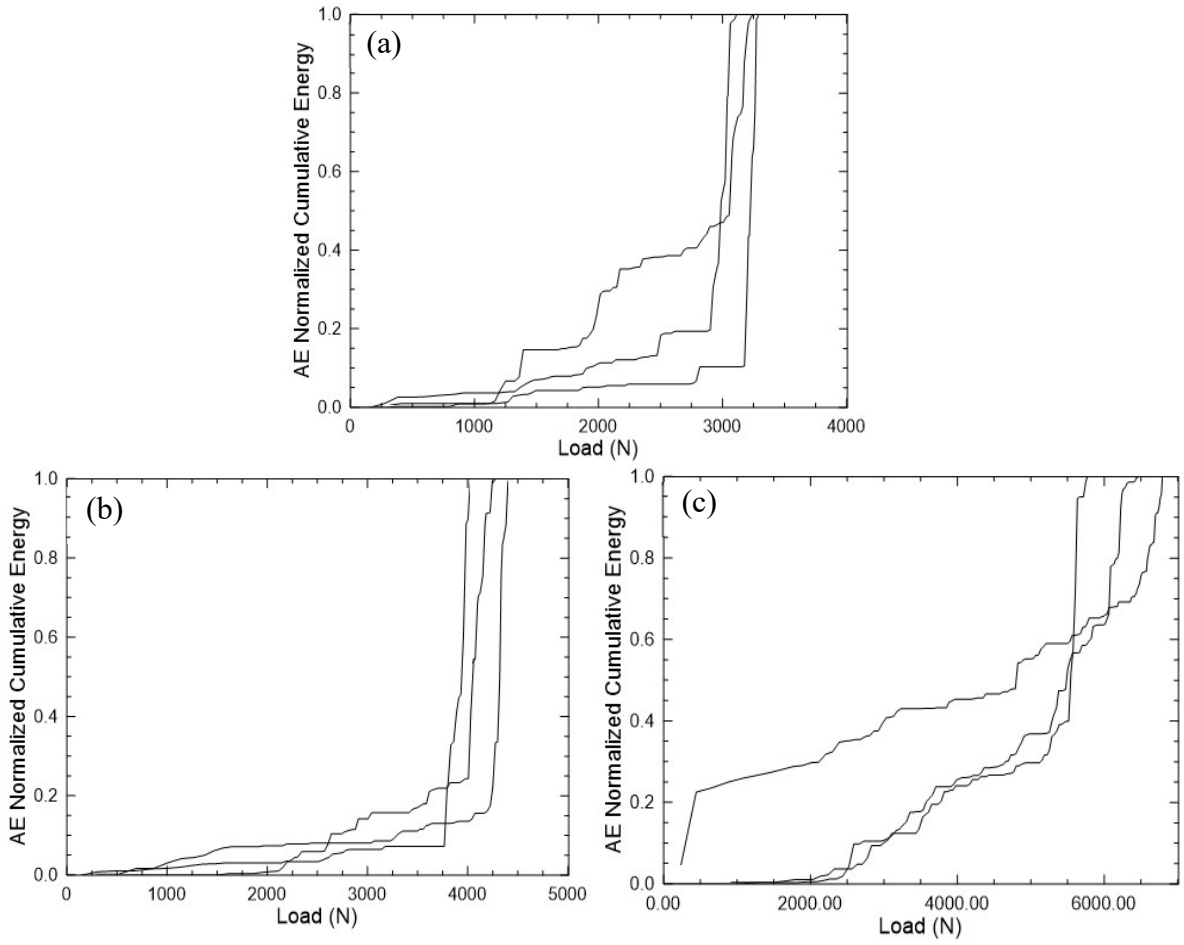

Figure 4.12 Normalized cumulative energy vs. load from acoustic emissions data of Al2024 elliptical backed punch tests for (a) 1.575 mm thick, (b) 2.36 mm and (c) 3.175 mm thick backing plates

DIC is used to obtain strain data on the back surface of the specimens during continuous loading until fracture for the unbacked tests, and during sequential interrupted tests when a backing plate is used. The nature of the backed tests, where the speckle pattern on the back surface of the specimen is being compressed into the backing plate, can cause the speckle pattern to be degraded.

This makes obtaining useable DIC data difficult, especially at the center area of displacement directly opposite the punch where the force and contact with the backing plate is concentrated. Therefore, the DIC strain data is extracted along centerlines across the specimen, as illustrated in Figure 4.13. A single centerline is used for the hemispherical punch tests since these tests are axisymmetric, and two centerlines are used for the elliptical punch tests that are aligned with the major and minor diameters of the elliptical shaped punch.

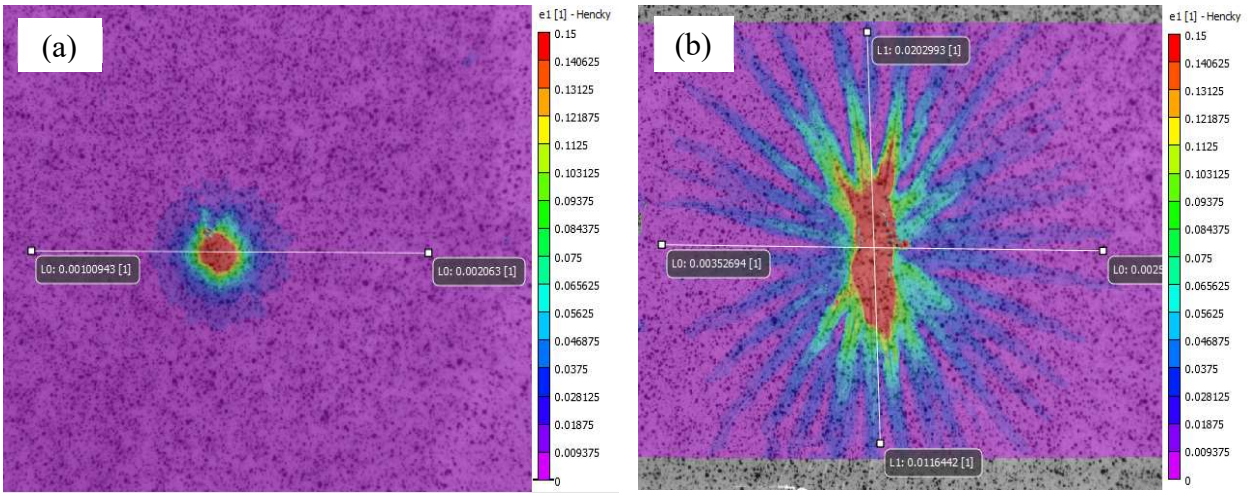

Figure 4.13 Centerlines along which DIC data is extracted for (a) hemispherical and (b) elliptical punch tests

The DIC data along these centerlines from the experiments is then compared to the LS-DYNA simulations at the same load level. The VSGL and element mesh size are compared, and if these values are not the same then the local DIC strains are averaged over the corresponding number of data points such that the physical area the localized strain is calculated over matches between the test and simulations. The comparison between the DIC and simulation strains is shown in Figure 4.14 - Figure 4.18. The single centerline for the Al2024, Ti64, and In718 hemispherical punch tests are shown in Figure 4.14, Figure 4.17, and Figure 4.18. This centerline comparison along the major diameter of the Al2024 elliptical punch tests is shown in Figure 4.15, and that of the minor diameter in Figure 4.16.

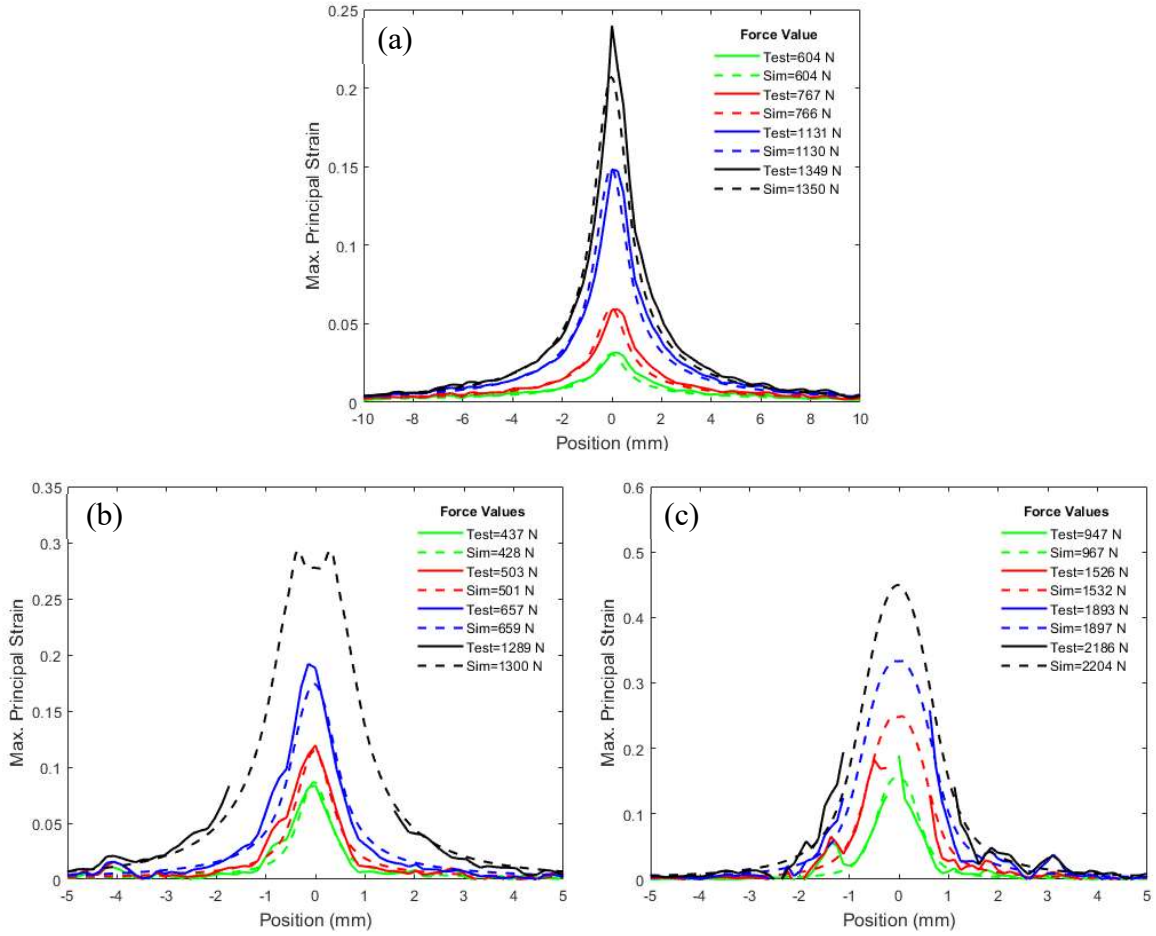

Figure 4.14 Comparison of experimental and simulated maximum principal strain on the back surface of Al2024 hemispherical backed punch test specimens for (a) unbacked, (b) 1.27 mm and (c) 2.54 mm thick backing plates

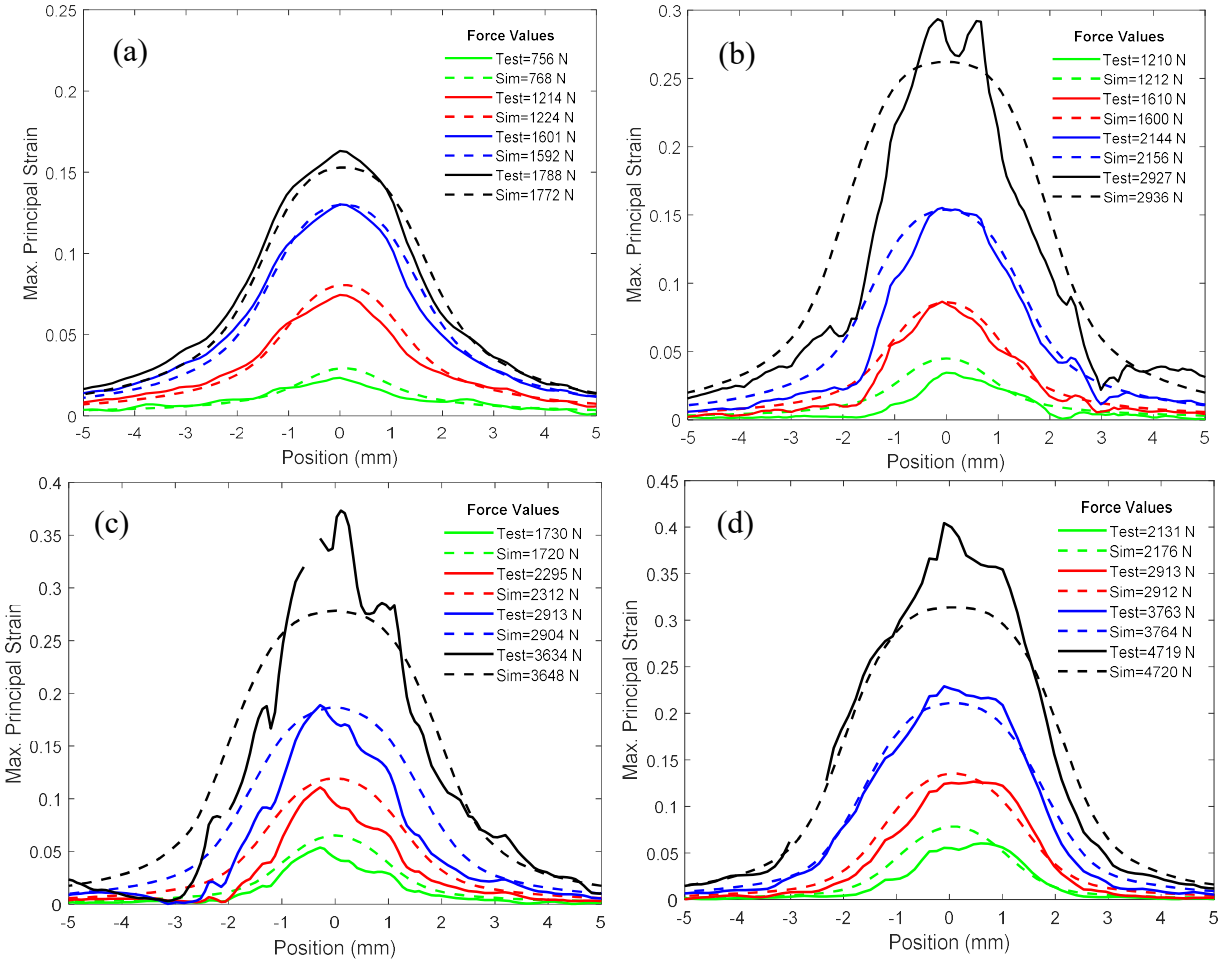

Figure 4.15 Comparison of experimental and simulated maximum principal strain on the back surface of Al2024 elliptical backed punch test specimens aligned with the major punch diameter for (a) unbacked, (b) 1.575 mm thick, (c) 2.36 mm and (d) 3.175 mm thick backing plates

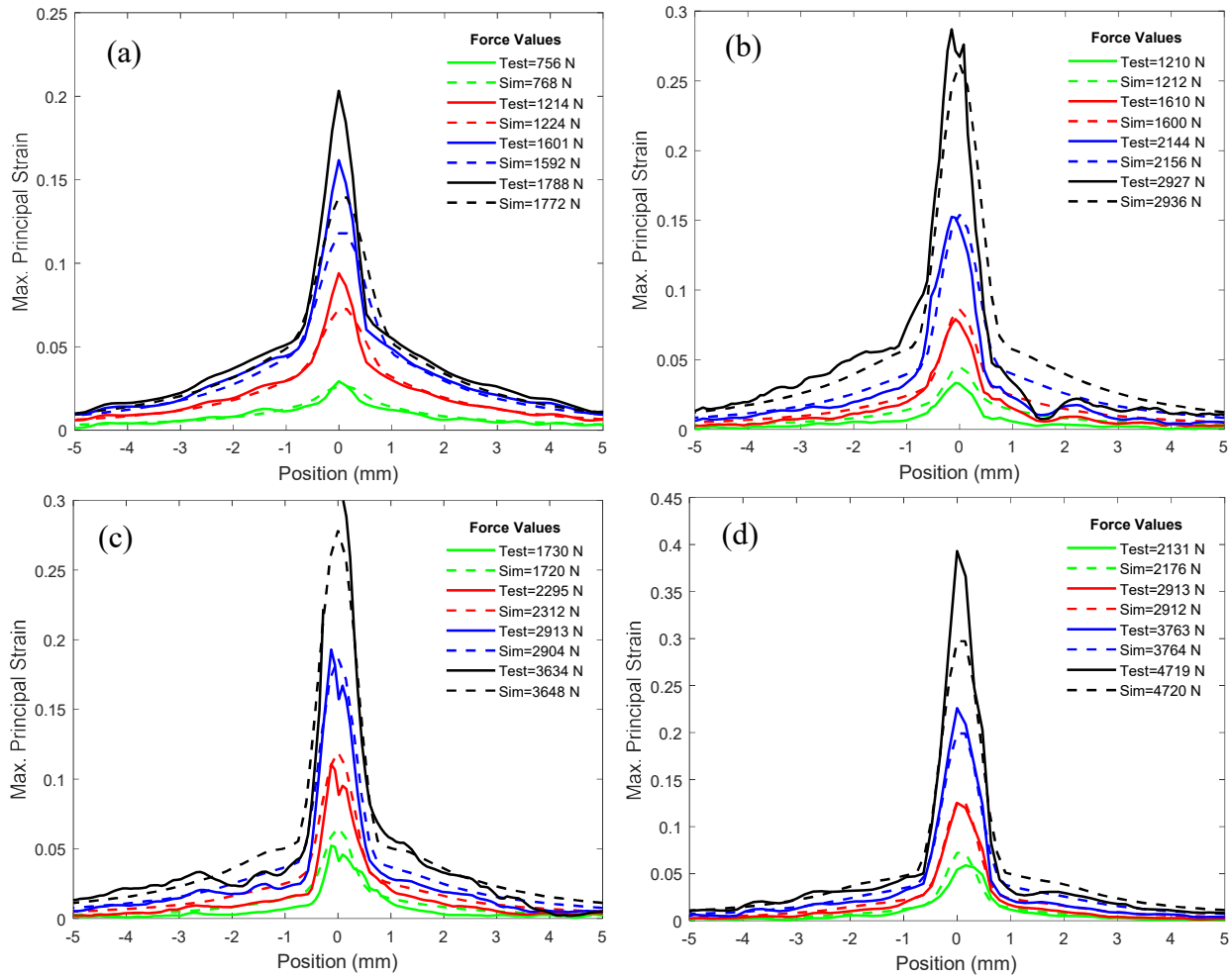

Figure 4.16 Comparison of experimental and simulated maximum principal strain on the back surface of Al2024 elliptical backed punch test specimens aligned with the minor punch diameter for (a) unbacked, (b) 1.575 mm thick, (c) 2.36 mm and (d) 3.175 mm thick backing plates

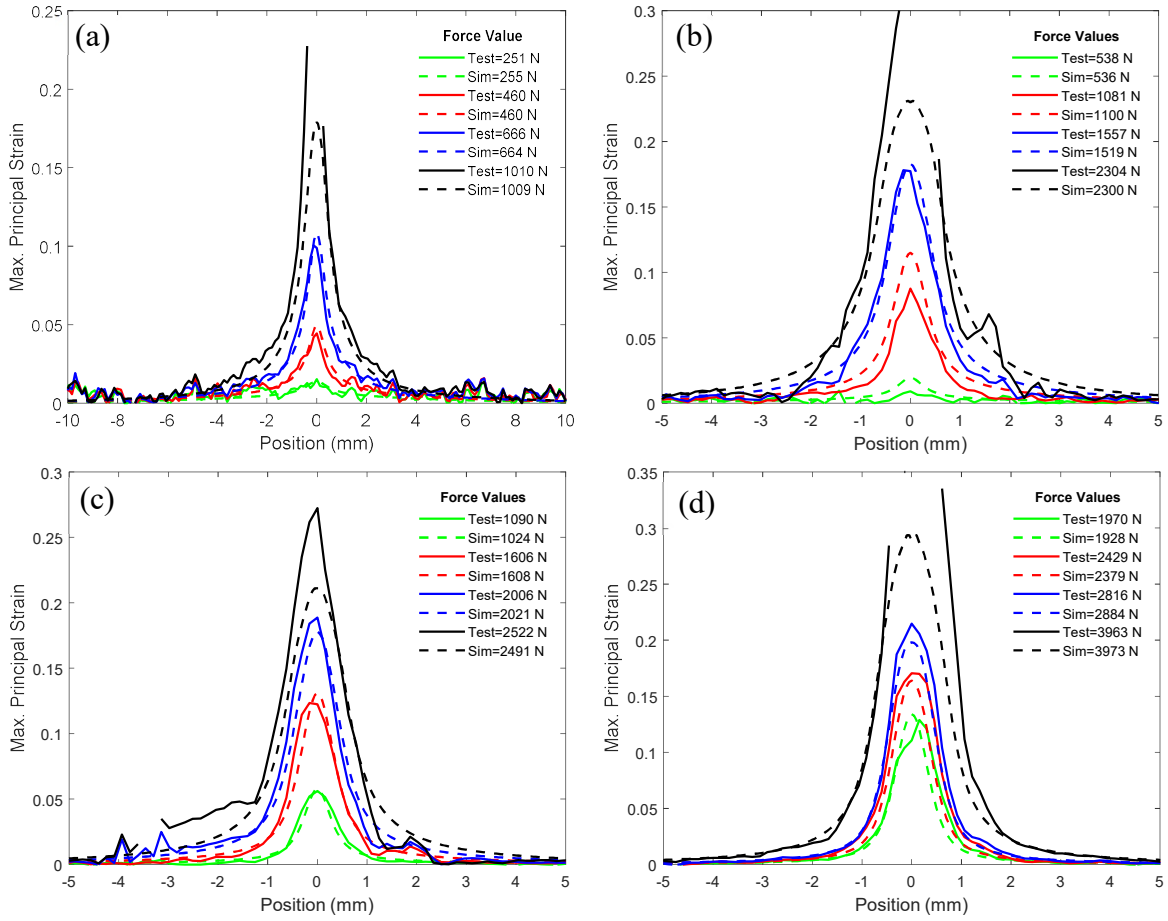

Figure 4.17 Comparison of experimental and simulated maximum principal strain on the back surface of Ti64 hemispherical backed punch test specimens for (a) unbacked, (b) 0.889 mm, (c) 1.27 mm and (d) 1.83 mm thick backing plates

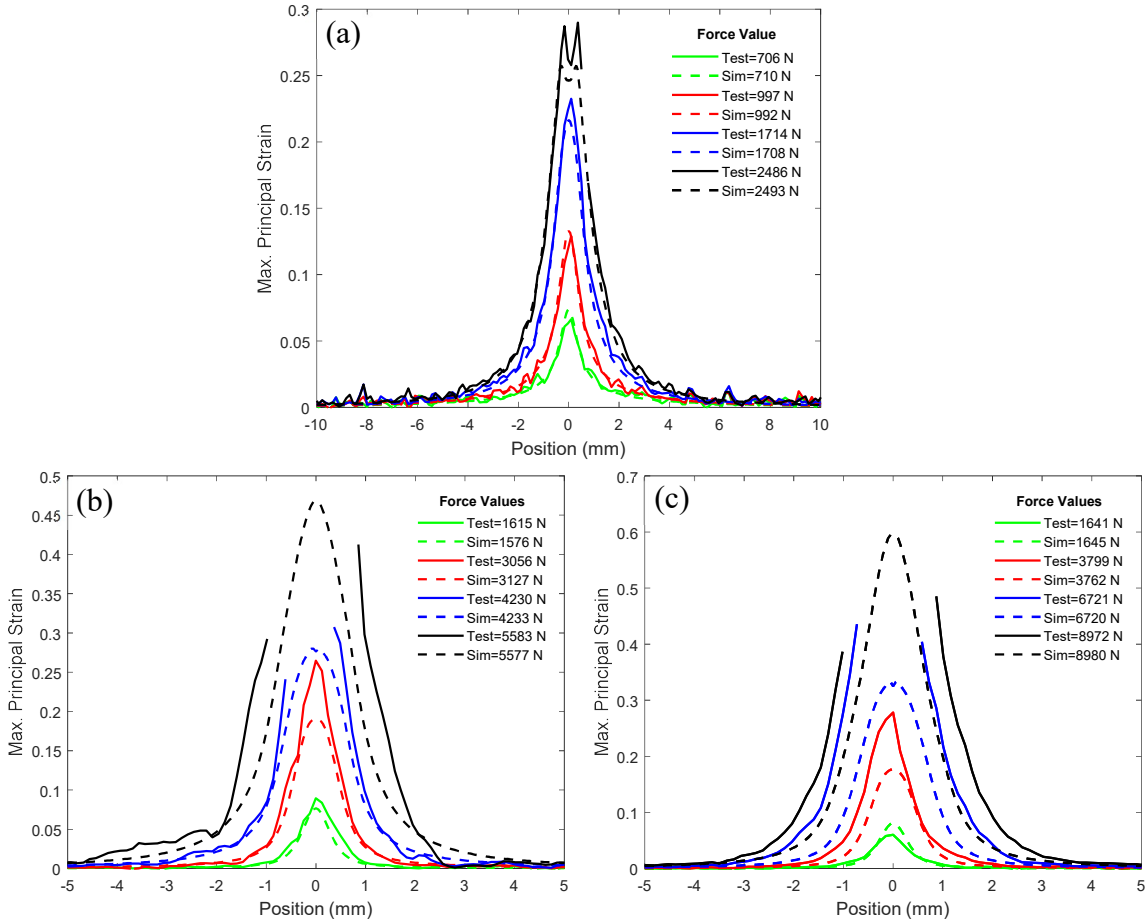

Figure 4.18 Comparison of experimental and simulated maximum principal strain on the back surface of In718 hemispherical backed punch test specimens for (a) unbacked, (b) 1.83 mm and (c) 2.77 mm thick backing plates

Figure 4.14(a) shows excellent agreement between the experimentally measured and simulated strains for the Al2024 unbacked hemispherical punch test. Figure 4.14(b) and (c) shows initial agreement between the Al2024 hemispherical backed punch experiments and the simulations for the first several loading increments. At later loading increments DIC data dropout occurs in the region directly opposite the punch, due to degradation of the speckle pattern from contact with the backing plate. However, DIC data remains available farther away from the center of the displaced area, and this data continues to agree with the simulation data. Because the simulated and experimental strain agree at all locations where the experimental data is available,

it is reasonable to assume that simulated strain continues to agree with the experimental values in areas where DIC data dropout has occurred. This includes in the center of the displaced area (directly opposite the punch), where fracture occurs.

Similarly, Figure 4.15(a) and Figure 4.16(a) show excellent agreement between the experimental and simulated strain along both the major and minor punch diameters for the unbacked Al2024 elliptical punch tests. Figure 4.15(b-d) and Figure 4.16(b-d), from the Al2024 elliptical sequential backed punch tests, show significantly less data dropout than the Al2024 hemispherical sequential backed punch tests shown in Figure 4.14(b-c). This is due to the addition of the clear cyanoacrylate adhesive layer on top of the speckle pattern in the elliptical punch tests, which allows the speckle pattern to survive longer and DIC data to be obtained for longer during the tests.

However, the DIC and simulation strains in Figure 4.15(b-d) and Figure 4.16(b-d) do not show perfect agreement for the Al2024 elliptical backed punch tests. This is likely due to the inherent difficulties of obtaining high quality DIC data from the sequential backed punch tests. Because the DIC images from the backed tests are taken after interrupted loading increments, there is a comparatively large amount of deformation between subsequent images. This makes it more difficult for the DIC software to track the deformation and accurately calculate the strains. In addition, the clear adhesive protective layer and clear Teflon lubricant coating over the speckle pattern can create optical distortions, which introduce error. In particular, the adhesive tends to crack in a radial pattern at higher loads. This can be seen in Figure 4.13(b), where the lines of higher strain expanding radially outward from the center area correspond to crack lines in the adhesive. In reality, the strains at these locations are not actually higher than the surrounding areas. The higher DIC strains are due to optical distortions caused by the cracks in the adhesive. The

contact forces between the specimen and backing plate can also cause the quality of the speckle pattern to degrade by being rubbed off or smeared. These are all opportunities for the introduction of error in the DIC strain measurements.

While these conditions are not ideal and do create some error in the DIC measurements, the DIC data in Figure 4.15(b-d) and Figure 4.16(b-d) still generally aligns well with the simulation data. Therefore it is reasonable to conclude that the simulated strain values are an accurate reflection of what occurs during the Al2024 elliptical punch tests.

Figure 4.17 shows a similar trend for the Ti64 backed punch tests as is observed in Figure 4.14 (with the Al2024 hemispherical backed punch tests). The experimental and simulated data agree well, and due to the protective adhesive layer the DIC data survives until relatively late in the Ti64 sequential tests. Therefore, it can be reasonably assumed that the simulation is accurately capturing the Ti64 material response, including the local strain at the fracture location.

Figure 4.18(a) shows excellent agreement between the In718 DIC data and the simulation for the unbacked test scenario. However, the backed tests shown in Figure 4.18(b) and (c) only appear to agree well with the simulation data at low loads early in the tests. The DIC strain then increases above the simulated value at intermediate loads and drops out in the center region at higher loads (even with the protective adhesive layer). This discrepancy between the test and simulation data, plus the premature data dropout, is likely due to the fact that the In718 sequential tests used to obtain this DIC strain data exhibited premature fracture compared to the continuous tests.

Because the simulated specimens are loaded continuously until fracture, it is expected that these simulations would match the experiments that are also loaded continuously until fracture.

The Al2024 and Ti64 experiments showed very similar behavior force-displacement behavior between the continuous and sequential experiments (Figure 4.1 - Figure 4.3). Therefore, it is reasonable to expect that the simulations for those materials will match both the sequential and continuous test data. However, this does not hold true for In718. The In718 backed punch simulations agree with the continuous test force-displacement data shown in Figure 4.4(b) and (c), yet the simulation and continuous test force-displacement curves both deviate from the sequential test curves (especially at higher loads). Therefore it would be reasonable to expect the In718 backed punch test simulations will initially match the sequential test data at low loads (when the force vs. displacement curves align), but not at higher loads. Indeed, this is exactly what is observed for the strain data in Figure 4.18(b) and (c). The strain initially matches at lower loads, then begins deviating as the load increases, before at higher loads the DIC data drops out. Therefore while it can be concluded from the strain data in Figure 4.18(a) that the In718 simulations accurately reflect the unbacked test data, the same cannot be concluded for the In718 backed punch tests based upon the strain data in Figure 4.18(b) and (c).

An additional complication occurs when simulating the In718 backed tests due to the extreme ductility that In718 exhibits in the backed tests. As noted previously, the In718 specimen becomes extremely thin before fracture occurs in the backed tests. Material fracture in the continuous tests is not observed until after a punch displacement of 3.55 mm and a load of 7,796 N with a 1.83 mm backing plate, and after a punch displacement of 4.49 mm and load of 13,674 N with a 2.77 mm backing plate. Attempting to simulate these tests up until this point results in highly flattened elements and non-physical behavior, as shown in Figure 4.19 and Figure 4.20.

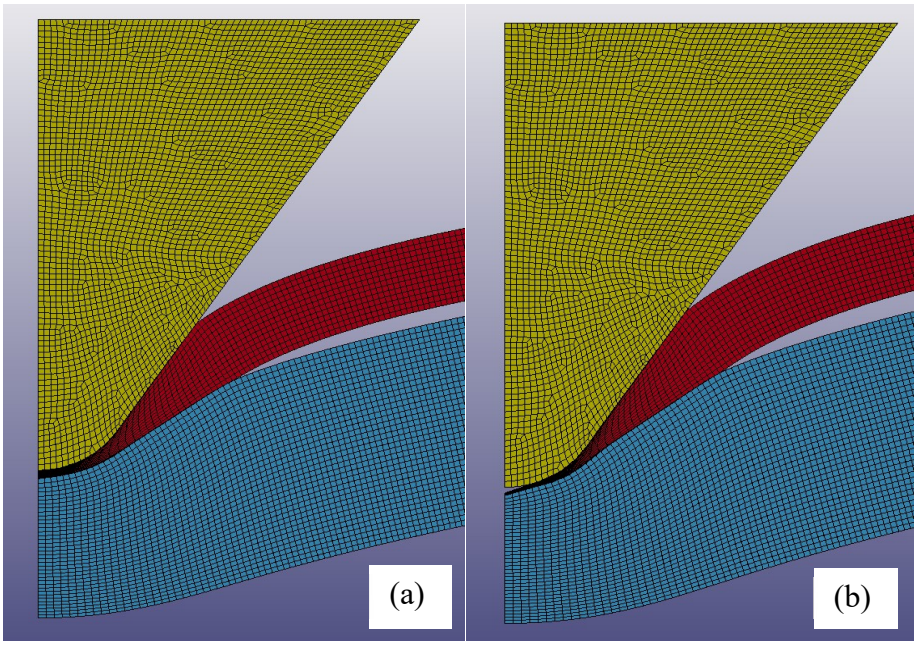

Figure 4.19 LS-DYNA simulation of In718 1.83 mm backed punch test at (a) punch displacement of 3.2 mm, before elements become distorted and (b) punch displacement of 3.55 mm, after elements become distorted due to extreme thinning

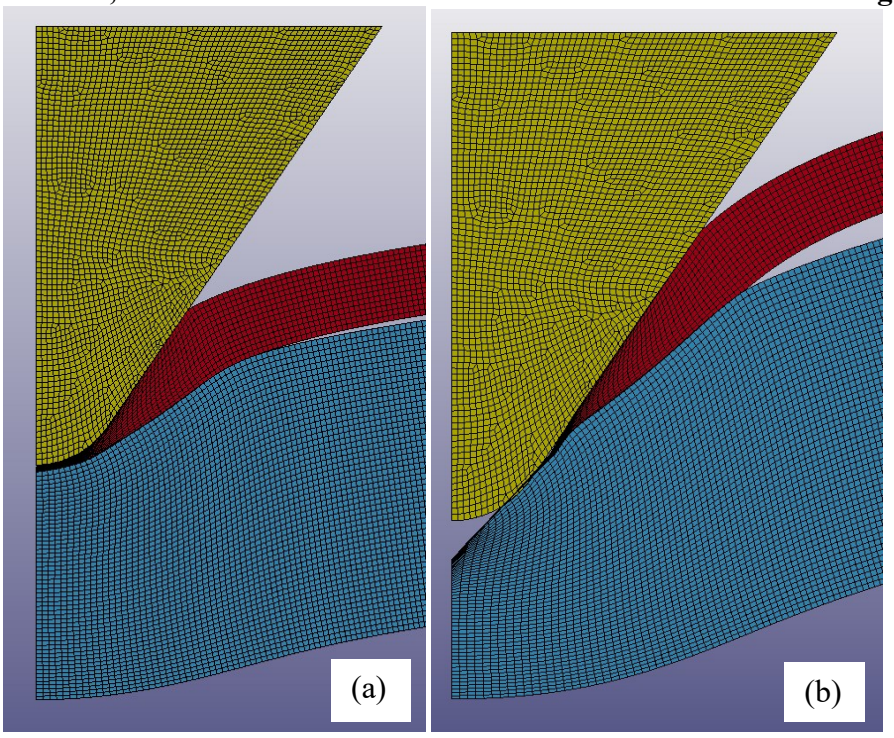

Figure 4.20 LS-DYNA simulation of In718 2.77 mm backed punch test showing (a) punch displacement of 2.75 mm, before elements become distorted and (b) punch displacement of 4.5 mm, after elements become distorted due to extreme thinning

The 2D simulation elements shown in Figure 4.19 and Figure 4.20 have an initial geometry of 0.05 x 0.05 mm. As the punch advances into the specimen, it compresses and flattens the elements underneath it. At a punch displacement of 3.55 mm in the 1.83 mm backed punch simulation (the last point before fracture is observed in the continuous tests), the element at the fracture location has been compressed to a geometry of 0.0021 x 0.23 mm. In the 2.77 mm backed punch simulation, at a punch displacement of 4.5 mm (the last point before fracture is observed in the continuous tests), the element at the fracture location has a geometry of 0.00054 x 0.73 mm.

As the element lengths become similar in size to the punch radius (0.8 mm), only one or two elements remain underneath the punch. This results in too few contact points between the punch and the specimen, and the simulated specimen material can no longer conform to match the shape of the punch. Instead, the elements directly underneath the punch begin to protrude at an angle tangential to the punch radius. As can be seen in the above figures, particularly in Figure 4.20(b), this results in non-realistic behavior. A gap forms between the specimen material and the punch tip, and the specimen elements are pushed into the backing plate at a severe angle. This is clearly non-physical behavior that is no longer representative of the localized In718 material behavior that occurs in test.

Therefore the In718 simulation results cannot be used to determine the stress state parameters and equivalent plastic strain all the way up to the observed point of fracture in the experiments. However, the simulation results can be truncated before the results becomes non-physical, and used to determine a lower limit on the equivalent plastic fracture strain under these conditions. Such non-physical behavior is not observed in the simulations of Al2024 and Ti64. Those materials are much less ductile at these stress states than In718, and material fracture occurs before the simulated Al2024 and Ti64 elements become distorted. Therefore the simulation results

for Al2024 and Ti64 can be used to determine the stress state parameter and equivalent plastic strain all the way up to the observed point of fracture in the experiments.

In some tests the DIC speckle pattern survives and DIC data at the center of the displaced area where fracture occurs can be obtained. The first and second principal strains measured by DIC at the center point correspond to the two in-plane tension strains. By assuming material incompressibility, meaning the trace of the strain tensor must equal zero, the third principal strain can be calculated as $\varepsilon_3 = -(\varepsilon_1 + \varepsilon_2)$. These strains are shown and compared to the simulated strain values at the same point in Figure 4.21 - Figure 4.24.

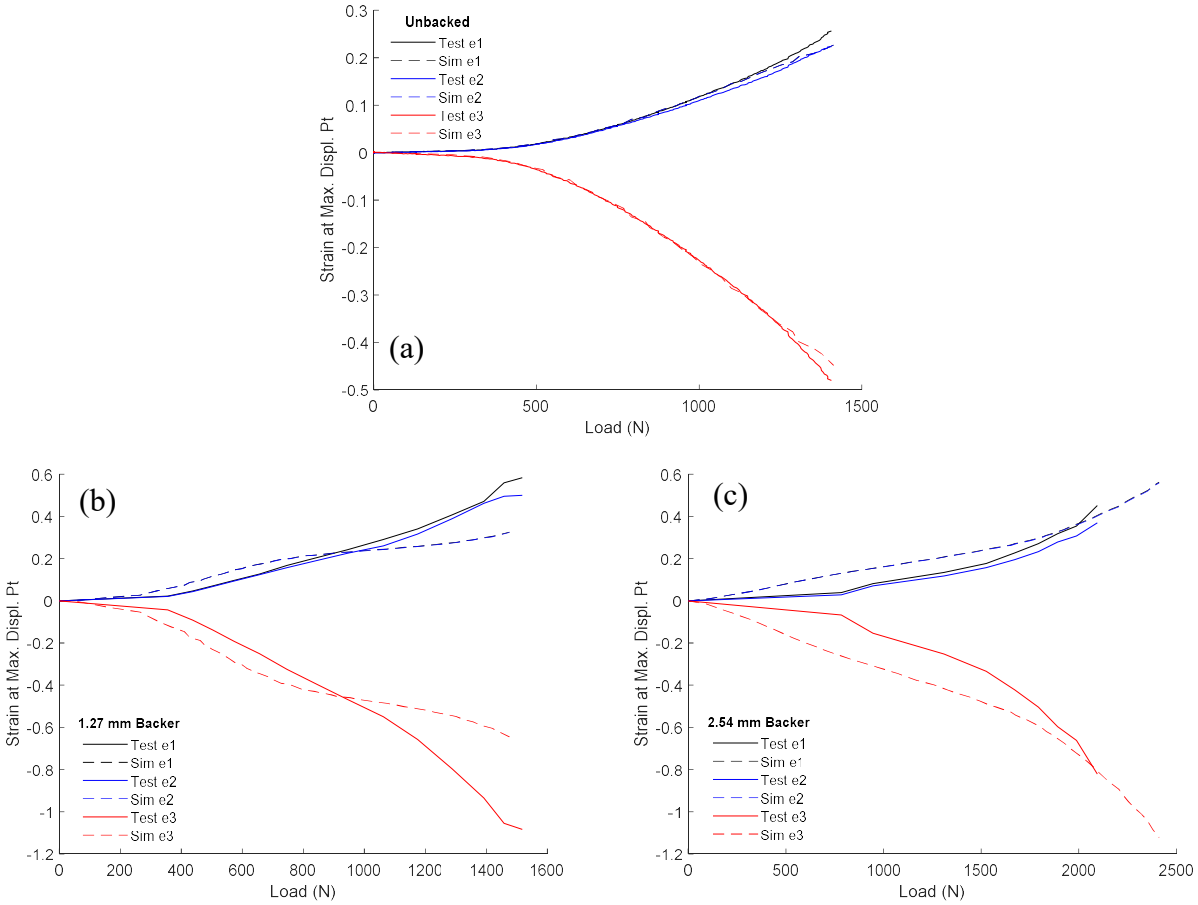

Figure 4.21 Measured and simulated principal strains at the maximum displacement point for Al2024 hemispherical backed punch tests for (a) unbacked, (b) 1.27 mm and (c) 2.54 mm thick backing plates

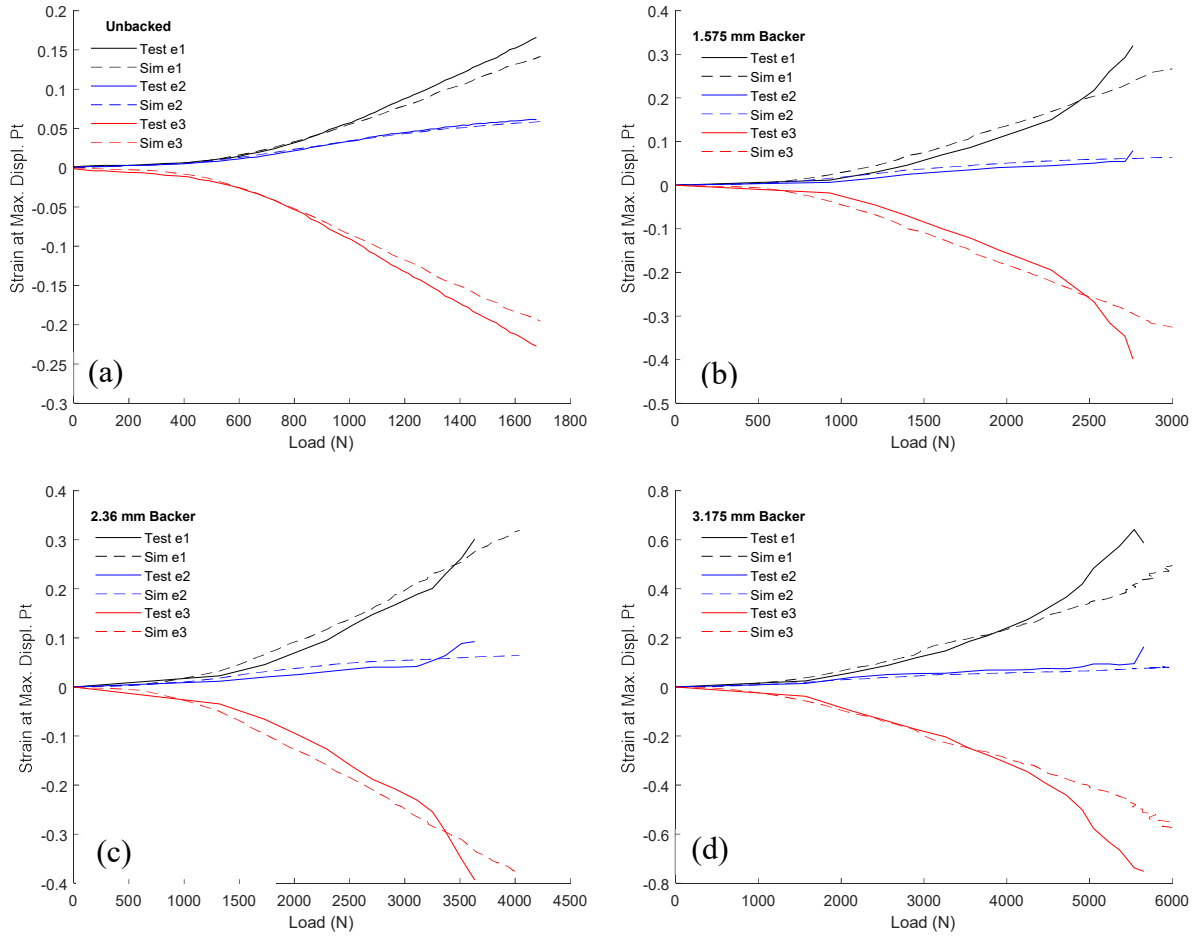

Figure 4.22 Measured and simulated principal strains at the maximum displacement point for Al2024 elliptical backed punch tests for (a) unbacked, (b) 1.575 mm thick, (c) 2.36 mm and (d) 3.175 mm thick backing plates

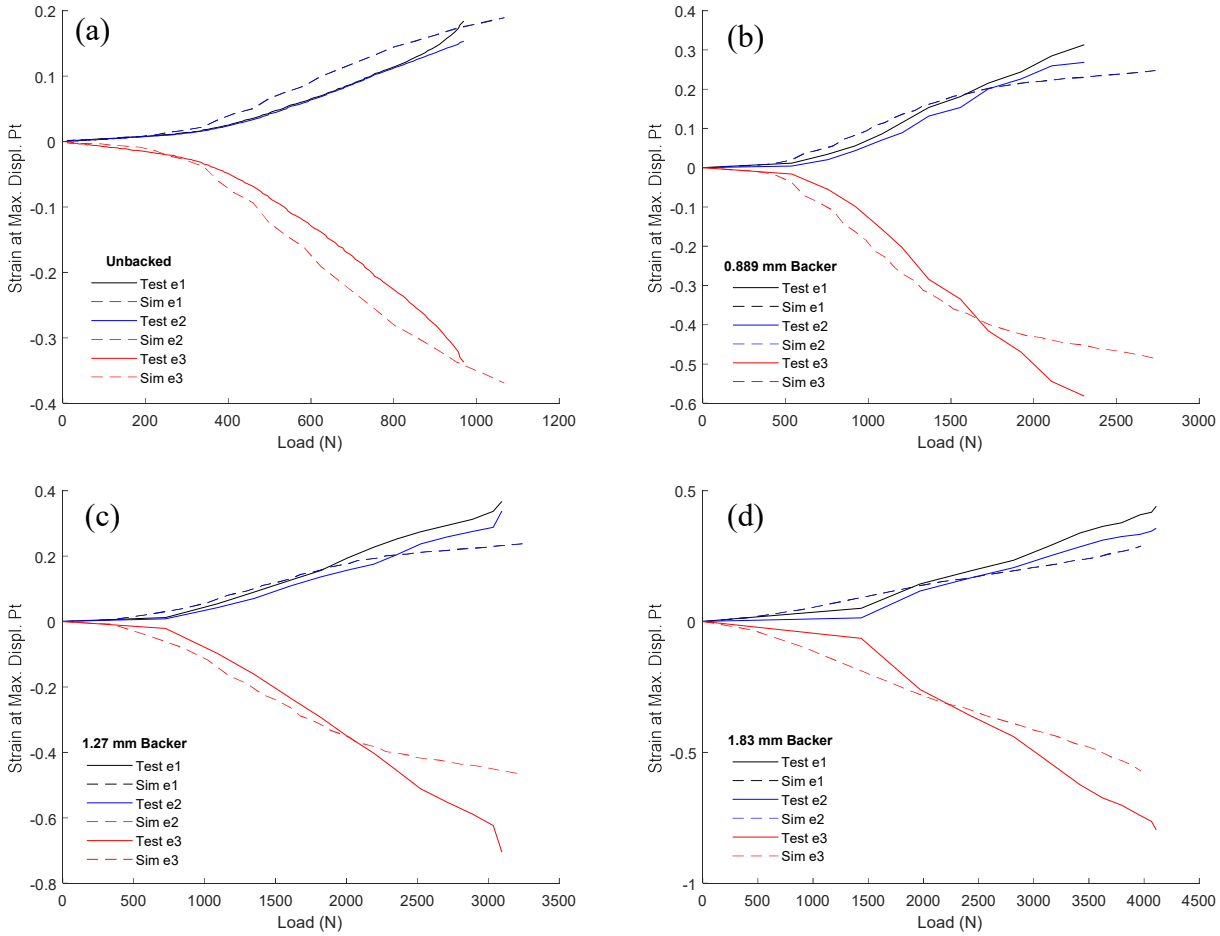

Figure 4.23 Measured and simulated principal strains at the maximum displacement point for Ti64 hemispherical backed punch tests for (a) unbacked, (b) 0.889 mm, (c) 1.27 mm and (d) 1.83 mm thick backing plates

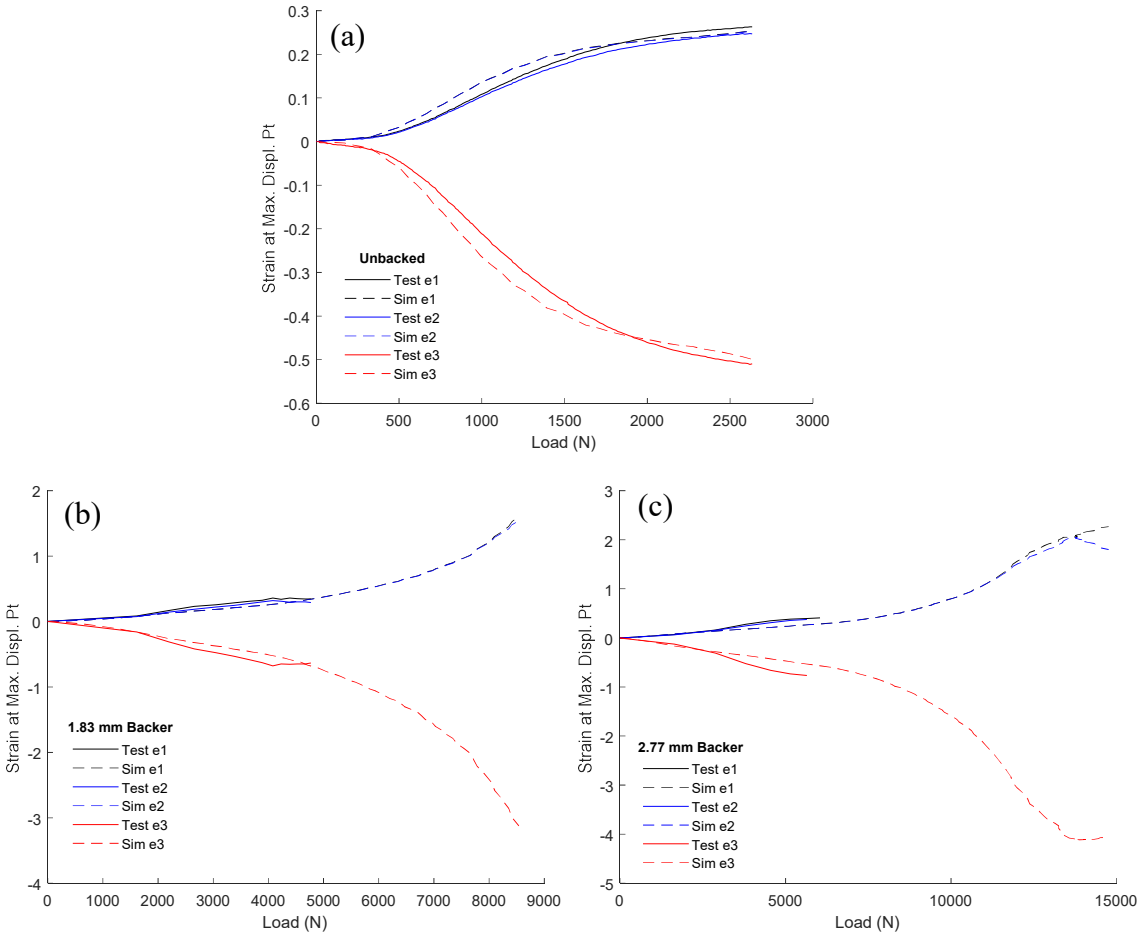

Figure 4.24 Measured and simulated principal strains at the maximum displacement point for In718 hemispherical backed punch tests for (a) unbacked, (b) 1.83 mm and (c) 2.77 mm thick backing plates

The DIC data from the Al2024 unbacked hemispherical punch test shown in Figure 4.21(a) agrees well with the simulated strain data. The Al2024 hemispherical backed punch test data in Figure 4.21(b) and (c) does not align perfectly with the simulated strain data. This is not surprising, for the same reasons that the Al2024 DIC strain data in Figure 4.14(b) and (c) does not perfectly match the simulation data (e.g., the DIC images are taken after interrupted loading increments, optical distortions due to the clear Teflon lubricant, and speckle pattern degradation due to contact with the backing plate). However, the experimental and simulated principal strains in Figure 4.21 (b) and (c) follow the same general trends, supporting the assumption that the simulated material

behavior is the same as the actual material behavior in these experiments. These same conclusions can be drawn from Figure 4.22 and Figure 4.23 for the Al2024 elliptical punch tests and the Ti64 punch tests.

In Figure 4.24(a), the experimental and simulated strains agree very well for the In718 unbacked punch tests. For the In718 backed tests shown in Figure 4.24(b) and (c), the experimentally observed principal strains align well with the simulated values initially, before the DIC data drops out and the experimental strain can no longer be determined. This DIC data dropout occurs much sooner in the In718 backed tests than in tests with the other materials. This is likely due to the higher compression force in the In718 experiments, which causes the speckle pattern to degrade sooner. It is unlikely that the DIC data dropout in Figure 4.24(b) and (c) is caused by the premature specimen fracture that occurs in the In718 sequential backed tests. In Figure 4.24(b), (1.83 mm sequential backed test), DIC data is unavailable after a load of approximately 4,800 N, yet fracture is not observed until an average load of 5,507 N for these tests. Similarly in Figure 4.24(c), (2.77 mm sequential backed test) data dropout occurs after approximately 6,000 N, yet fracture is not observed until 8,658 N.

This behavior is in line with the conclusions drawn from Figure 4.4(b-c) and Figure 4.18(b-c), namely that the LS-DYNA simulations initially agree with the In718 sequential backed test data. However as noted previously, the In718 sequential test behavior deviates from that of the continuous tests and the simulations as the experiments progress.

The maximum principal strains shown in Figure 4.21 - Figure 4.24 can be used to determine the equivalent plastic strain, $\bar{\varepsilon}^p$, which is defined as:

$$\bar{\varepsilon}^p = \int d\bar{\varepsilon}^p = \int \left(\frac{2}{3} d\varepsilon_{ij}^p d\varepsilon_{ij}^p\right)^{1/2}, \tag{4-1}$$

where $d\varepsilon_{ij}^{p}$ is an element of the plastic strain increment tensor. Using a strain increment tensor derived solely from the principal strains, this formula can be re-written as

$$\bar{\varepsilon}^{p} = \sqrt{\frac{2}{3}} \int \left(\left(\frac{d\varepsilon_1}{dt} \right)^2 + \left(\frac{d\varepsilon_2}{dt} \right)^2 + \left(\frac{d\varepsilon_3}{dt} \right)^2 \right)^{1/2} dt \,. \tag{4-2}$$

These calculated values of the equivalent plastic strain are compared to the simulated values in Figure 4.25 - Figure 4.28. These figures also show the simulated Lode parameter and triaxiality at the maximum displacement point.

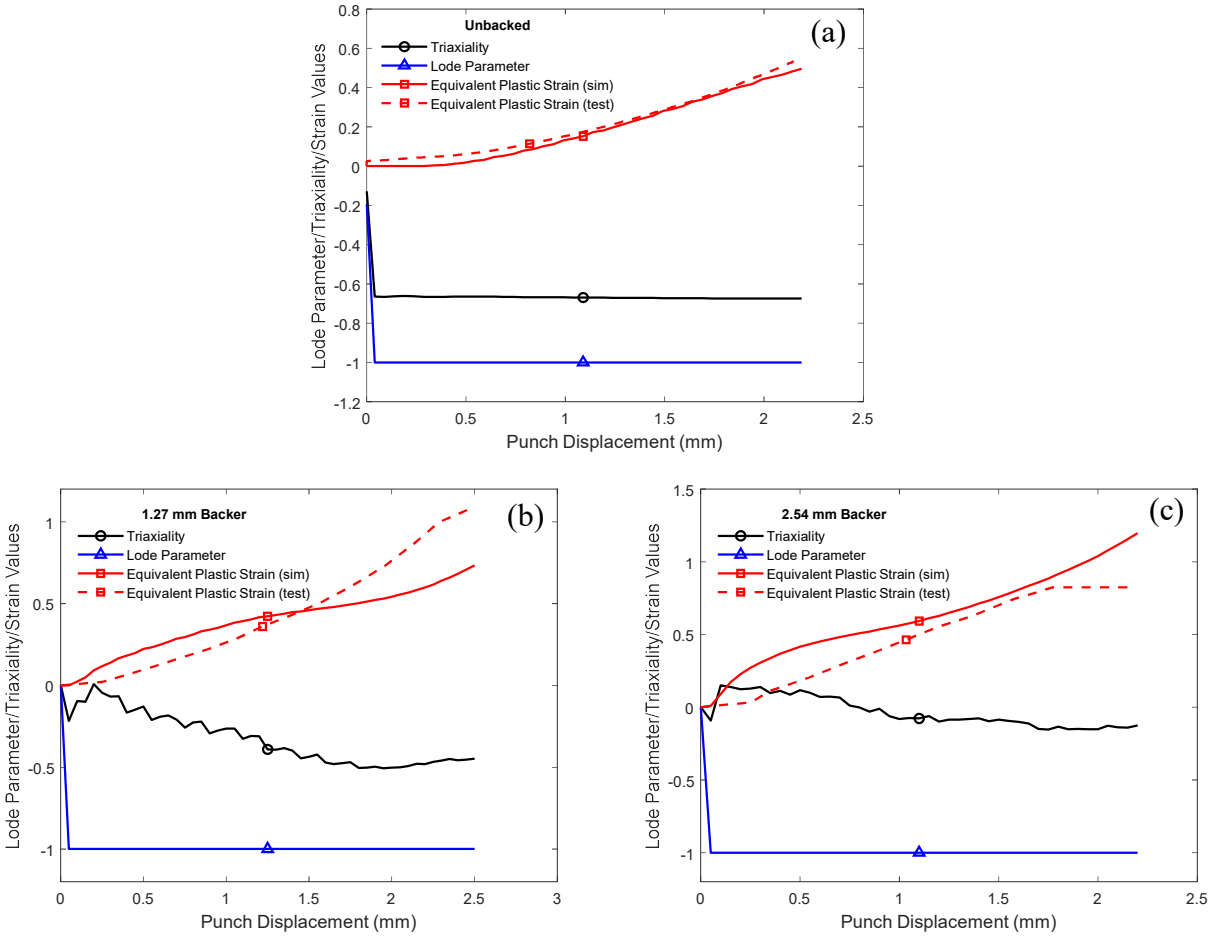

Figure 4.25 Equivalent plastic strain, triaxiality, and Lode parameter at the maximum displacement point for Al2024 hemispherical backed punch tests for (a) unbacked, (b) 1.27 mm and (c) 2.54 mm thick backing plates

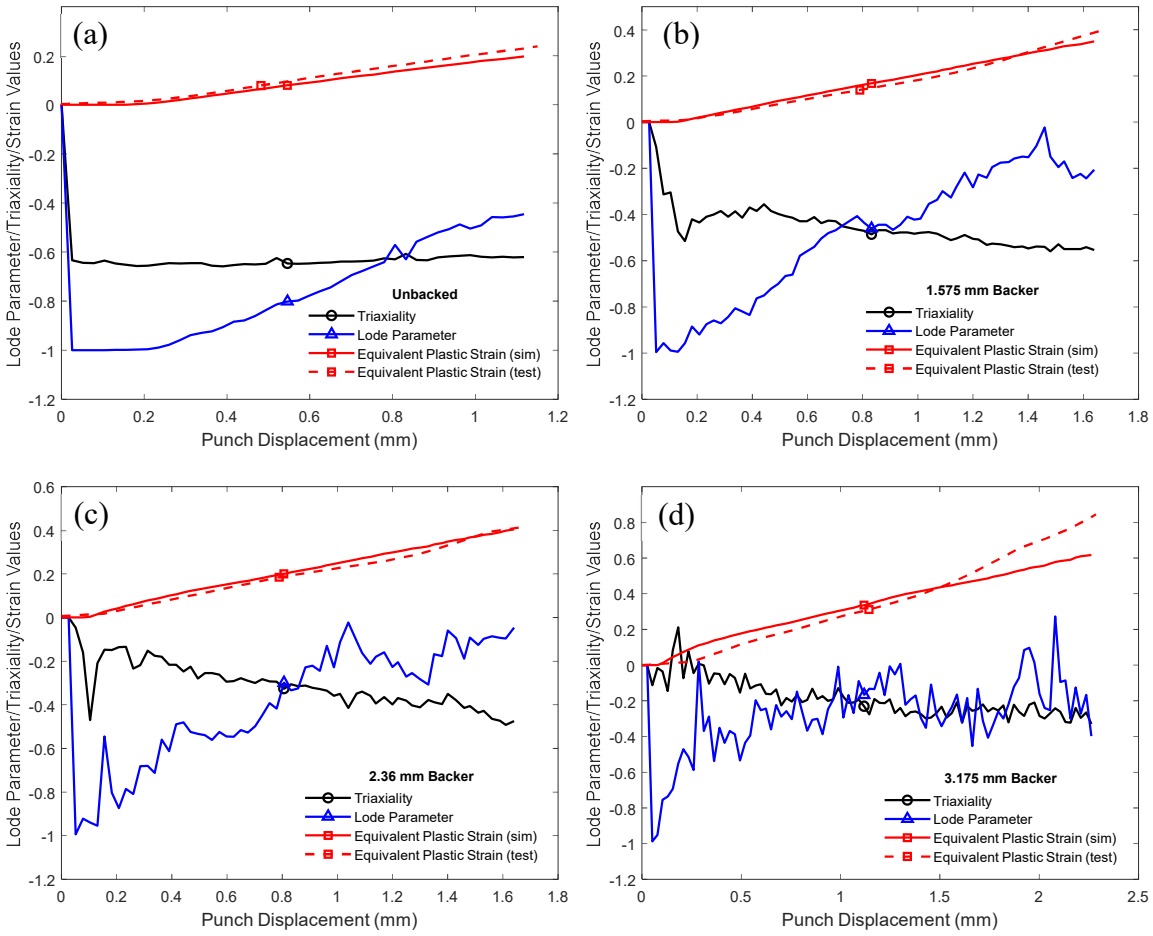

Figure 4.26 Equivalent plastic strain, triaxiality, and Lode parameter at the maximum displacement point for Al2024 elliptical backed punch tests for (a) unbacked, (b) 1.575 mm thick, (c) 2.36 mm and (d) 3.175 mm thick backing plates

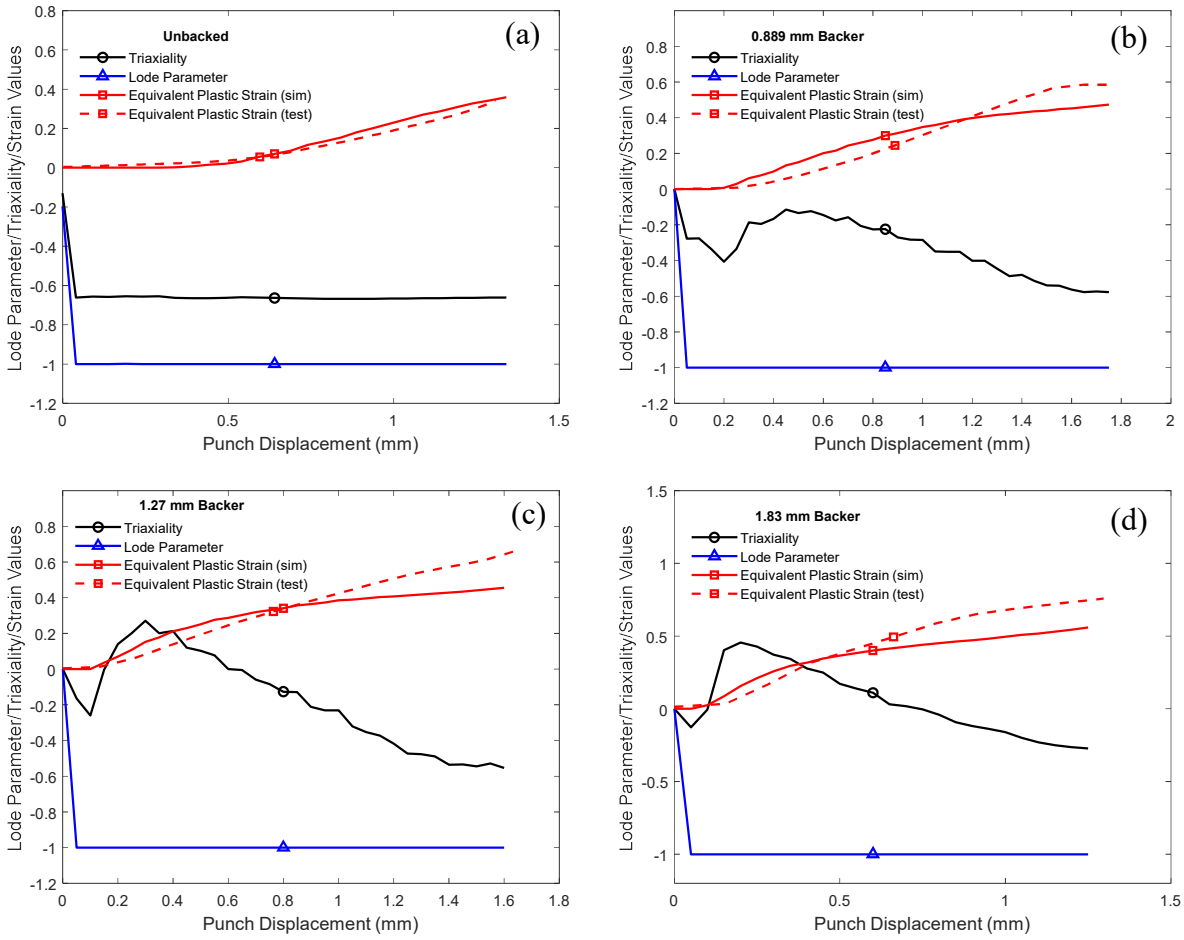

Figure 4.27 Equivalent plastic strain, triaxiality, and Lode parameter at the maximum displacement point for Ti64 hemispherical backed punch tests for (a) unbacked, (b) 0.889 mm, (c) 1.27 mm and (d) 1.83 mm thick backing plates

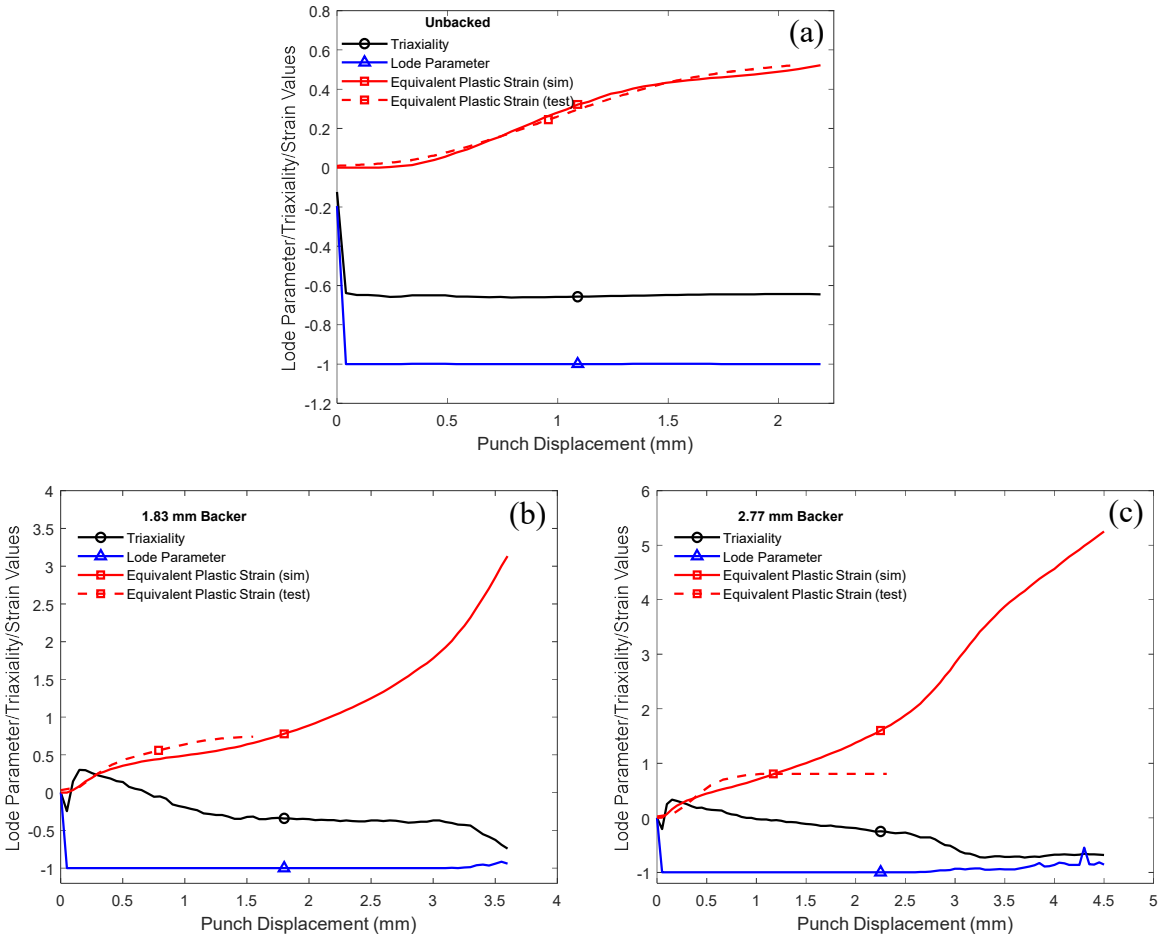

Figure 4.28 Equivalent plastic strain, triaxiality, and Lode parameter at the maximum displacement point for In718 hemispherical backed punch tests for (a) unbacked, (b) 1.83 mm, and (c) 2.77 mm thick backing plates

In Figure 4.25(a), it can be seen that the simulated and experimental equivalent plastic strains for the Al2024 unbacked hemispherical punch test align well with one another. The simulated triaxiality and Lode parameter remain relatively constant throughout the experiment at values of approximately $\sigma^* = -\frac{2}{3}$ and $L = -1$, respectively. This means that the material remains in a constant state of in-plane, equi-biaxial tension as it is loaded to fracture. Figure 4.25(b) and (c) show that the equivalent plastic strain does not show as strong of an agreement between the simulated and experimental values for the Al2024 hemispherical punch tests when a backing plate

is added. This is not surprising, given the difficulties previously noted in obtaining high quality DIC data in the backed test measurements.

While the Lode parameter in Figure 4.25(b) and (c) remains relatively constant, the addition of a backing plate causes more variability in the triaxiality as these tests progress. The triaxiality rises to an initial peak of around $\sigma^* = 0$ when a 1.27 mm backing plate is used (Figure 4.25(b)), before decreasing to and settling at an approximate value of $\sigma^* = -0.4$. A similar trend occurs when a 2.54 mm backing plate is used, except that the triaxiality rises to an initial peak of approximately $\sigma^* = 0.2$ and remains there for a time before decreasing and settling at a value of approximately $\sigma^* = -0.1$. This increase in the triaxiality with the addition of a backing plate is due to the out-of-plane compression that the backing plate induces on the specimen. The higher the relative amount of out-of-plane compression stress compared to the in-plane tension stresses induced by the punch, the larger (more positive) the triaxiality becomes. This is clearly seen in the fact that the test with the thicker 2.54 mm backing plate has a more positive (i.e., more compressive) triaxiality than the test with the thinner 1.27 mm thick backing plate. The triaxiality in Figure 4.25(c) with a 2.54 mm thick backing plate increases to the point that it becomes positive for a large portion of the test. This positive triaxiality indicates that the stress state is compression dominated during that portion of the experiment.

It can also be seen in Figure 4.25 that just as the triaxiality increases with the addition of more out-of-plane compression, so too does the equivalent plastic strain at fracture, $\bar{\varepsilon}_f^p$. The final value of the simulated equivalent plastic strain (corresponding to the same punch displacement and load when fracture is observed in the experiments) is taken to be the equivalent plastic strain at fracture. For the Al2024 hemispherical punch tests, the equivalent plastic fracture strain for the unbacked test is approximately $\bar{\varepsilon}_f^p = 0.44$, increases to approximately $\bar{\varepsilon}_f^p = 0.64$ in the 1.27 mm

backed tests, and further increases to approximately $\bar{\varepsilon}_f^p = 1.12$ when a 2.54 mm thick backing plate is used.

The Al2024 elliptical punch tests shown in Figure 4.26 show the same phenomenon of increasing equivalent plastic fracture strain with increasing backer plate thickness (i.e., increasing out-of-plane compression). Also, because higher quality DIC data is obtained in these backed experiments, the experimental and simulated equivalent plastic strain align well. The equivalent plastic fracture strain increases from a value of approximately $\bar{\varepsilon}_f^p = 0.20$ in the unbacked test to a value of approximately $\bar{\varepsilon}_f^p = 0.62$ when a 3.175 mm thick backing plate is used. The triaxiality in the Al2024 elliptical punch tests also shows similar behavior to the Al2024 hemispherical punch tests. The triaxiality remains at a constant value of approximately $\sigma^* = -\frac{2}{3}$ in Figure 4.26(a) for the unbacked test, when there is solely in-plane tension stress. When a backing plate is used, as in Figure 4.26(b-d), the triaxiality rises to an initial peak value before slowly decreasing and settling to a lower value. The thicker the backing plate and consequently the higher the amount of out-of-plane compression, the larger (more positive) the triaxiality becomes, even rising above zero to a compression dominated state of stress in the tests with 2.36 mm and 3.175 mm thick backing plates.

The behavior of the Lode parameter in the Al2024 elliptical punch tests, shown in Figure 4.26, shows a stark difference to that of the hemispherical punch tests shown in Figure 4.25. When a hemispherical punch is used, the symmetric shape of the punch induces equal in-plane tension stresses along any direction. This equi-biaxial in-plane tension results in a very constant Lode parameter of approximately $L = -1$ for all the Al2024 hemispherical backed punch tests. In the elliptical punch tests the 2x6 mm elliptical shaped punch causes asymmetric in-plane tension

stresses, with the tension stress along the major punch diameter being greater than the stress in the direction of the minor diameter. In Figure 4.26 it can be seen that initially during the tests the Lode parameter starts at a value near $L = -1$, then steadily increases as the test progresses. This indicates that in the initial stage of each test the material does experience a stress state of equi-biaxial in-plane tension where $L = -1$. This is likely due to the fact that initially only a very small portion of the punch tip is in contact with the specimen. This initial contact can be approximated as similar to a point contact, where the relative difference between the major and minor punch diameters is not yet relevant to the stresses induced in the specimen.

As the punch advances further into the specimen, a larger area of the punch comes into contact with the specimen. As the specimen bulges outward and begins to deform around the elliptical punch, the effect of the punch asymmetry becomes more profound. It begins to induce different relative amounts of tension aligned with the major and minor axes of the elliptical punch. This causes the Lode parameter to increase and deviate from the $L = -1$ meridian.

The Lode parameter is affected by the backing plate thickness during the elliptical punch tests, a phenomenon which is not observed in the hemispherical punch tests. As shown in Figure 4.25 for the Al2024 hemispherical punch tests, so long as equi-biaxial in-plane tension is maintained, the Lode parameter remains at $L = -1$ regardless of the amount of out-of-plane compression added. In the elliptical punch tests, because the in-plane tension stresses are no longer equal, the stress state is affected by the ratio of the tension stresses to one another, as well as by the ratio of each tension stress to the out-of-plane compression stress. For the unbacked elliptical punch test in Figure 4.26(a), the Lode parameter remains at $L = -1$ until approximately 0.2 mm of punch displacement, or until shortly after plastic deformation is induced in the specimen (as

evidenced by the equivalent plastic strain becoming non-zero). The Lode parameter then steadily rises to a peak value of approximately $L = -0.4$ with some minor oscillations.

When a backing plate is added the Lode parameter becomes more oscillatory throughout the test, as shown in Figure 4.26(b-d). A more complex material response under these conditions is not surprising, given that the stress state with a backing plate is now three dimensional. The Lode parameter in the unbacked test is reliant solely upon the ratio of the in-plane tension stresses to one another. With a backing plate, the Lode parameter value is dependent on the in-plane tension stresses and the out-of-plane compression stress. Changes in the relative magnitudes of these three stresses during the backed tests cause these variations in the value of the Lode parameter. Increasing the backer plate thickness also tends to cause an increase in the peak value of the Lode parameter, with the Lode parameter rising to a peak value of approximately $L = 0$ with 1.575 and 2.36 mm thick backing plates, and rising to a peak value of approximately $L = 0.2$ with a 3.175 mm thick backing plate.

The Ti64 hemispherical punch test results shown in Figure 4.27 show a similar overall behavior as the Al2024 hemispherical punch tests shown in Figure 4.25. The equivalent plastic strain values determined from DIC measurements and from the simulations generally agree with one another. This is particularly true for the unbacked Ti64 hemispherical punch test in Figure 4.27(a). For the backed tests, the deviation between the experimental and simulated equivalent plastic strain values is likely due to the inherent difficulties of obtaining high quality DIC measurements when a backing plate is used. The experiments show the same phenomenon previously noted for Al2024 of increasing triaxiality and equivalent plastic strain at fracture with increasing backer plate thickness (i.e., increasing out-of-plane compression).

The Ti64 unbacked tests in Figure 4.27(a) has triaxiality that remains constant at approximately $\sigma^* = -\frac{2}{3}$, and an equivalent plastic fracture strain of approximately $\bar{\varepsilon}_f^p = 0.36$. In Figure 4.27(b), the tests with 0.889 mm thick backing plates exhibited a triaxiality that increases to an initial peak of approximately $\sigma^* = -0.1$ before steadily decreasing to approximately $\sigma^* = -0.5$. This increase in triaxiality is accompanied by an increase in the equivalent plastic fracture strain to a value of approximately $\bar{\varepsilon}_f^p = 0.47$. Interestingly, the 1.27 mm thick backed test in Figure 4.27(c) exhibits a further increase in triaxiality (an initial peak of approximately $\sigma^* = 0.2$, before steadily decreasing to approximately $\sigma^* = -0.5$), yet the equivalent plastic fracture strain remains at a very similar value to that of the 0.889 mm thick backing plate tests, again approximately $\bar{\varepsilon}_f^p = 0.47$. When the backing plate thickness is further increased to 1.83 mm thick, as shown in Figure 4.27(d), the triaxiality and equivalent plastic fracture strain both increase. The triaxiality increases to an initial peak value of approximately $\sigma^* = 0.45$, and while it then decreases, it remains above zero (in the compression dominated stress state regime) for almost half of the remaining experiment before settling at a value of approximately $\sigma^* = -0.35$. The equivalent plastic fracture strain increases from the other Ti64 backed punch tests to a value of approximately $\bar{\varepsilon}_f^p = 0.56$.

The In718 hemispherical punch test results shown in Figure 4.28 reflect similar trends to those seen in Figure 4.25 and Figure 4.27 for the Al2024 and Ti64 hemispherical punch tests. The unbacked punch test in Figure 4.28(a) shows good agreement between the simulated and experimentally determined equivalent plastic strain. The equivalent plastic fracture strain is determined to be $\bar{\varepsilon}_f^p = 0.56$. The simulated triaxiality and Lode parameter remain relatively constant throughout the experiment at values of approximately $\sigma^* = -\frac{2}{3}$ and $L = -1$.

The In718 backed punch test results in Figure 4.28(b) and (c) show initial agreement between the experimental and simulated equivalent plastic strain, before the DIC data drops out and the experimental value becomes unavailable. The simulations are ran until the last point before fracture is observed in the continuous tests (punch displacement of 3.55 mm with a 1.83 mm thick backing plate, and punch displacement of 4.49 mm with a 2.77 mm thick backing plate). At that point the simulated equivalent plastic strain is extremely high for both the In718 backed experiments, having a value of $\bar{\varepsilon}_f^p = 3.13$ for the 1.83 mm backed tests and $\bar{\varepsilon}_f^p = 5.25$ for the 2.77 mm backed tests.

Recall that the LS-DYNA simulations of the In718 backed punch tests are unable to accurately capture the physical material behavior all the way up to these final points before observed fracture, due to the element thinning and distortion shown in Figure 4.19 and Figure 4.20. Consequently, the above values of equivalent plastic fracture strain are almost certainly incorrect, as they include simulation data from after the element distortion occurs. This occurs at a punch displacement of 3.2 mm for the 1.83 mm backed punch test and at a punch displacement of 2.75 mm for the 2.77 mm backed punch test. Truncating the simulation data at this point can be used to find a lower limit on the equivalent plastic fracture strain under these stress states. This yields lower limit equivalent plastic fracture strains of $\bar{\varepsilon}_f^p = 2.21$ for the In718 1.83 mm backed punch tests, and $\bar{\varepsilon}_f^p = 2.28$ for the In718 2.77 mm backed punch tests.

The element distortion can also be seen in the behavior of the simulated stress state parameters in Figure 4.28(b) and (c). At the same moment that the elements become so thin that they can no longer conform to the punch shape, the triaxiality abruptly decreases and the Lode parameter begins to rise away from the $L = -1$ meridian. It is highly unlikely that this behavior

accurately reflects the stress state that occurs in the actual physical experiments, given the non-physical behavior of the simulation elements at this point. Hence the stress state parameters are only valid up until the point that element distortion occurs, and the values reported after that point should be ignored. If this is done, a similar trend is observed for the In718 hemispherical punch test as is seen for the Al2024 and Ti64 hemispherical punch tests. The Lode parameter in Figure 4.28(b) and (c) remains nearly constant at a value of $L = -1$, indicating equi-biaxial in-plane tension. The triaxiality increases to an initial peak value of approximately $\sigma^* = 0.3$ before decreasing and setting at a value of approximately $\sigma^* = -0.3$ in the In718 1.83 mm backed punch tests. In the In718 2.77 mm backed punch tests, the triaxiality increases to an initial peak value of approximately $\sigma^* = 0.33$ before steadily decreasing to a final value of $\sigma^* = -0.36$ before element distortion begins to occur. In addition, for the In718 2.77 mm backed punch tests the triaxiality decreases more slowly than for the 1.83 mm backed punch tests, meaning the 2.77 mm backed punch tests remain longer in a compressively dominated stress state.

As noted, many of the above experiments in Figure 4.25 - Figure 4.28 experience variations in the stress state over the progression of the test. While the Lode parameter in the hemispherical backed punch tests remains relatively constant, the triaxiality in all the experiments as well as the Lode parameter in the Al2024 elliptical backed punch tests all vary during the experiments. This is likely due to the changing geometry that occurs during the tests. This changes the way loads are applied to the specimen at the fracture location and causes the stress state to vary during the experiment.

While ideally the stress state parameters should not change during the loading, in reality such variations in the stress state are common in experiments with ductile materials where there are large deformations and geometric changes. Therefore it is necessary to analyze these varying

triaxiality and Lode parameter values in order to construct a stress-state dependent material fracture model. One approach is to attempt to match how the damage accumulates through each stress state that occurs in the simulation, such that the total damage accumulation results in fracture occurring at the same moment in the simulation as is observed in the test. Another simpler approach is to take the average value of each stress state parameter, and use these average values to determine where the corresponding value of equivalent plastic fracture strain should be located on the fracture surface. While using an average value of the triaxiality and Lode parameter simplifies the analysis, it may or may not result in a fracture criterion that accurately models the physical material behavior, depending on the amount of variability that occurs and the general material behavior,

Average values of the Lode parameter and triaxiality with respect to the equivalent plastic strain are calculated by Equations 4-3 and 4-4:

$$\sigma^*_{avg} = \frac{1}{\bar{\varepsilon}^p_f} \int_0^{\bar{\varepsilon}^p_f} \sigma^* \; d\bar{\varepsilon}^p, \tag{4-3}$$

$$L_{avg} = \frac{1}{\bar{\varepsilon}^p_f} \int_0^{\bar{\varepsilon}^p_f} L \; d\bar{\varepsilon}^p. \tag{4-4}$$

The average Lode parameter and average triaxiality are calculated for each of the Al2024, Ti64, and In718 punch tests and are reported in Table 4.1 - Table 4.4. In addition, the corresponding equivalent plastic fracture strain, the punch displacement and the load at which fracture are observed for each test are also summarized. Note that for the In718 backed punch tests, the reported values are those taken by truncating the simulations before the element distortions and non-physical results occur. Therefore the In718 backed punch test values of the equivalent plastic fracture strain should be taken as the lower limit of the fracture strain at this stress state, below which fracture should not occur.

Table 4.1 Al2024 hemispherical punch tests average stress state parameters and fracture strain

	L_{avg}	σ^*_{avg}	$\bar{\varepsilon}^p_f$	Displacement at fracture (mm)	Load at fracture (N)
Unbacked	-0.94	-0.63	0.44	2.14	1,399
1.27 mm Backer	-0.96	-0.25	0.64	2.45	1,463
2.54 mm Backer	-0.97	0.00	1.12	2.15	2,384

Table 4.2 Al2024 elliptical punch tests average stress state parameters and fracture strain

	L_{avg}	σ^*_{avg}	$\bar{\varepsilon}^p_f$	Displacement at fracture (mm)	Load at fracture (N)
Unbacked	-0.71	-0.62	0.20	1.16	1,682
1.575 mm Backer	-0.46	-0.46	0.35	1.66	3,043
2.36 mm Backer	-0.39	-0.30	0.40	1.65	4,000
3.575 mm Backer	-0.28	-0.16	0.62	2.27	5,969

Table 4.3 Ti64 hemispherical punch tests average stress state parameters and fracture strain

	L_{avg}	σ^*_{avg}	$\bar{\varepsilon}^p_f$	Displacement at fracture (mm)	Load at fracture (N)
Unbacked	-0.95	-0.63	0.36	1.30	1,023
0.889 mm Backer	-0.98	-0.25	0.47	1.74	2,615
1.27 mm Backer	-0.98	-0.01	0.47	1.69	3,185
1.83 mm Backer	-0.97	0.20	0.56	1.40	3,944

Table 4.4 In718 hemispherical punch tests average stress state parameters and fracture strain

	L_{avg}	σ^*_{avg}	$\bar{\varepsilon}^p_f$	Displacement at fracture (mm)	Load at fracture (N)
Unbacked	-0.99	-0.65	0.49	2.14	2,621
1.83 mm Backer[†]	-0.95	-0.23	>2.21	3.2	7,787
2.77 mm Backer[†]	-0.96	-0.08	>2.28	2.75	11,178

The average Lode parameter is approximately $L_{avg} = -1$ for each of the Al2024, Ti64, and In718 hemispherical backed punch tests (indicating equi-biaxial in-plane tension). However in the Al2024 elliptical punch tests, the average Lode parameter for the Al2024 elliptical punch

[†] These values correspond to the final simulation values before the elements become highly distorted and the simulation results become non-physical. The reported strain values can be taken as the lower limit on the fracture strain at these stress states.

tests ranges from $L_{avg} = -0.71$ in the unbacked test and increases with increasing backer plate thickness to $L_{avg} = -0.28$ with a 3.175 mm thick backing plate. For the unbacked, hemispherical punch tests where the stress state consists solely of equi-biaxial in-plane tension (no out-of-plane compression), the triaxiality is expected to have a value of $\sigma^*_{avg} = -\frac{2}{3}$. Although the reported unbacked test values in Table 4.1, Table 4.3, and Table 4.4 are not exactly equal to this value, they are certainly a close approximation of it. In the Al2024 elliptical punch tests where there is an unequal amount of tension along the in-plane axes, the triaxiality is expected to fall somewhere between the range of $\sigma^*_{avg} = -\frac{2}{3}$ (equi-biaxial tension) and $\sigma^*_{avg} = -\frac{1}{3}$ (uniaxial tension). A value of $\sigma^*_{avg} = -0.62$ would indicate that the in-plane tension stress along the major punch diameter axis is approximately 1.6 times that of the in-plane tension stress along the minor punch diameter axis. However this is the average ratio for the entire test duration. Figure 4.22 shows that the in-plane tension strains (ε_1 and ε_2) are identical at the beginning of each test and deviate until reaching a ratio of $\frac{\varepsilon_1}{\varepsilon_2} \approx 3$. This indicates the ratio of in-plane tension stresses also varies during loading, and does not stay constant at the average value.

Each test set above shows an increase in σ^*_{avg} with increasing backing plate thickness (increasing out-of-plane compression). The Al2024 hemispherical punch tests and the In718 hemispherical punch tests both achieve a maximum average triaxiality of $\sigma^*_{avg} \approx 0$ in the tests with the thickest backing plates, indicating the tension and compression stresses are relatively similar in magnitude. The Al2024 elliptical punch test with the thickest backing plate exhibits $\sigma^*_{avg} = -0.16$, indicating that the tension stresses are greater in magnitude than the compression stress. The Ti64 hemispherical punch test shows the greatest increase in average triaxiality, to a value of $\sigma^*_{avg} = 0.20$, firmly within the compression dominated stress state regime.

Increasing the amount of out-of-plane compression results in a dramatic increase in the corresponding equivalent plastic fracture strain. The Al2024 hemispherical punch tests, Al2024 elliptical punch tests, and Ti64 hemispherical punch tests each show an increase of 152%, 213%, and 55.5% in the fracture strain, respectively, between the unbacked and thickest backing plate experiments. Because the exact fracture strain could not be determined in the In718 backed punch test experiments, the exact increase in fracture strain between the unbacked and backed experiments cannot be determined. However using the lower limit on the equivalent plastic fracture strain reported in Table 4.4, it can be shown that In718 experiences a greater than 362% increase in fracture strain between the unbacked and thickest backing plate experiments. While it is generally known that compression tends to increase the fracture strain by inhibiting void growth and coalescence, it was not previously known that the fracture strain would increase by the above magnitudes when out-of-plane compression is superimposed on top of in-plane biaxial tension.

4.2 Direct Impact Test Results: Determination of High Strain Rate Plasticity Behavior

Direct impact tests are performed on Al2024, Ti64, and In718 specimens. A sample DIC image from these tests is shown in Figure 4.29. This figure shows the areas on the specimen, transmitter, and projectile over which the average DIC displacement and strain values are calculated. In addition the DIC inspect extensometer is shown, which is used to determine the relative displacement between the projectile and transmitter bar.

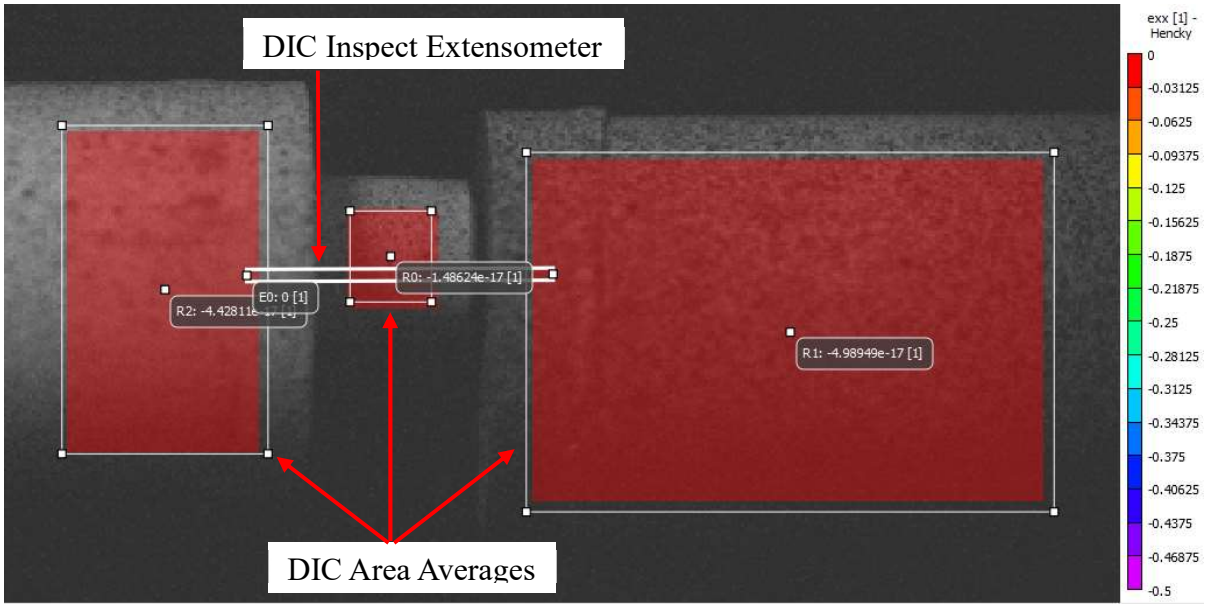

Figure 4.29 DIC image and inspection elements from a direct impact SHB test

Because the images are taken at a rate of either 2,000,000 or 5,000,000 frames per second, the camera has a maximum exposure time between 200 and 500 nanoseconds during which the sensor captures the image. This short exposure time means that a large amount of light is required to sufficiently saturate the sensor in order to create a bright image with suitable contrast for DIC analysis.

Typically, for tests at this frame rate the light source is placed close to the specimen, and often a pre-triggered pulsed light source is used to generate a higher intensity light. However, the impact of the projectile creates a significant amount of shrapnel, meaning light sources cannot be placed close to the specimen without being destroyed. Furthermore, because the test is post-triggered by the strain gage voltage pulse in the transmitter bar, there is no opportunity to send a pre-triggered signal to initiate a pulsed light source during the test. Many high intensity light sources require air and a ventilation fan for cooling, and since these tests are performed in a vacuum such light sources are not feasible.

Six Cree CXA2790 LED lights, placed between 0.5 and 1 m from the specimen to avoid shrapnel damage, are used to illuminate the specimen during the tests. This illumination method resulted in DIC images that are too dark and with insufficient contrast to obtain highly localized strain and displacement data. Therefore, the area averages of the DIC data are determined and used for analysis. In addition the DIC inspect extensometer is used determine the overall change in length of the specimen as it is compressed.

The force between the rear edge of the specimen and the transmitter bar is measured via the voltage output of the strain gages on the transmitter bar, using the previously determined 1780 N/mV conversion factor. Using this conversion factor assumes the transmitter bar does not deform plastically during the test. The Ti64 transmitter bars are 12.7 mm in diameter with an approximate yield strength of 830 MPa. Plastically deforming these bars would require a force of over 105,000 N. The measured force during the tests does not exceed this value before specimen fracture occurs, and therefore it can be concluded that the transmitter bars do not plastically deform during the tests. Once the specimen has been fully compressed, the impact of the projectile directly against the transmitter bar does induce significant plastic deformation in the bar. This occurs well after the specimen has fractured and all relevant test data has been captured.

The measured force is synchronized with the DIC data, and the force vs. specimen displacement (determined from the DIC inspect extensometer) is shown in Figure 4.30.

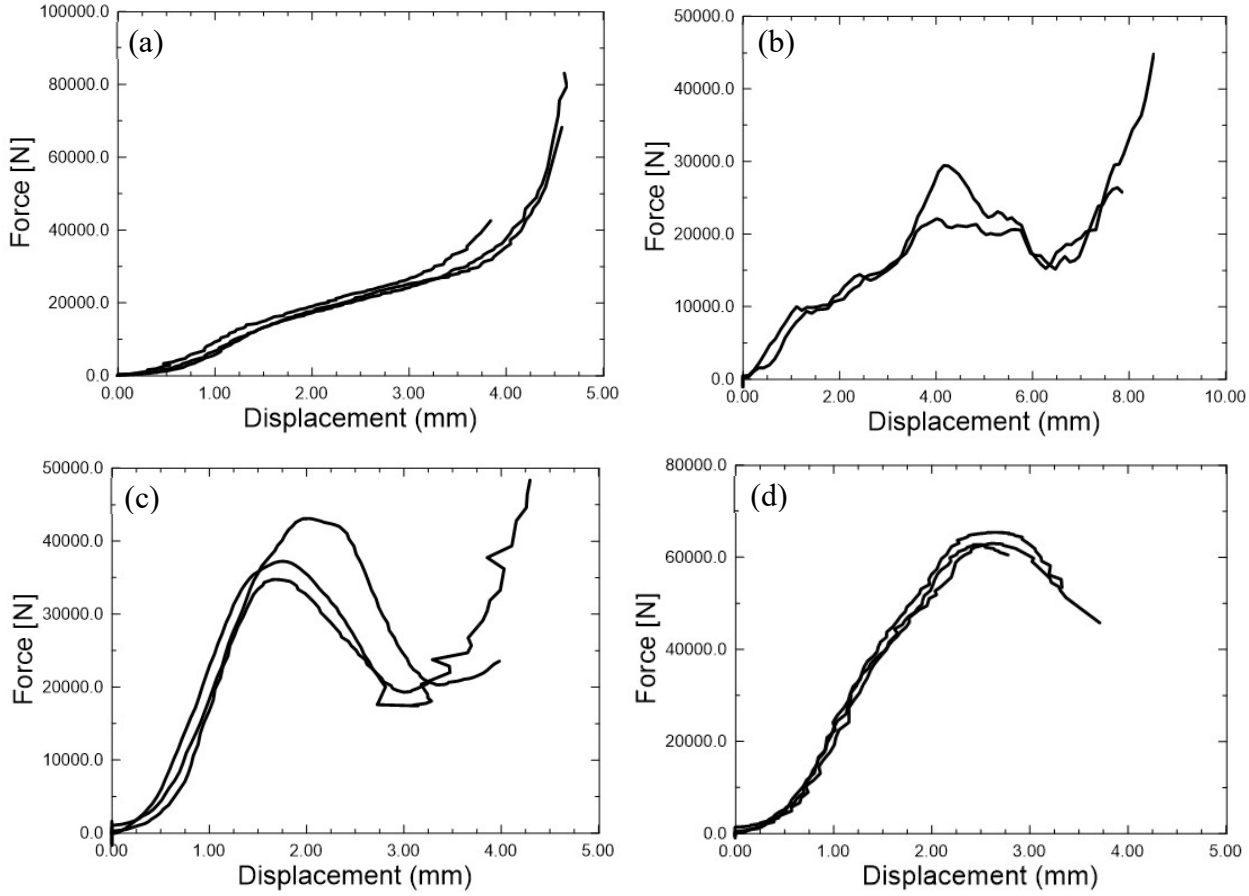

Figure 4.30 Force-displacement curves from direct impact SHB tests on (a) Al2024 5.08 mm long specimens, (b) Al2024 10.16 mm long specimens, (c) Ti64 5.08 mm long specimens and (d) In718 5.08 mm long specimens

The engineering stress can be found by dividing the measured force by the original cross sectional area of the specimen. The engineering strain can be found by dividing the extensometer change in length by the original specimen length. Both of these operations assumes uniform deformation of the specimen and force balance across the specimen length. The engineering stress and strain can then be converted into true stress and strain values using Equations 3-1 and 3-2. The stress vs strain curves found using this analysis are shown in Figure 4.31.

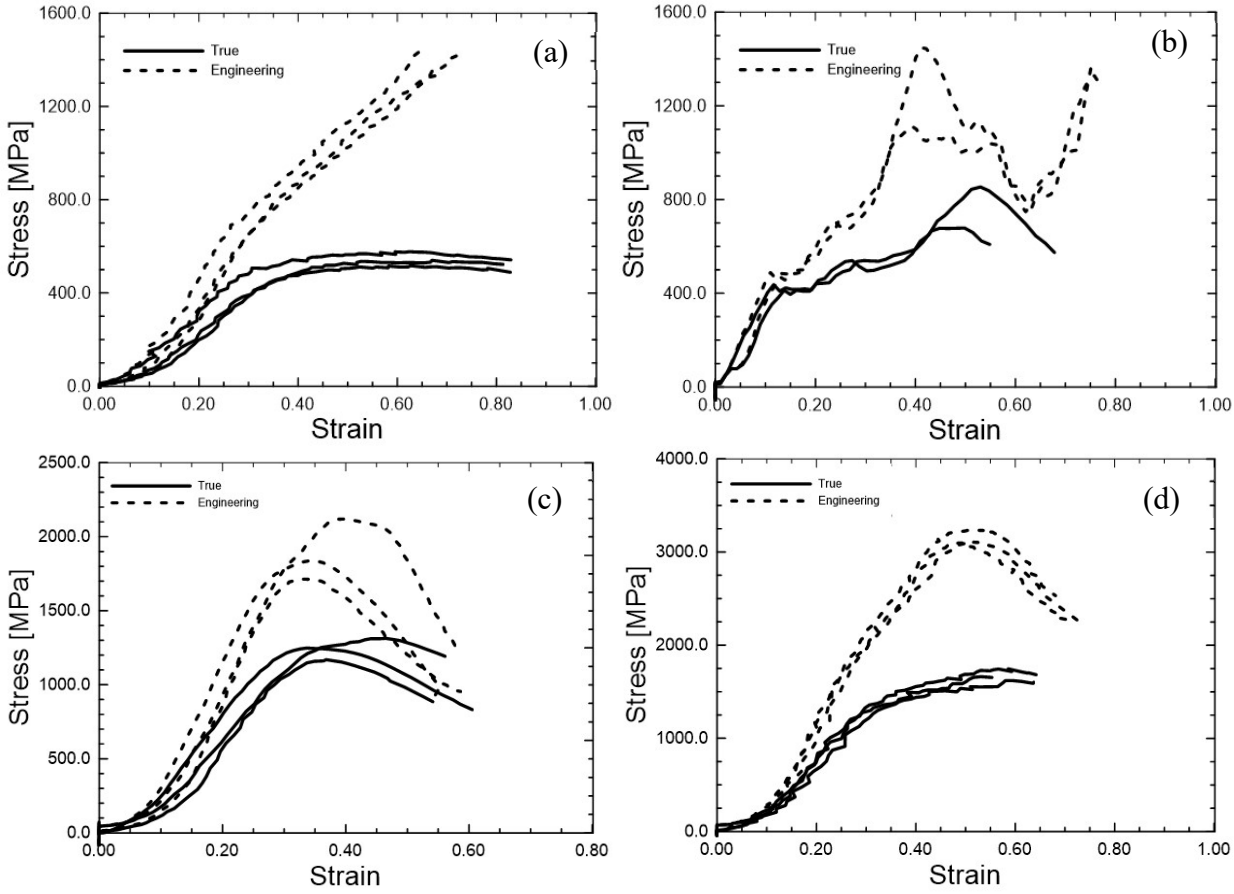

Figure 4.31 Stress-strain curves from direct impact SHB tests on (a) Al2024 5.08 mm long specimens, (b) Al2024 10.16 mm long specimens, (c) Ti64 5.08 mm long specimens and (d) In718 5.08 mm long specimens

These derived stress vs. strain curves are almost certainly incorrect, as the analysis assumes uniform deformation and force balance. In reality neither of these assumptions are likely to be true during the direct impact tests. The DIC images show clear non-uniform specimen deformation, as the impact edge experiences greater plastic deformation and has greater radial expansion than the rear edge. Furthermore, according to elastic wave theory, the rear edge of the specimen will not experience a compressive force until the elastic compression stress wave generated by the impact travels the entire length of the specimen and reaches the rear edge. At this moment part of the elastic wave continues into the transmitter bar, while a portion of the elastic wave reflects back into the specimen and begins traveling in the opposite direction. The elastic wave must typically

travel along the specimen length and reflect off both ends several times before force balance is achieved between the ends of the specimen. The speed of the elastic wave for a given material is defined by $c = \sqrt{\frac{E}{\rho}}$, where c is the elastic wave speed, E is the Young's modulus and ρ is the material density. These material constants and the elastic wave speed for each of the materials are summarized in Table 4.5 below.

Table 4.5 Elastic modulus, density, and elastic wave speed of each tested material

	E [GPa]	ρ [kg/m^3]	c [mm/μs]
Al2024	70	2600	5.188
Ti64	110	4430	4.983
In718	210	8190	5.063

The wave speed for each material is approximately 5 mm/μs, meaning it will take roughly 1 μs for the elastic wave to travel the full length of a 5.08 mm long specimen and roughly 2 μs to travel the length of a 10.16 mm long specimen. DIC images are taken every 0.2 μs for tests with 5.08 mm long specimens, meaning there will be 5 DIC images taken between the time the projectile impacts the specimen and the elastic wave reached the rear edge of the specimen. DIC images taken every 0.5 μs for tests with 10.16 mm long specimens, meaning those tests will have 4 DIC images between the projectile impact and when the elastic wave reaches the rear edge of the specimen. DIC images from this time frame are show in Figure 4.32 - Figure 4.35.

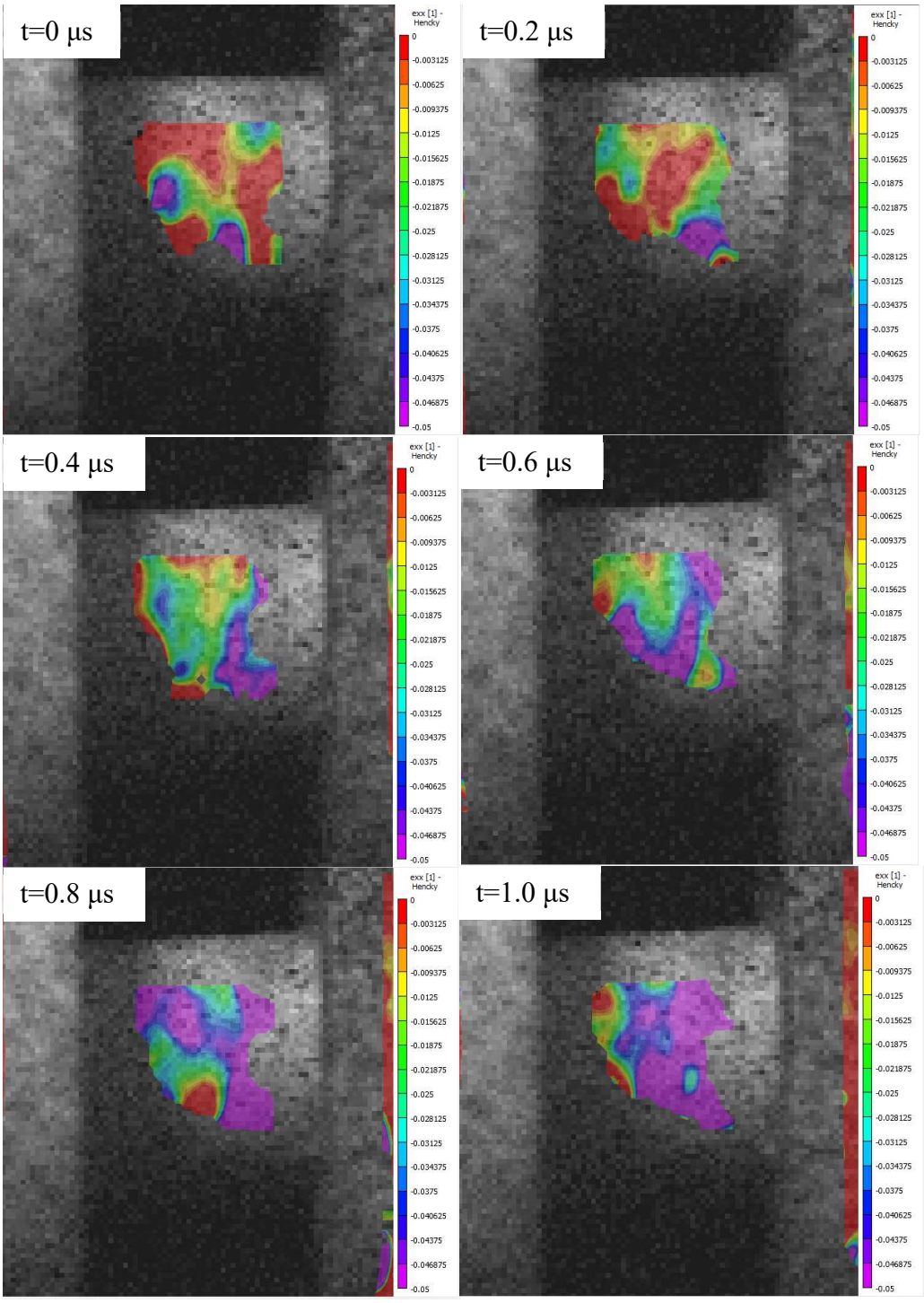

Figure 4.32 Initial frames of Al2024, 5.08 mm long specimen during a direct impact SHB test showing DIC compressive strains occurring due to impact before the elastic wave has traveled the entire specimen length

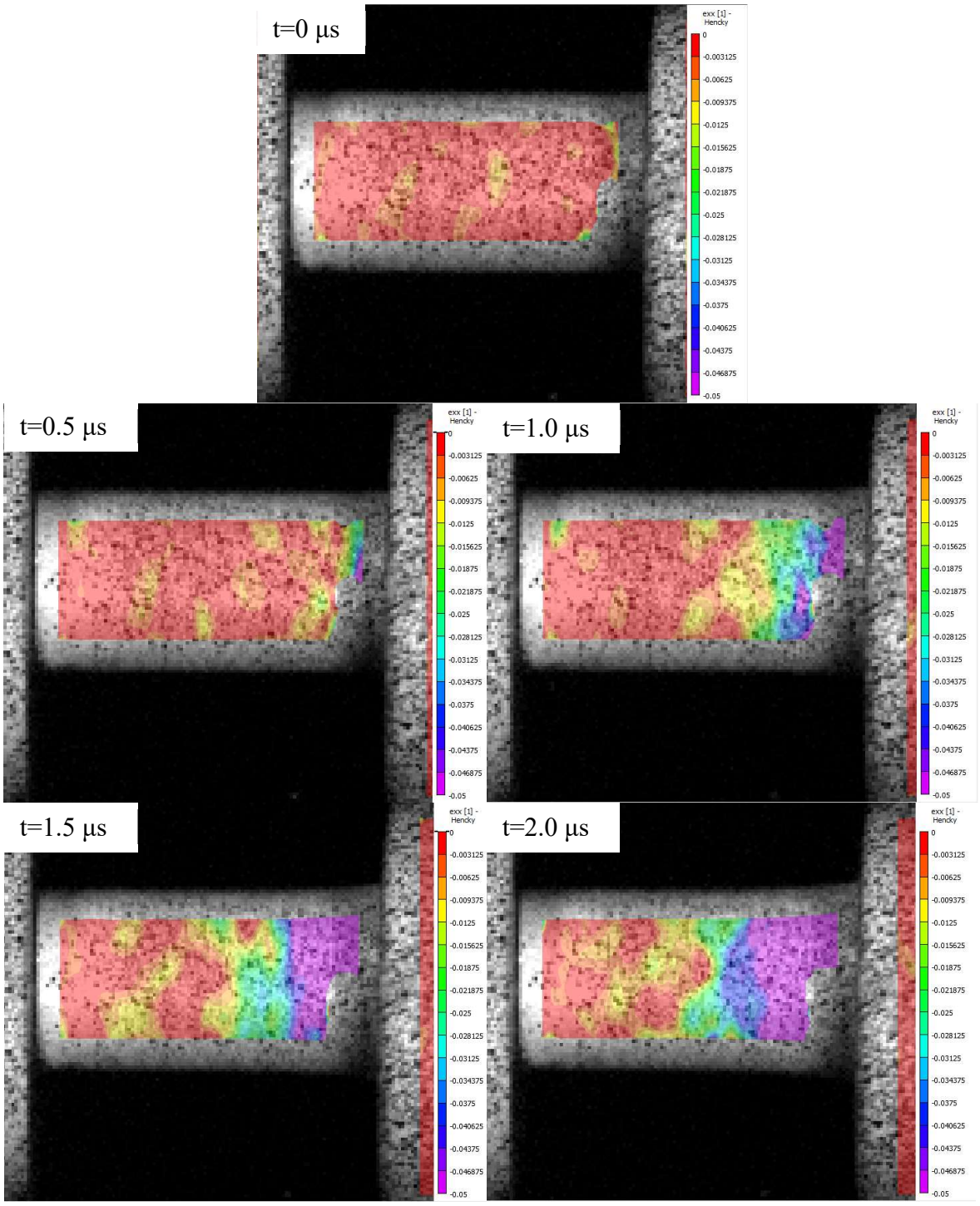

Figure 4.33 Initial frames of Al2024, 10.16 mm long specimen during a direct impact SHB test showing DIC compressive strains occurring due to impact before the elastic wave has traveled the entire specimen length

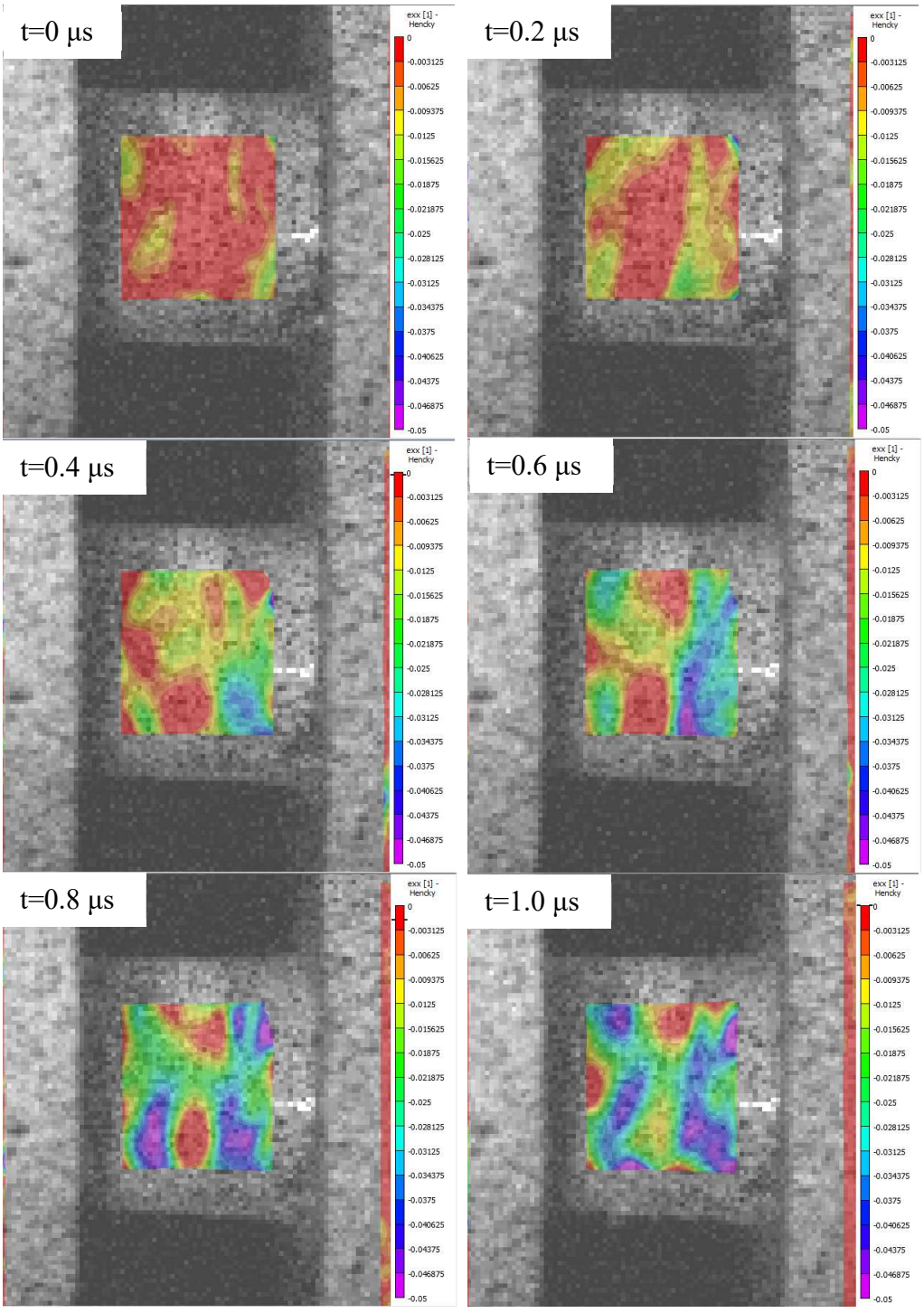

Figure 4.34 Initial frames of Ti64, 5.08 mm long specimen during a direct impact SHB test showing DIC compressive strains occurring due to impact before the elastic wave has traveled the entire specimen length

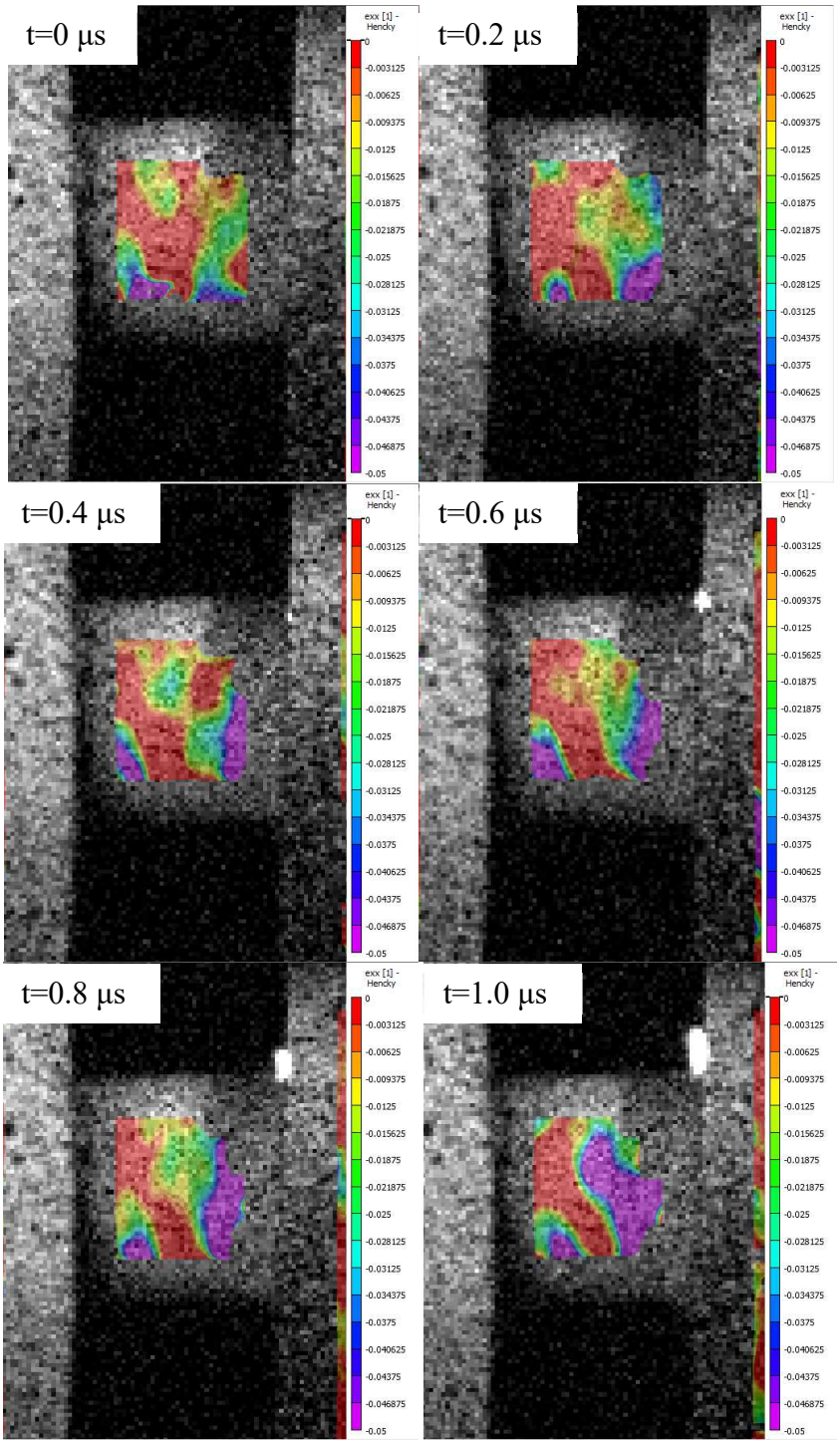

Figure 4.35 Initial frames of In718, 5.08 mm long specimen during a direct impact SHB test showing DIC compressive strains occurring due to impact before the elastic wave has traveled the entire specimen length

As can be seen in Figure 4.32 - Figure 4.35, there is clear deformation and radial displacement at the impact edge during this time frame. Furthermore DIC analysis shows

compressive strains occurring towards the front edge of the specimen. The impact edge is clearly experiencing compressive loading, yet the rear edge of the specimen continues to experience no load until the elastic wave has traveled the full length of the specimen. Therefore, it can be concluded that the specimen is not under force balance during the early part of the test.

Elastic wave theory states that the specimen is not in a state of force balance until several wave reflections within the specimen have occurred, and the majority of the internal elastic wave has been transmitted out of the specimen into the transmitter bar and incident bar/projectile. While the actual number of wave reflections within the specimen before force balance is achieved is unknown, investigations into this behavior by Sutton et. al. [37] on tension split-Hopkinson bar tests indicate that it takes approximately 5-10 reflections before the accelerations within the specimen die down and force balance is achieved.

While a tension split-Hopkinson bar test is different from the direct impact split-Hopkinson tests described here, if we estimate that it requires a minimum of 5-10 wave reflections before force balance is achieved, this would occur after 5-10 μs for the 5.08 mm long specimens and 10-20 μs for the 10.16 mm long specimens. DIC images taken during this time frame are shown in Figure 4.36 - Figure 4.39. These images show significant damage to the specimen after the time required for 10 wave reflections have occurred, with visible cracks in the specimens. This also corresponds to roughly the same time in the tests as the peak loads seen in Fig. 4.30 for the 10.16 mm long Al2024, 5.08 mm long Ti64 and 5.08 mm long In718 specimens, indicating fracture has indeed occurred and caused this decrease in load by that point in the test. Therefore it is seems highly unlikely the specimens experience any significant period of force-equilibrium before fracture occurs in the direct impact experiments.

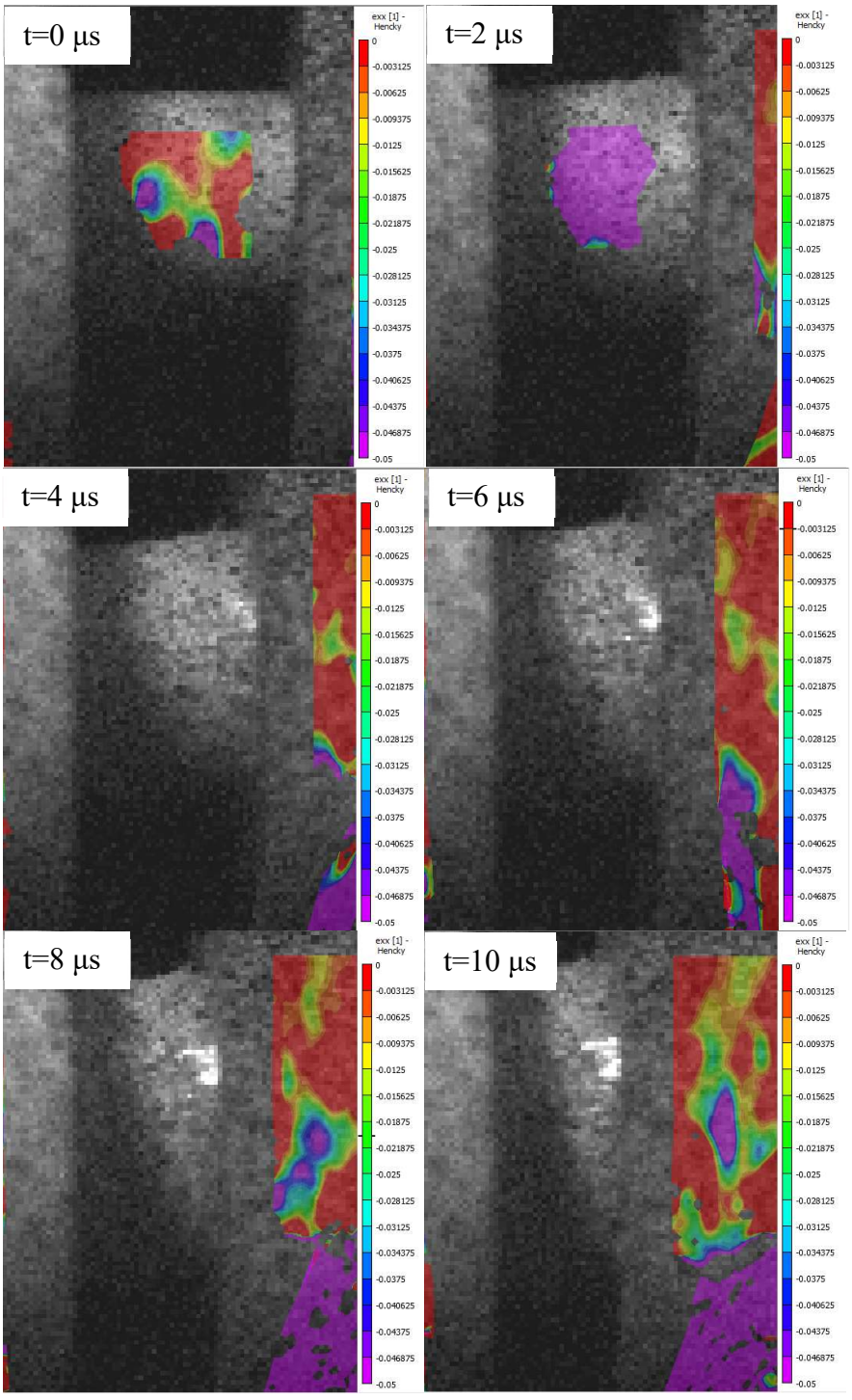

Figure 4.36 First 10 μs of a direct impact SHB test on an Al2024, 5.08 mm long specimen

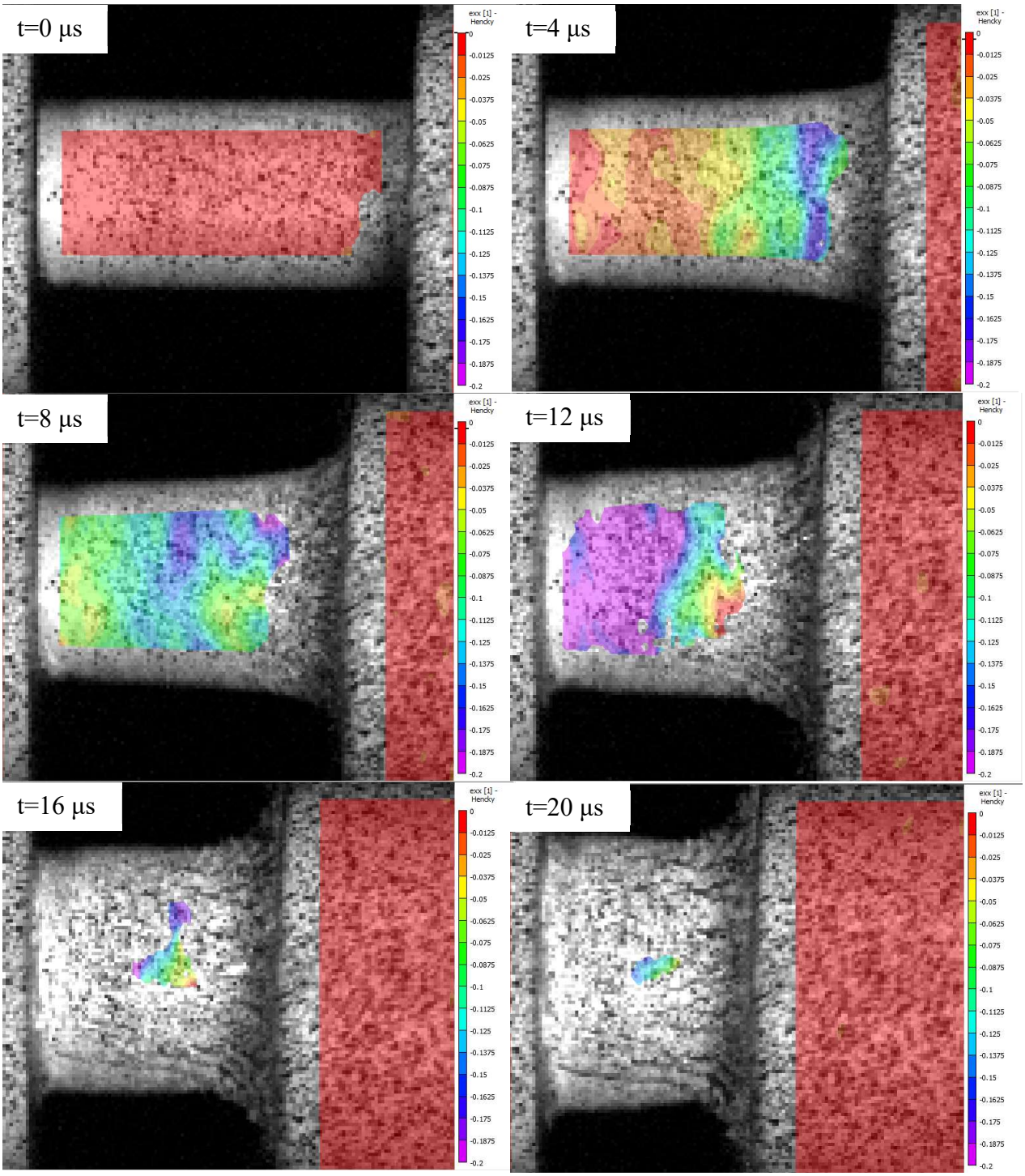

Figure 4.37 First 20 µs of a direct impact SHB test on an Al2024, 10.16 mm long specimen

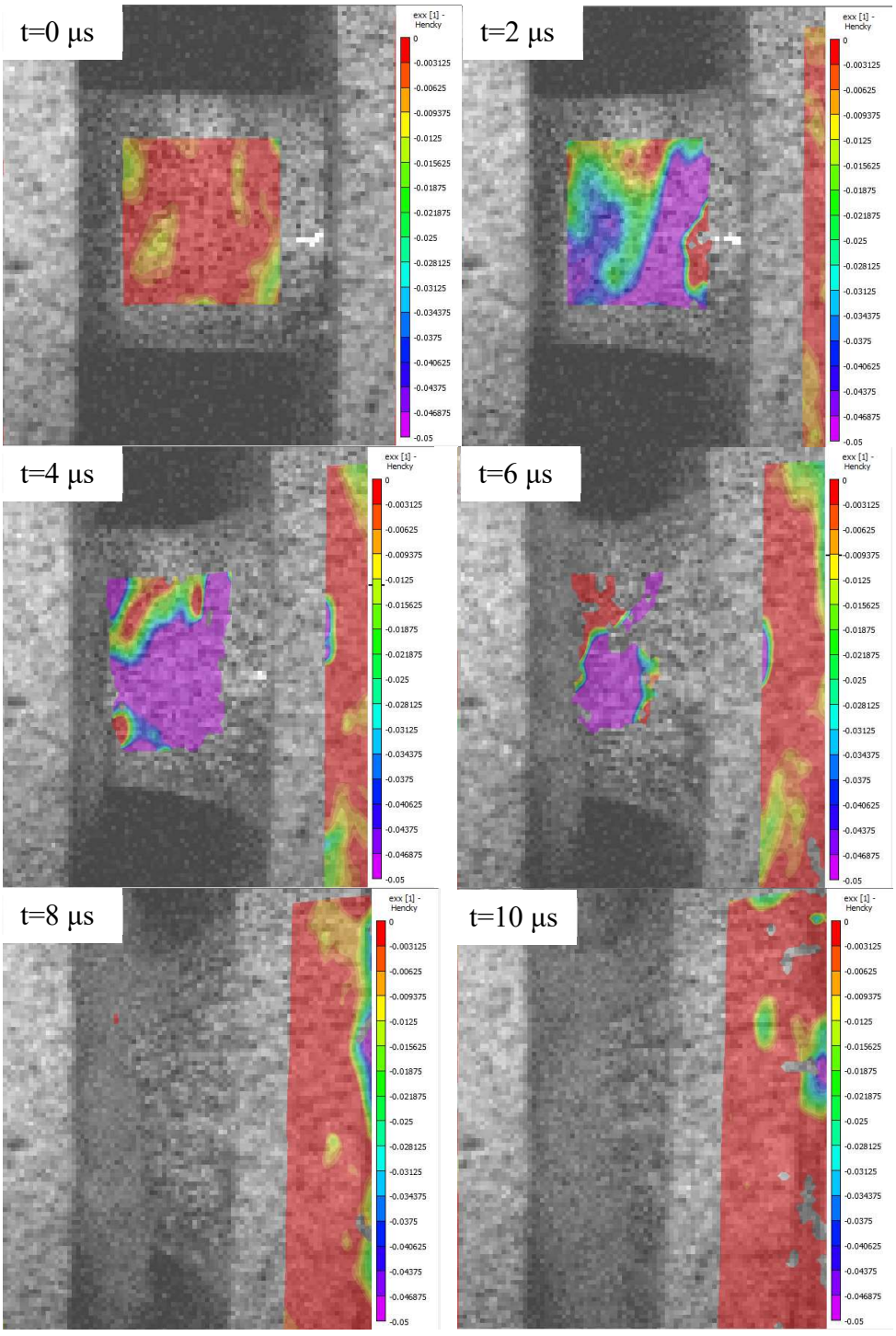

Figure 4.38 First 10 µs of a direct impact SHB test on a Ti64, 5.08 mm long specimen

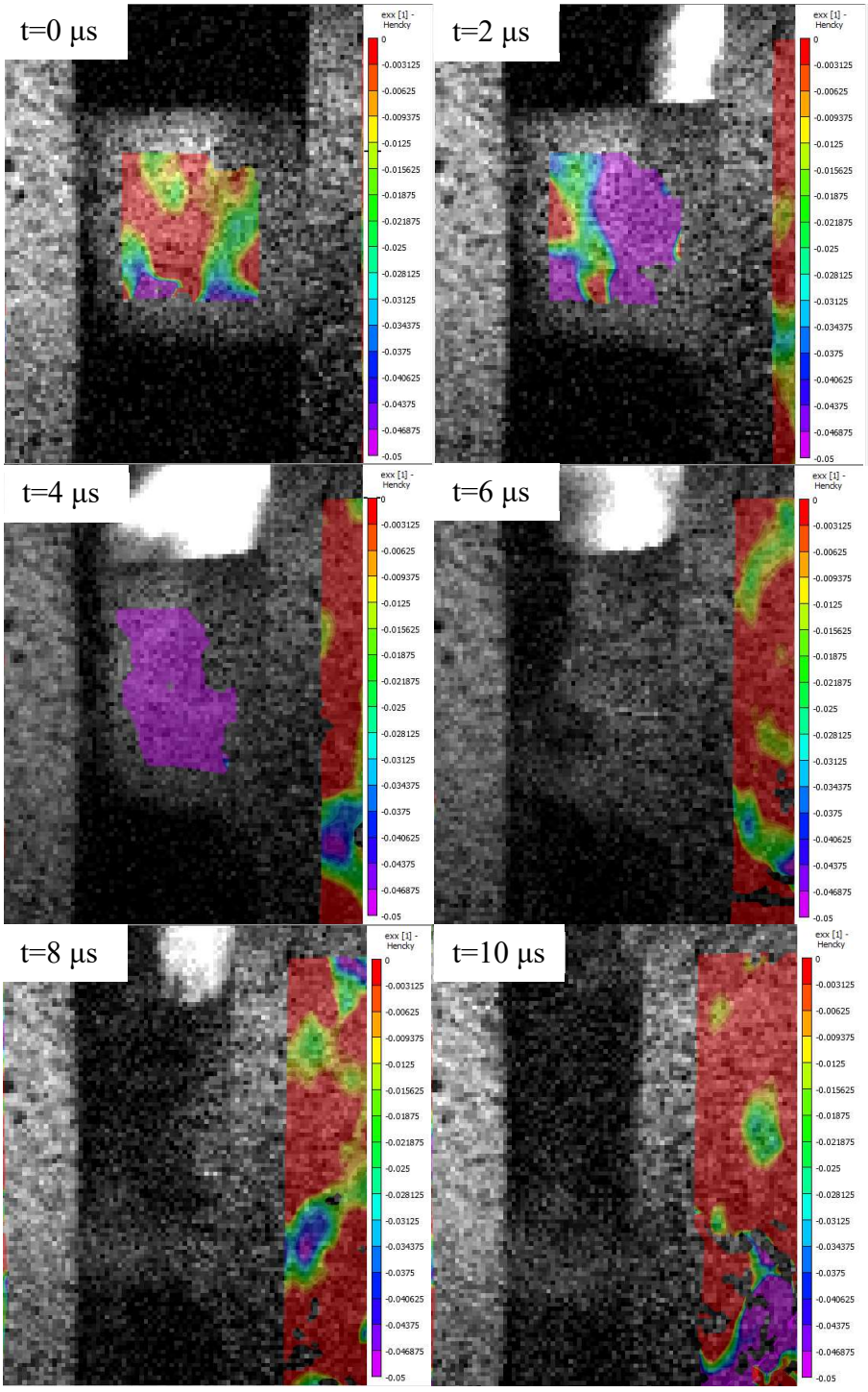

Figure 4.39 First 10 µs of a direct impact SHB test on an In718, 5.08 mm long specimen

Because the specimens undergo non-uniform deformation and do not experience force equilibrium, the underlying assumptions used to calculate the stress versus strain response shown in Figure 4.31 are invalid. In order to determine the response of the materials during this test, a

numerical approach must be used where the material behavior is initially assumed and the tests simulated, and the results between the tests and simulations compared. This comparison is used to update the material model and the process iterated until the simulation and tests agree. While the experimentally determined stress versus strain responses shown in Figure 4.31 are based on invalid assumptions, they can still provide a useful first guess of the material response for the numerical simulations.

From Figure 4.31, it is clear that this test is not capable of capturing the elastic behavior of the materials. This is also evident from the DIC images, which show that the specimens undergo highly localized plastic deformation very early on in the test. Thus, the recorded stress-strain response will be a mixture of the elastic and plastic response. This makes it is impossible to separate out the elastic and plastic responses and directly determine an initial yield point from this data. Another approach is to take the peak true stress from these experiments and compare it to the stress from previous experiments at lower strain rates. The previously determined stress-strain curve can then be scaled appropriately in order to match the same stress level seen in the direct impact experiments.

Most metals that are rate-sensitive exhibit strain rate hardening. It becomes more difficult to induce plastic deformation at higher rates, because it is more difficult for the dislocations in the crystal lattice structure to move past choke points such as grain boundaries in the short time frame during which loading occurs. A higher applied stress becomes necessary at higher strain rates in order to move these dislocations past these choke points and induce plastic deformation. Therefore it would be expected to see an increased level of stress in the direct impact tests compared to tests performed on the same material at lower strain rates.

The peak true stress observed for each material from the 5.08 mm long specimens is 540 MPa for Al2024, 1,220 MPa for Ti64, and 1,630 MPa for In718. The 10.16 mm long Al2024 specimens shows an initial peak true stress of 410 MPa early in the test, followed by a short period of lower, relatively constant stress before the stress begins to rise after approximately 20% true strain. The point where the stress begins to increase again corresponds to approximately 2 mm of projectile displacement at 9 μs after projectile impact. The DIC images show significant plastic deformation and potential cracks in the specimen after this point, indicating the specimen has most likely failed. Therefore, it would be expected that the force after these visible cracks appear would decrease, as is the case for the Ti64 and In718 tests. However this is not the case, and instead the force rises (and likewise the calculated engineering stress rises). Subsequent DIC images after this point show significant radial expansion of the specimen, with the rear edge of the specimen becoming wider than the middle region, even while the impacted edge appears to be nearly obliterated. Therefore it seems plausible that the increase in stress after 9 μs is not indicative of the underlying material behavior, but rather due to geometric effects from using a longer specimen. The longer specimen has more material that becomes trapped between the projectile and transmitter bar even after the specimen has failed, which results in the observed increase in force. Therefore the initial peak stress of 410 MPa is taken as the peak stress for the Al2024 tests using 10.16 mm long specimens.

Each of the above measured peak stresses is lower than the peak stresses observed in previous quasi-static compression tests performed on these same materials [9][10][33]. This indicates that these materials exhibit strain rate softening, which is the opposite of the expected response. This is also contrary to the previous testing that shows that these materials exhibit strain rate hardening at rates between rates of 10^{-4} to 10^{3} s^{-1}, although the effect is slight for Al2024

[9][10][33]. Consequently, it is highly unlikely that a stress-strain curve scaled down to match this stress level would accurately describe the material behavior.

One possible explanation as to why the observed peak stress in the direct impact experiments is lower than that seen in previous experiments would be if the direct impact tests induce a higher thermo-mechanical temperature rise. If the temperature rise is significant enough the thermal softening could offset the effect of strain rate hardening, and result in a lower overall peak stress. Another possible explanation is that the specimen is fracturing prematurely during the experiment, resulting in less undamaged material capable of carrying load. This would cause a decrease in the load and a perceived decrease in the stress, since this reduction in load-bearing area is not taken into account in the above stress calculations.

Another option to estimate the stress-strain response from the experimental data is to scale a previously determined stress-strain curve such that the yield stress will match the observed peak stress from the direct impact experiments. It is expected that such a material model would over-predict the stress levels compared to the experiments. However the addition of thermal softening due to the temperature rise in the experiments would lower the simulated stress levels, potentially to the point where they could agree with the experimental response.

As mentioned in Chapter 3.2, the direct impact tests are simulated in LS-DYNA using *MAT_224 material models constructed by the FAA's Aerospace Working Group (AWG) from previous experimental characterization studies and optimized to match plate impact experiments 141[9][10][11][33][36]. Additional simulations are also performed using material models derived from the direct impact experimental data. The material models are implemented as simplified *MAT_224 models consisting of a single stress-strain curve. A curve scaled to match peak stress-to-peak stress and a curve scaled to match peak stress-to-yield stress from each direct impact SHB

test series are used. Additional simplified *MAT_224 models with a stress-strain curve derived from quasi-static test data and a curve from the AWG *MAT_224 models at the nominal strain rate for each test (derived from extrapolating the strain rate response to match plate impact experiments) are also used for reference. Simulations are performed with and without the effects of thermal softening for each material model. The stress-strain curves used in the simplified *MAT_224 material models for each test are shown in Figure 4.40 below.

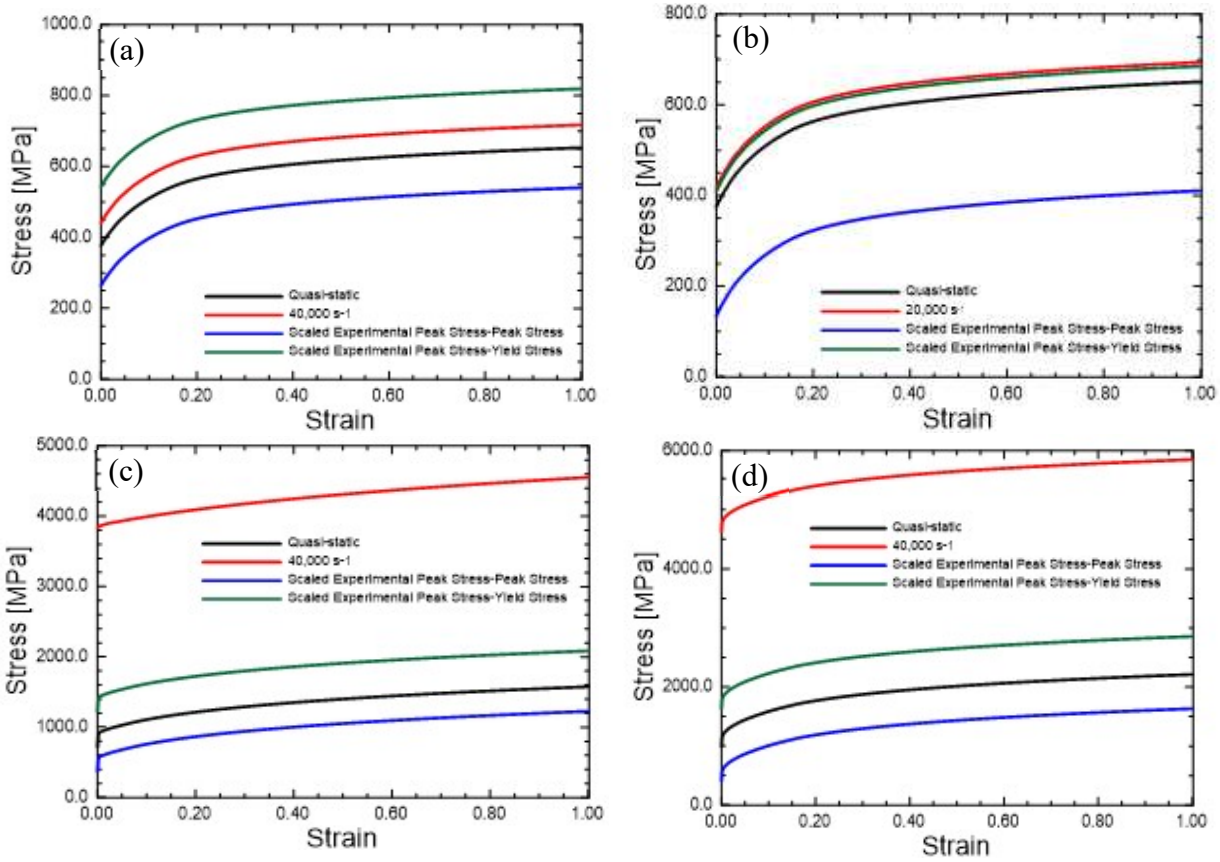

Figure 4.40 Individual stress-strain curves used to construct simplified *MAT_224 material models for simulations of (a) Al2024 5.08 mm long specimens, (b) Al2024 10.16 mm long specimens, (c) Ti64 5.08 mm long specimens, and (d) In718 5.08 mm long specimens

The simulations using each of these material models are compared to the direct impact SHB experimental data. The simulated force is determined through a cross-section of the transmitter bar at the same location as the strain gages in the test. This simulated force values are compared to the measured force from the tests in Figure 4.41 - Figure 4.44.

The mushroomed shape of the specimen contour profile is also compared between the tests and the simulations. The displacement of the nodes on the outer edge of the simulated specimen is recorded and overlaid onto the images from the test at the appropriate scale and time step. This comparison between the experimentally observed and simulated specimen contour profile for each test case is shown in Figure 4.45 - Figure 4.64. In general, these figures show that the inclusion of thermal softening in the simulations has a very minor effect on the simulated force and deformed specimen shape, especially early on in the simulations. At later simulation time steps the material models with thermal effects considered do experience lower loads due to thermal softening, however, this typically occurs at times after fracture has already been observed in the test DIC images.

Overall, the results shown in Figure 4.41 - Figure 4.64 indicate that Al2024 and In718 do not show strain rate hardening at these elevated strain rates, and that Ti64 exhibits a moderate amount of strain rate hardening. While this is in line with previous research results for Al2024, these conclusions are in contrast to previous investigations on Ti64 and In718 that show both these materials exhibit strain rate hardening.

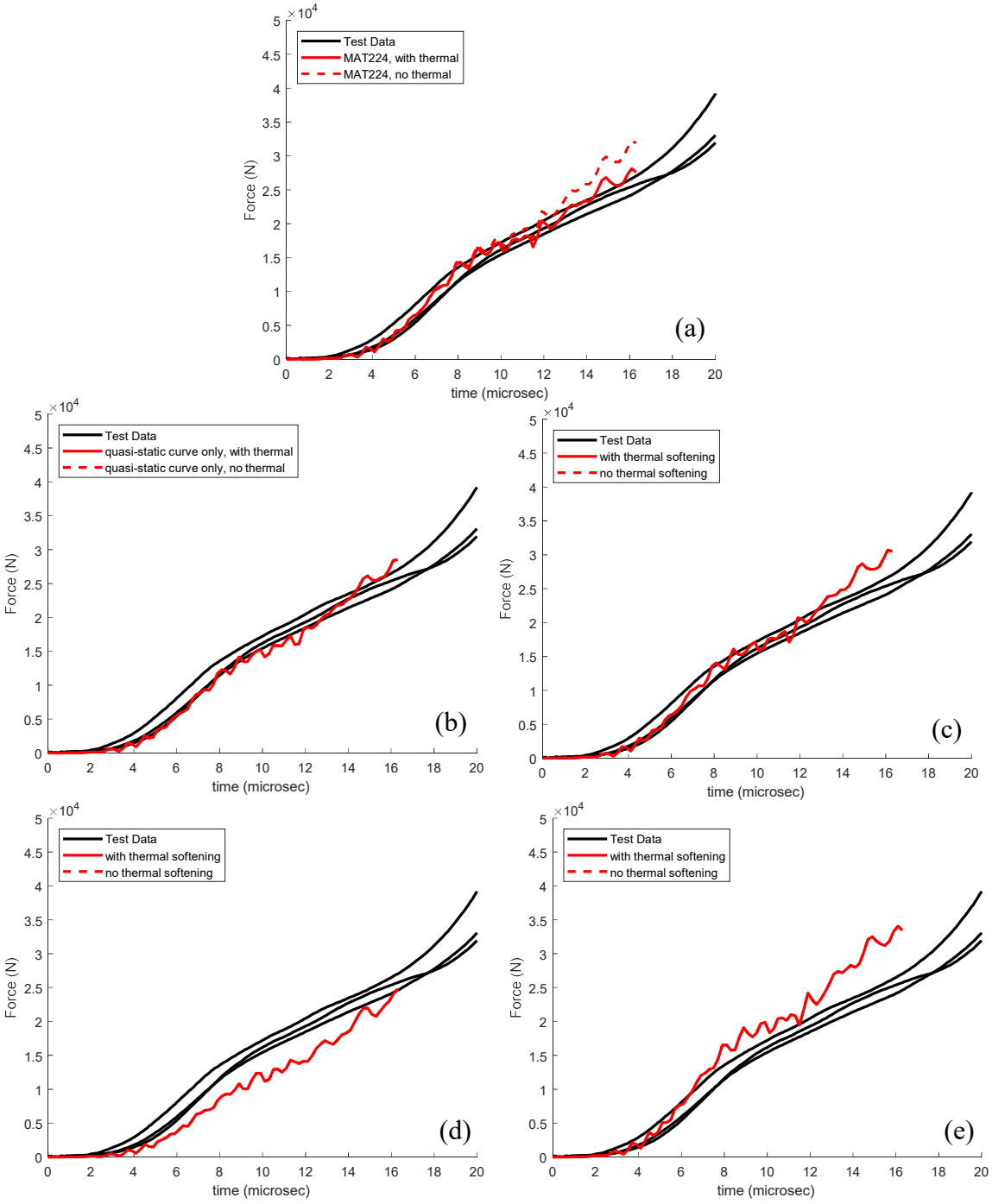

Figure 4.41 Force comparison between direct impact tests on Al2024 5.08 mm long specimens and simulations using (a) AWG *MAT_224 model, (b) Quasi-static curve only, (c) 40,000 s^{-1} curve, (d) scaled peak stress-peak stress curve and (e) scaled peak stress-yield stress curve

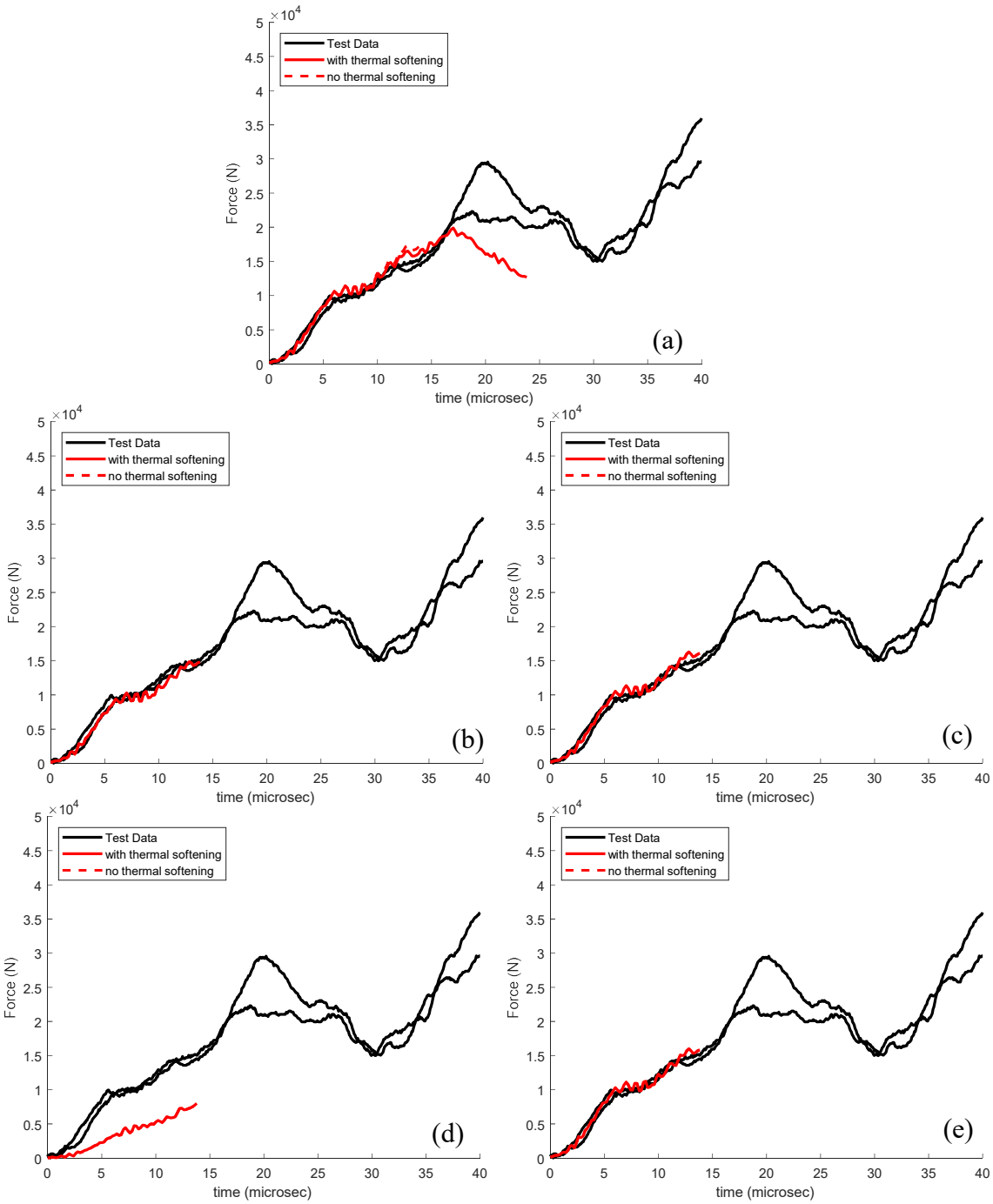

Figure 4.42 Force comparison between direct impact tests on Al2024 10.16 mm long specimens and simulations using (a) AWG *MAT_224 model, (b) Quasi-static curve only, (c) 20,000 s^{-1} curve, (d) scaled peak stress-peak stress curve and (e) scaled peak stress-yield stress curve

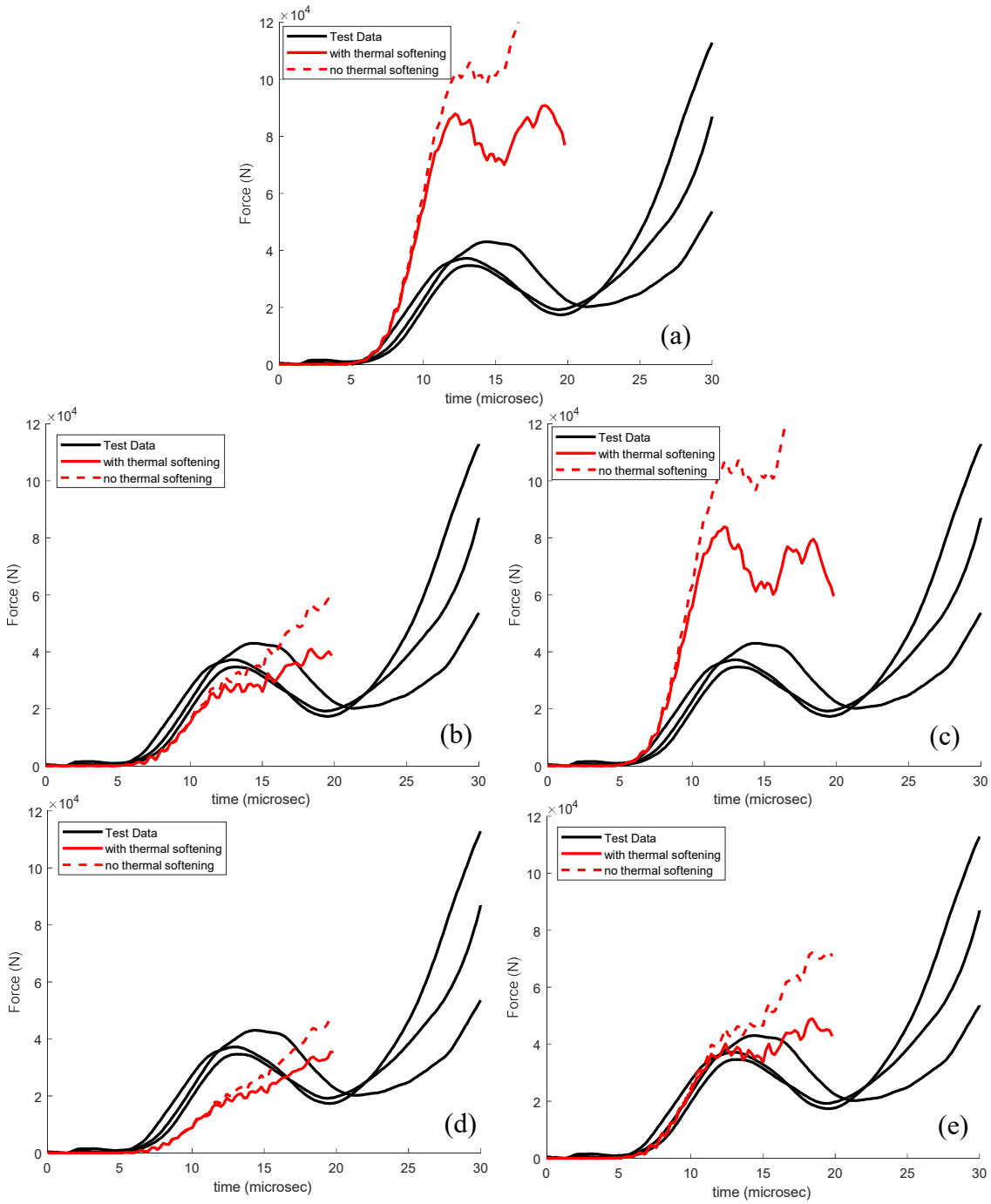

Figure 4.43 Force comparison between direct impact tests on Ti64 5.08 mm long specimens and simulations using (a) AWG *MAT_224 model, (b) Quasi-static curve only, (c) 40,000 s^{-1} curve, (d) scaled peak stress-peak stress curve and (e) scaled peak stress-yield stress curve

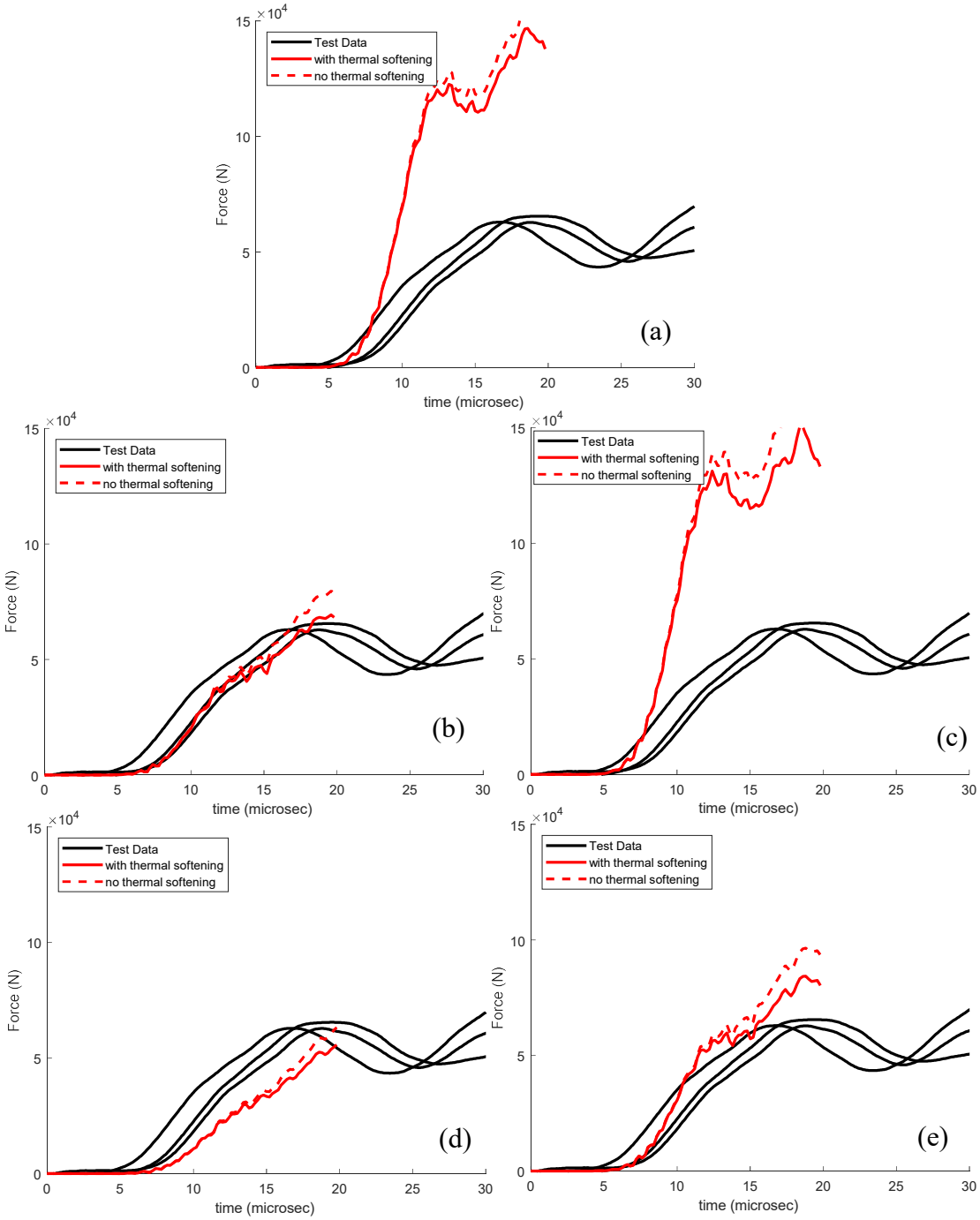

Figure 4.44 Force comparison between direct impact tests on In718 5.08 mm long specimens and simulations using (a) AWG *MAT_224 model, (b) Quasi-static curve only, (c) 40,000 s^{-1} curve, (d) scaled peak stress-peak stress curve and (e) scaled peak stress-yield stress curve

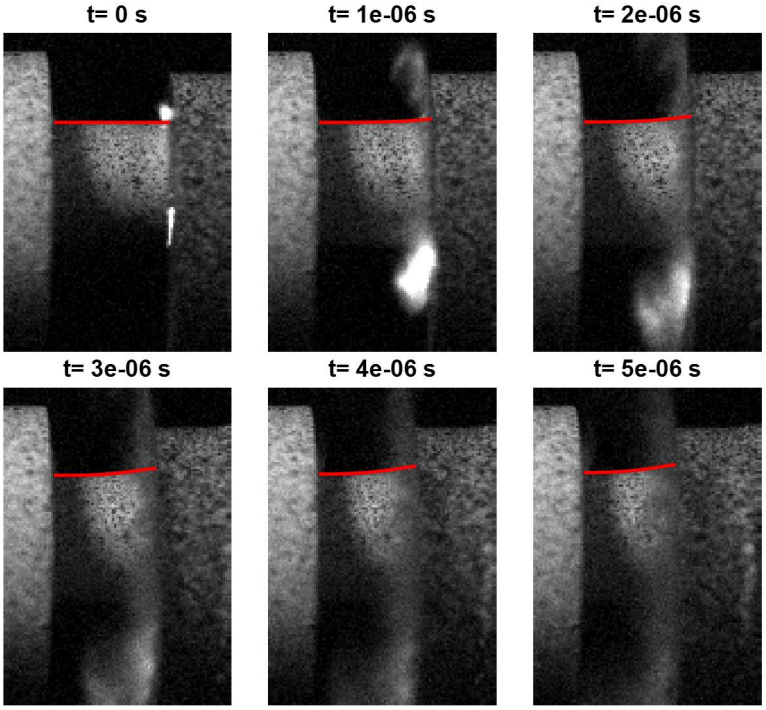

Figure 4.45 Comparison of Al2024 5.08 mm long specimen profile between test DIC images and FEA simulations (red line) using AWG *MAT_224 model with thermal softening

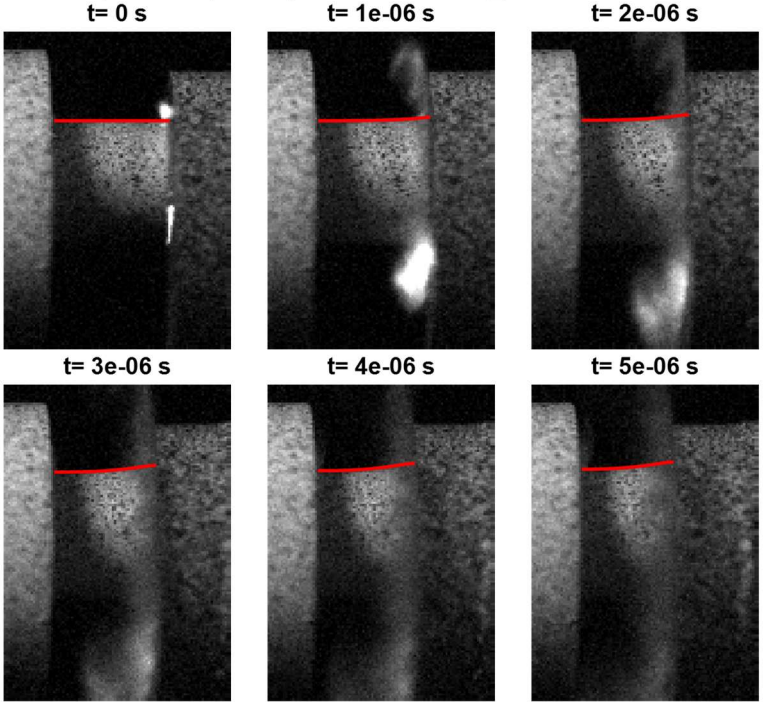

Figure 4.46 Comparison of Al2024 5.08 mm long specimen profile between test DIC images and FEA simulations (red line) using AWG *MAT_224 model without thermal softening

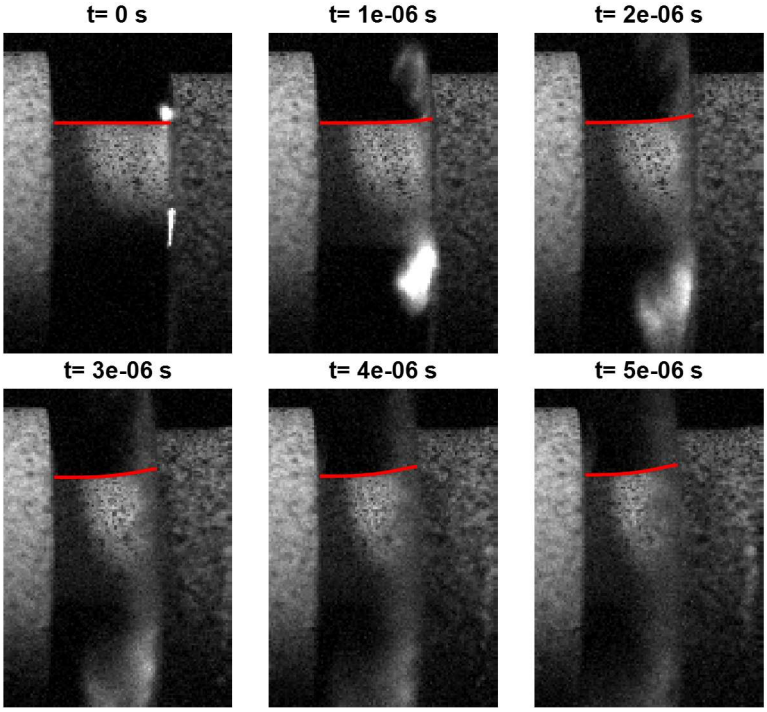

Figure 4.47 Comparison of Al2024 5.08 mm long specimen profile between test DIC images and FEA simulations (red line) using quasi-static curve with thermal softening

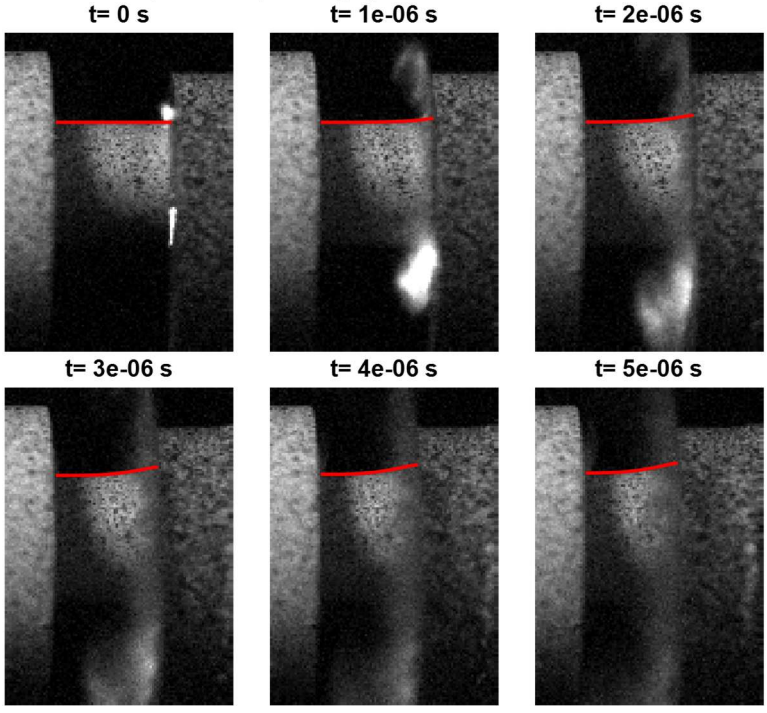

Figure 4.48 Comparison of Al2024 5.08 mm long specimen profile between test DIC images and FEA simulations (red line) using quasi-static curve without thermal softening

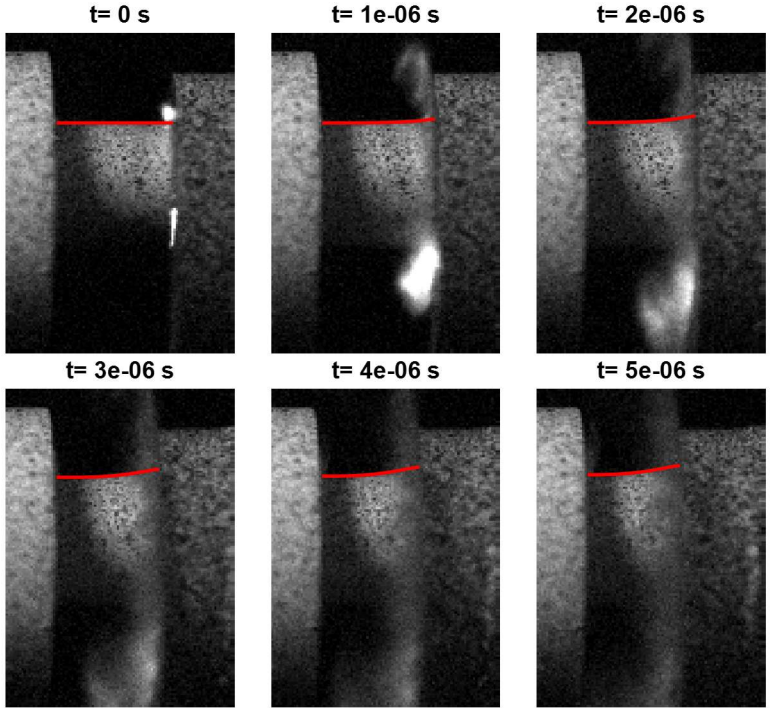

Figure 4.49 Comparison of Al2024 5.08 mm long specimen profile between test DIC images and FEA simulations (red line) using 40,000 s^{-1} curve with thermal softening

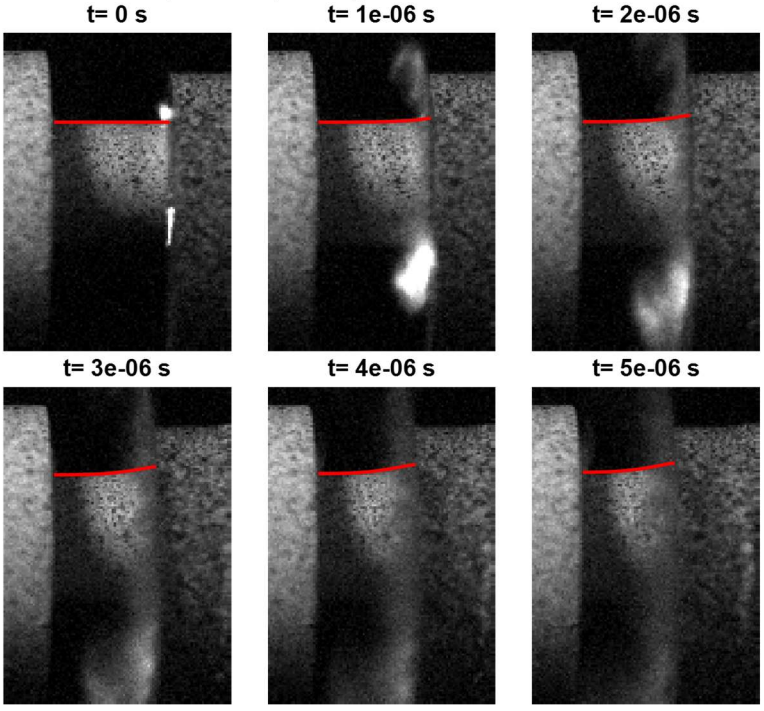

Figure 4.50 Comparison of Al2024 5.08 mm long specimen profile between test DIC images and FEA simulations (red line) using 40,000 s^{-1} curve without thermal softening

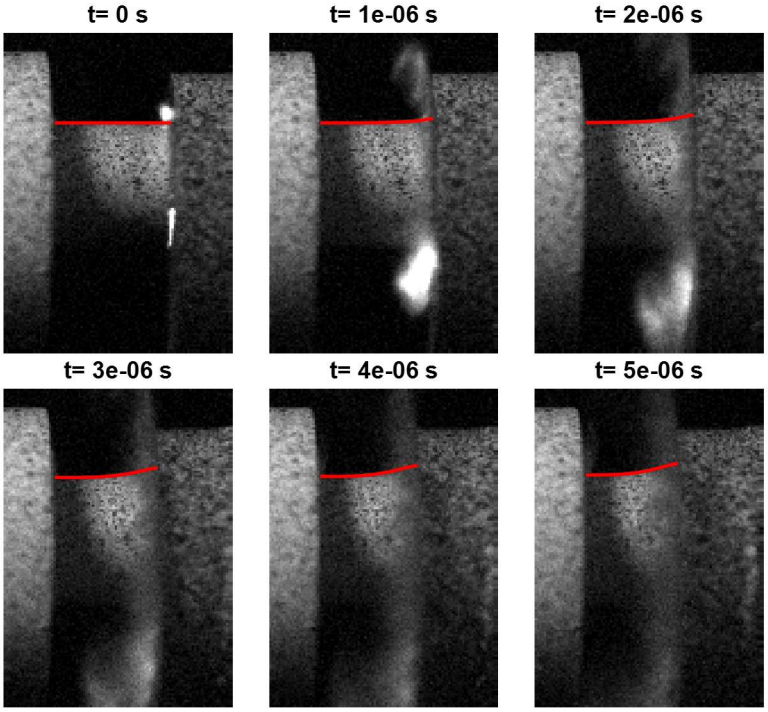

Figure 4.51 Comparison of Al2024 5.08 mm long specimen profile between test DIC images and FEA simulations (red line) using scaled peak stress-peak stress curve with thermal softening

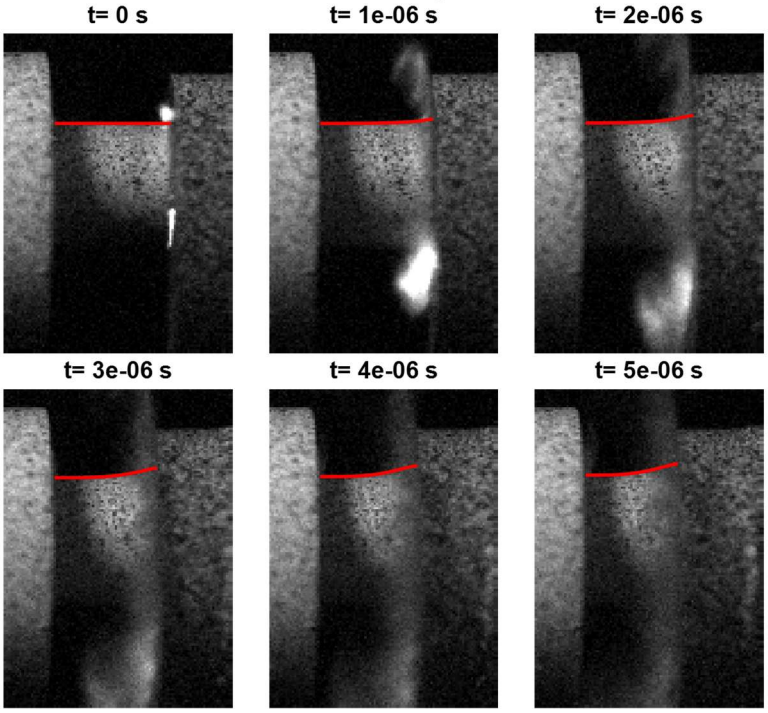

Figure 4.52 Comparison of Al2024 5.08 mm long specimen profile between test DIC images and FEA simulations (red line) using scaled peak stress-peak stress curve without thermal softening

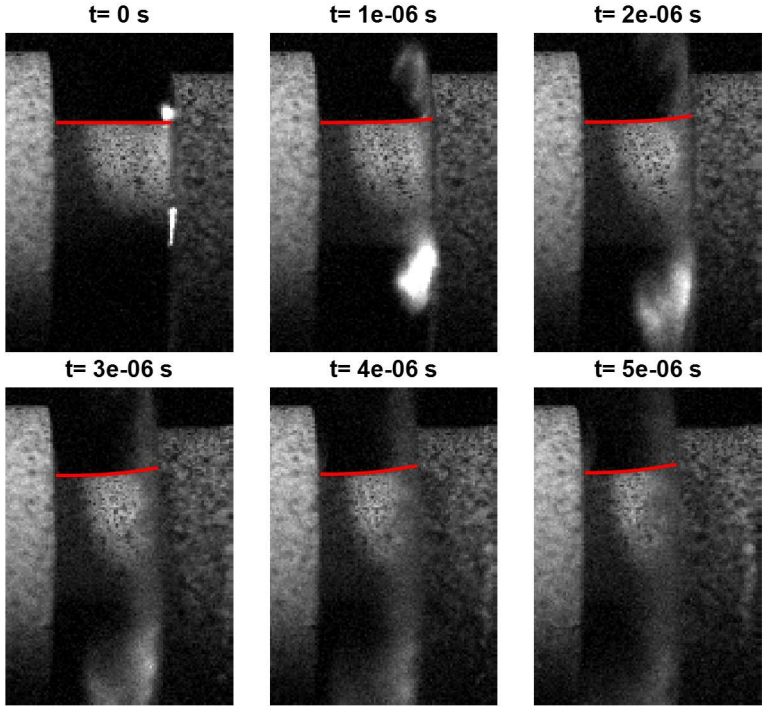

Figure 4.53 Comparison of Al2024 5.08 mm long specimen profile between test DIC images and FEA simulations (red line) using scaled peak stress-yield stress curve with thermal softening

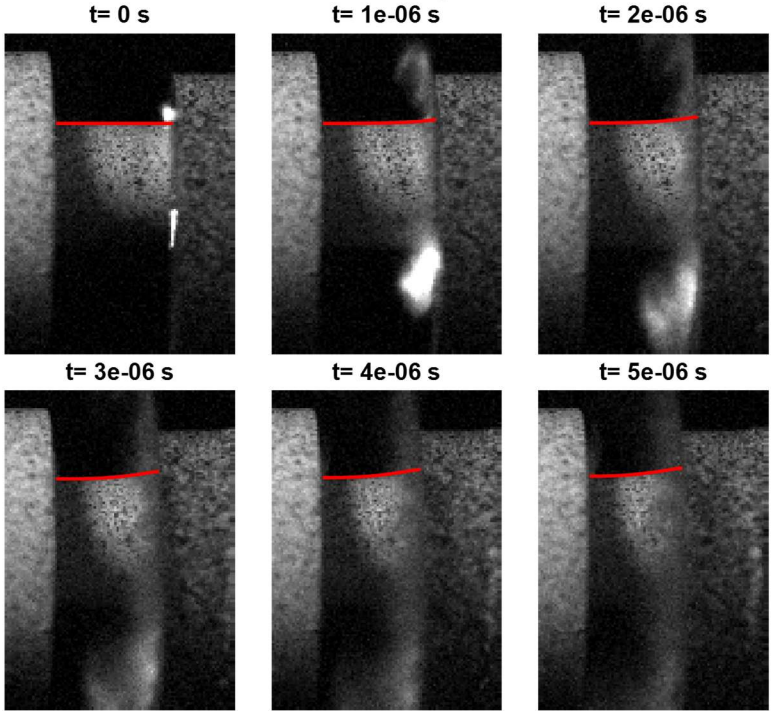

Figure 4.54 Comparison of Al2024 5.08 mm long specimen profile test DIC images and FEA simulations (red line) using scaled peak stress-yield stress curve without thermal softening

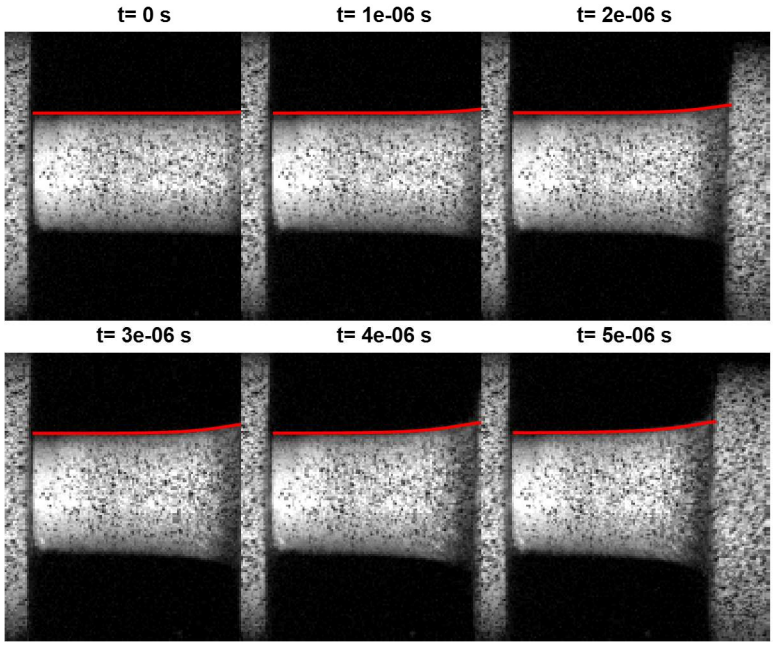

Figure 4.55 Comparison of Al2024 10.16 mm long specimen profile between test DIC images and FEA simulations (red line) using AWG *MAT_224 model with thermal softening

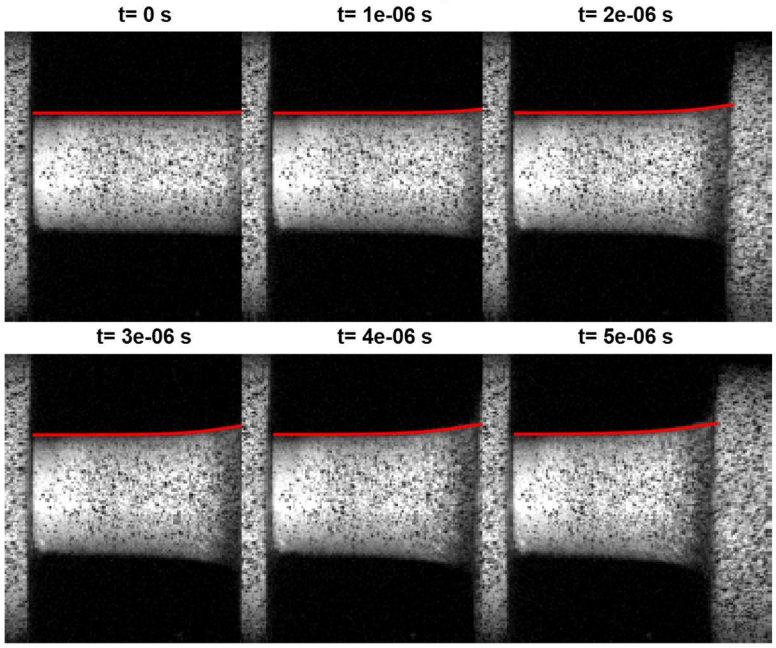

Figure 4.56 Comparison of Al2024 10.16 mm long specimen profile test DIC images and FEA simulations (red line) using AWG *MAT_224 model without thermal softening

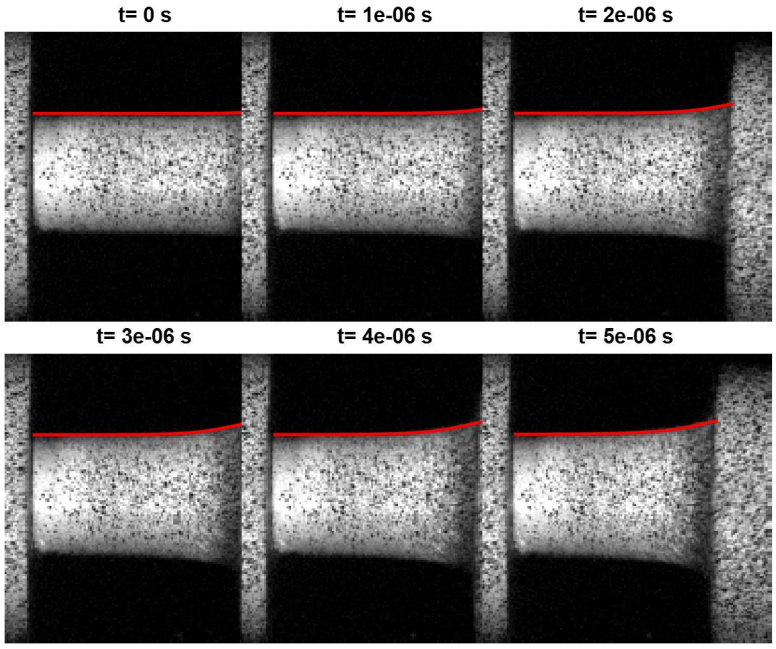

Figure 4.57 Comparison of Al2024 10.16 mm long specimen profile between test DIC images and FEA simulations (red line) using quasi-static curve with thermal softening

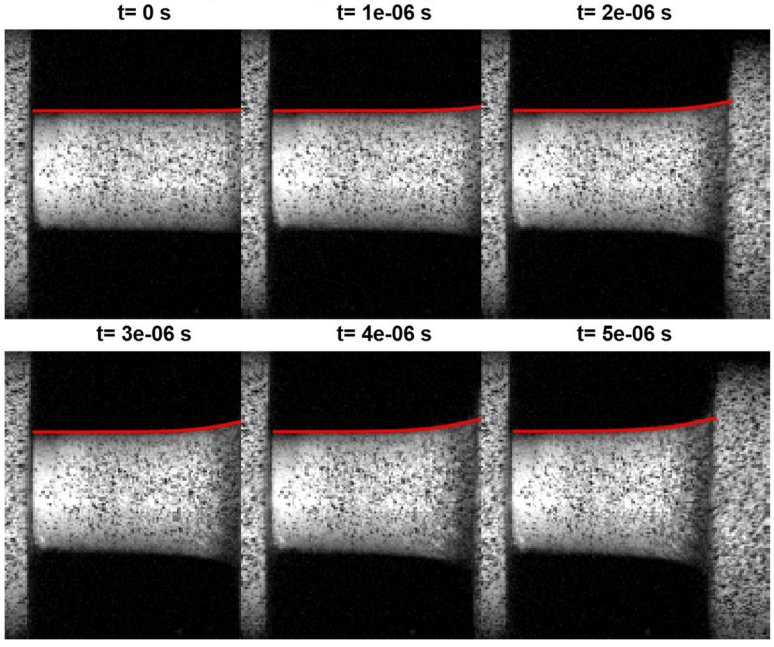

Figure 4.58 Comparison of Al2024 10.16 mm long specimen profile between test DIC images and FEA simulations (red line) using quasi-static curve without thermal softening

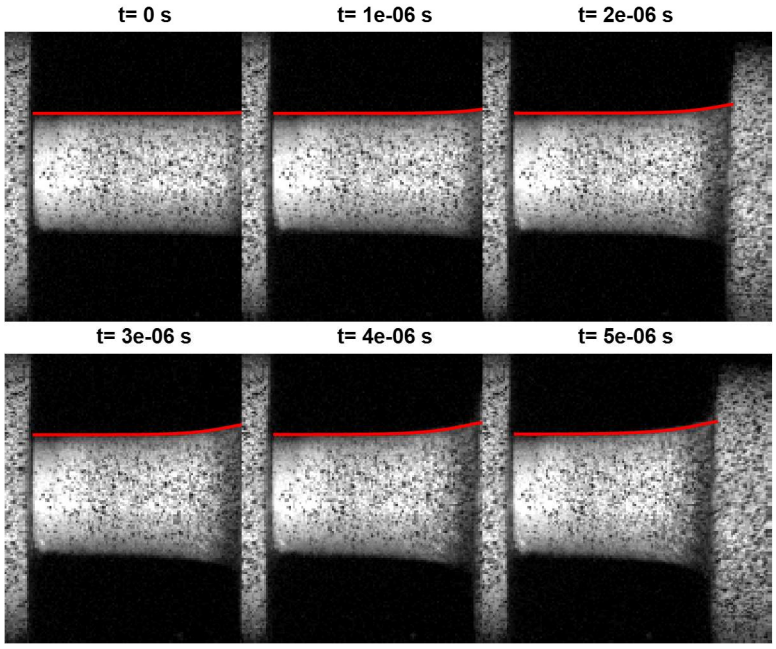

Figure 4.59 Comparison of Al2024 10.16 mm long specimen profile between test DIC images and FEA simulations (red line) using 20,000 s^{-1} with thermal softening

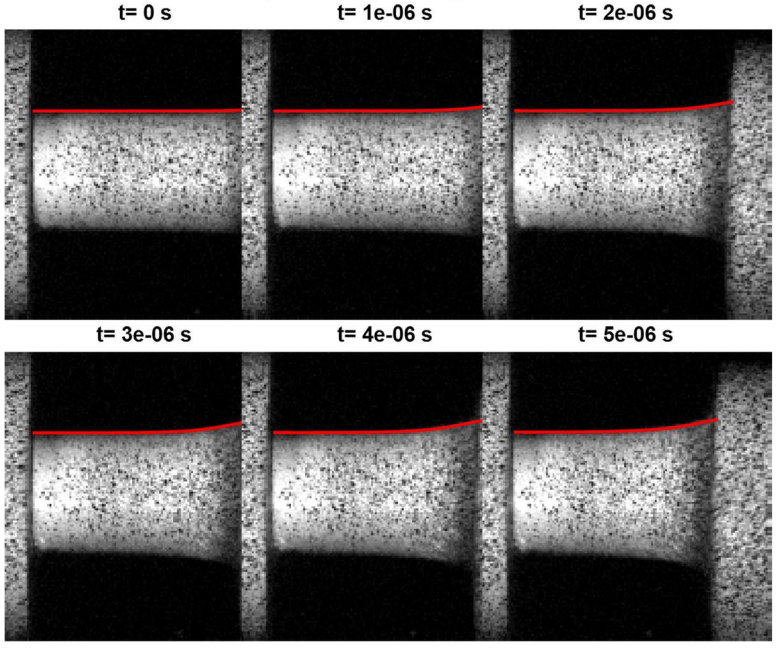

Figure 4.60 Comparison of Al2024 10.16 mm long specimen profile between test DIC images and FEA simulations (red line) using 20,000 s^{-1} without thermal softening

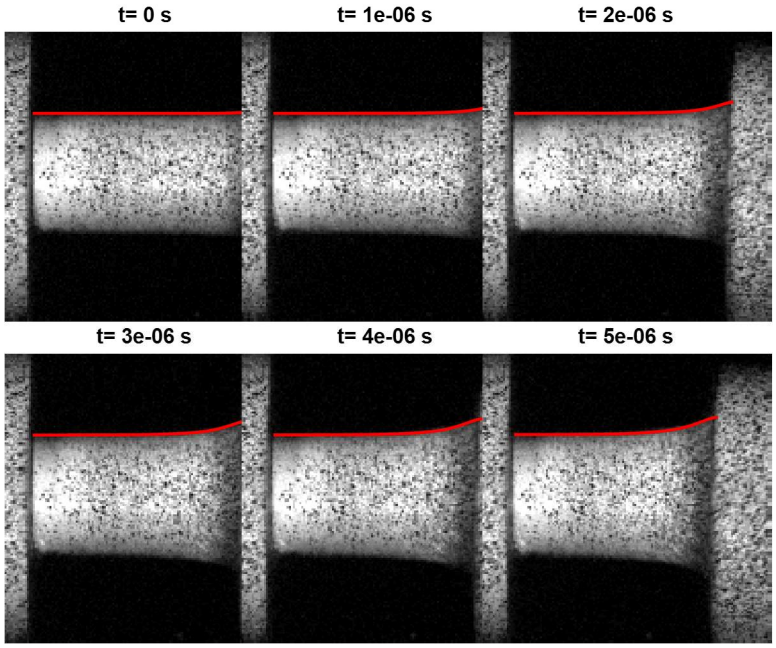

Figure 4.61 Comparison of Al2024 10.16 mm long specimen profile between test DIC images and FEA simulations (red line) using scaled peak stress-peak stress curve with thermal softening

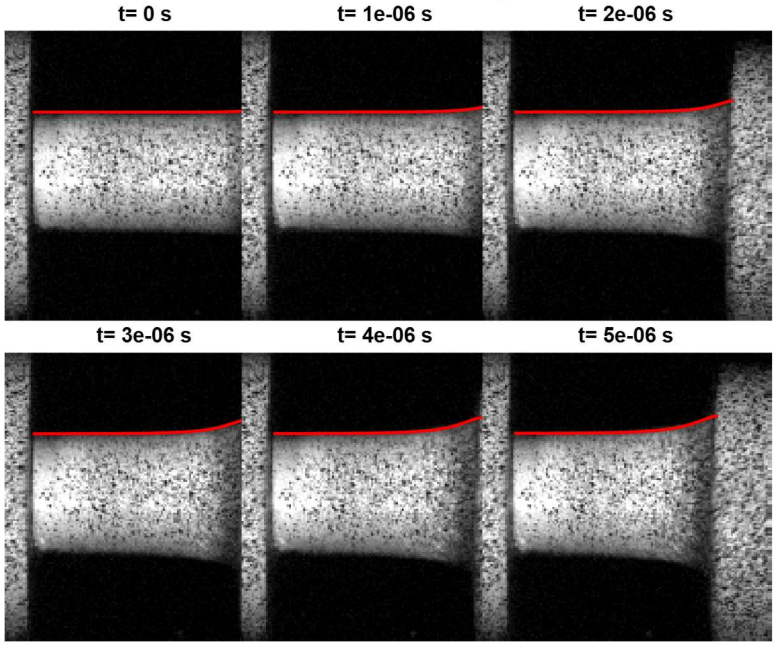

Figure 4.62 Comparison of Al2024 10.16 mm long specimen profile between test DIC images and FEA simulations (red line) using scaled peak stress-peak stress curve without thermal softening

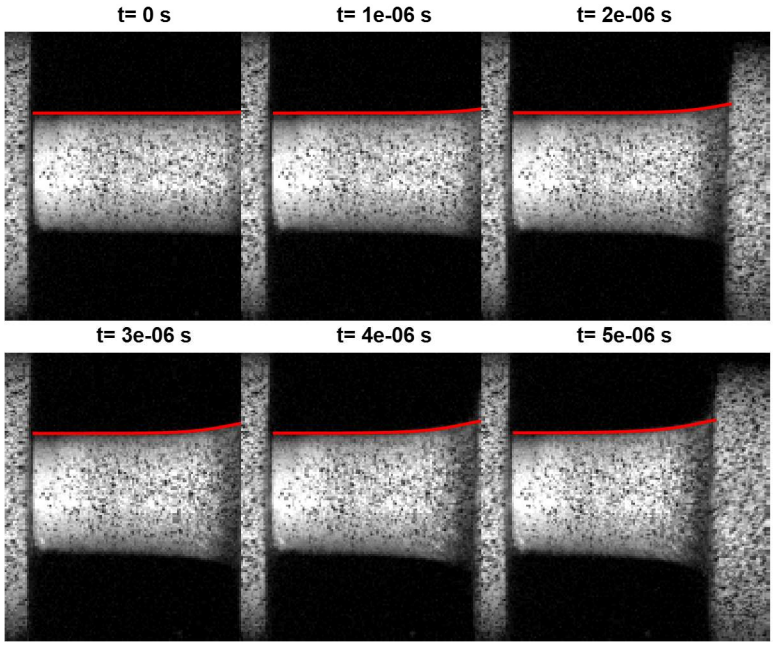

Figure 4.63 Comparison of Al2024 10.16 mm long specimen profile between test DIC images and FEA simulations (red line) using scaled peak stress-yield stress curve with thermal softening

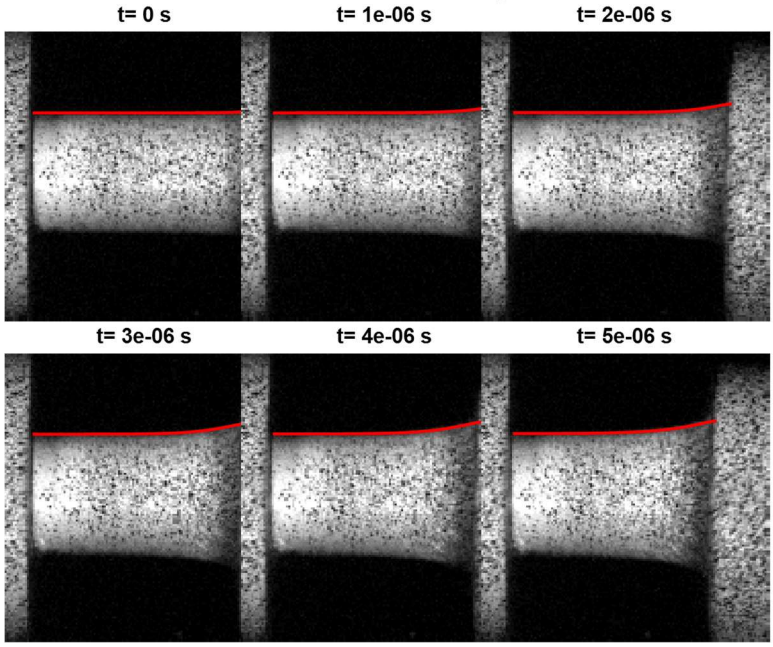

Figure 4.64 Comparison of Al2024 10.16 mm long specimen profile between test DIC images and FEA simulations (red line) using scaled peak stress-yield stress curve without thermal softening

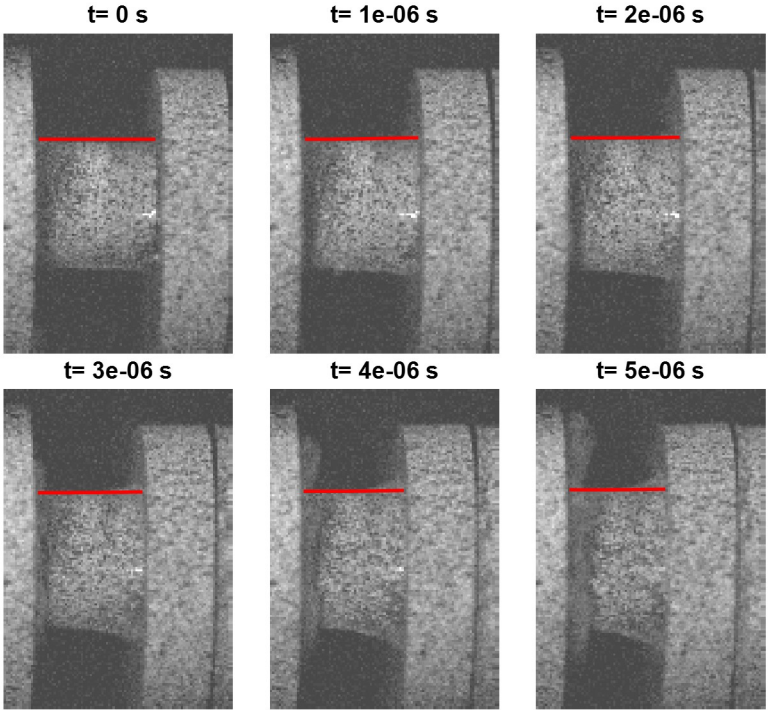

Figure 4.65 Comparison of Ti64 5.08 mm long specimen profile between test DIC images and FEA simulations (red line) using AWG *MAT_224 model with thermal softening

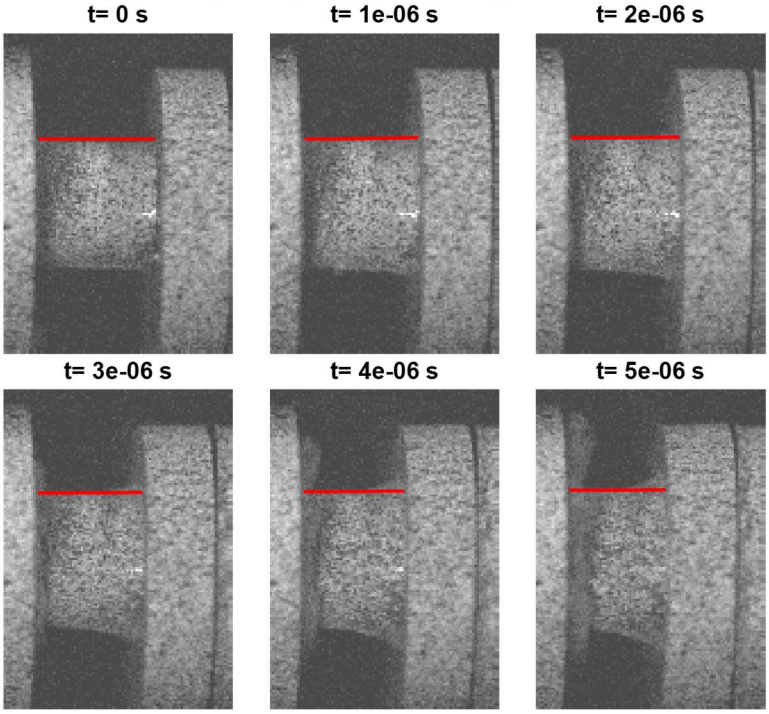

Figure 4.66 Comparison of Ti64 5.08 mm long specimen profile between test DIC images and FEA simulations (red line) using AWG *MAT_224 model without thermal softening

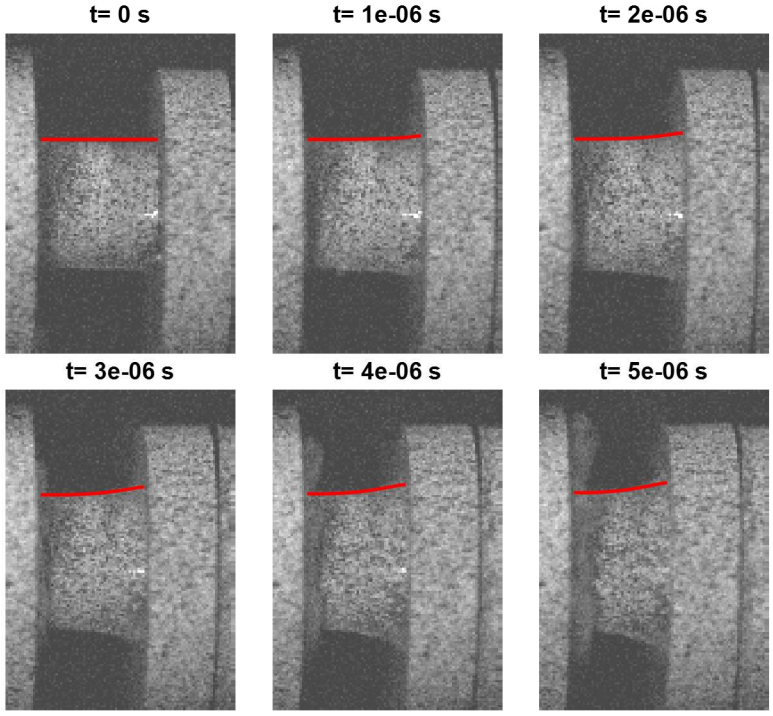

Figure 4.67 Comparison of Ti64 5.08 mm long specimen profile between test DIC images and FEA simulations (red line) using quasi-static curve with thermal softening

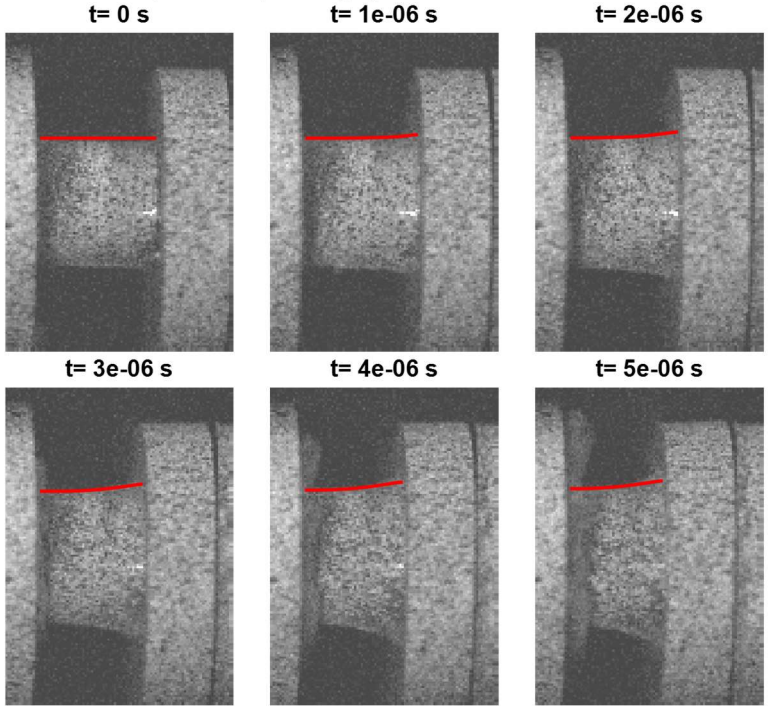

Figure 4.68 Comparison of Ti64 5.08 mm long specimen prfile between test DIC images and FEA simulations (red line) using quasi-static curve without thermal softening

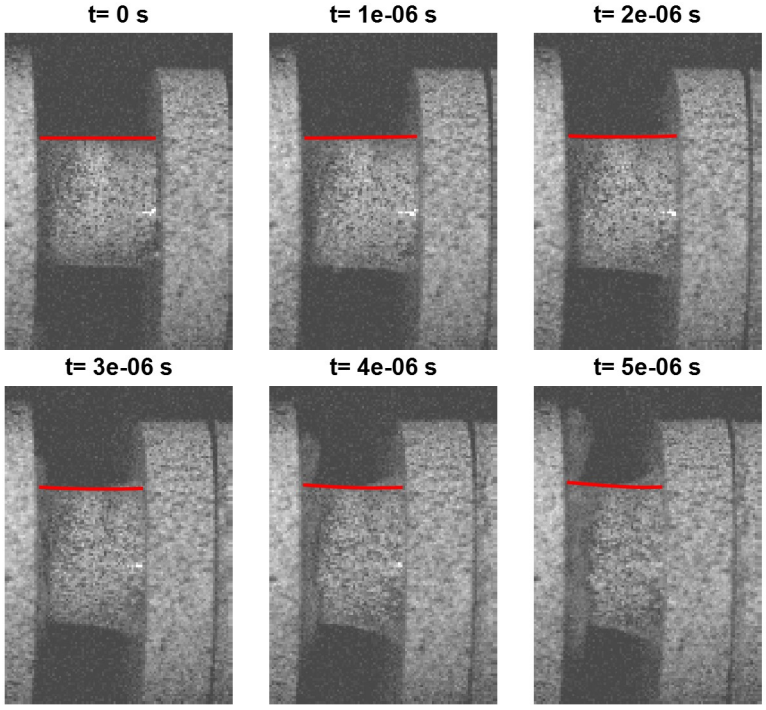

Figure 4.69 Comparison of Ti64 5.08 mm long specimen profile between test DIC images and FEA simulations (red line) using 40,000 s^{-1} with thermal softening

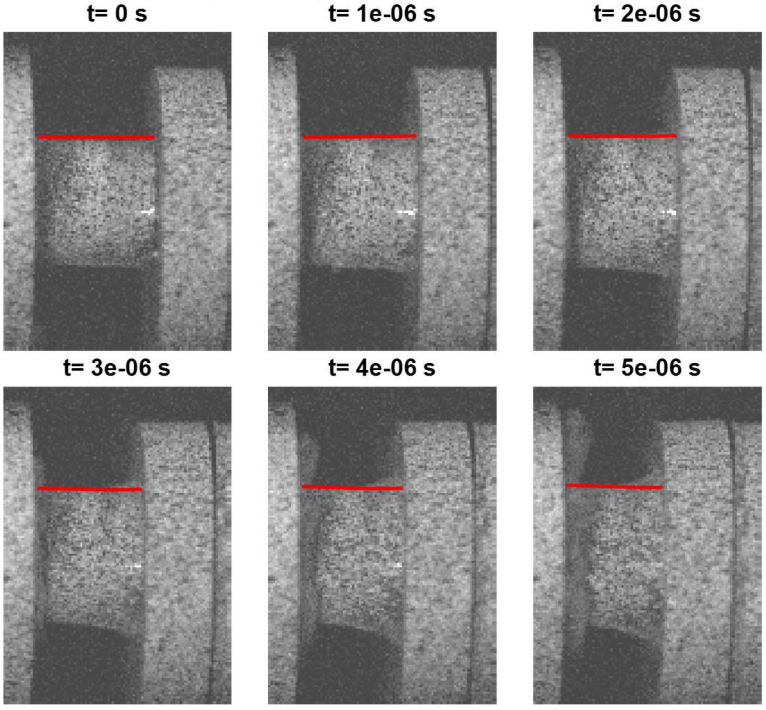

Figure 4.70 Comparison of Ti64 5.08 mm long specimen pofile between test DIC images and FEA simulations (red line) using 40,000 s^{-1} without thermal softening

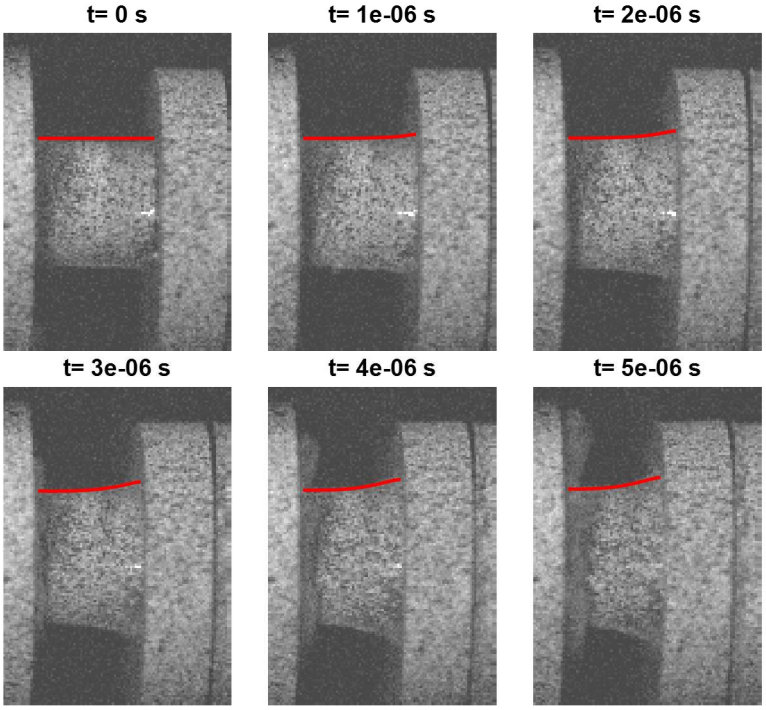

Figure 4.71 Comparison of Ti64 5.08 mm long specimen profile between test DIC images and FEA simulations (red line) using scaled peak stress-peak stress curve with thermal softening

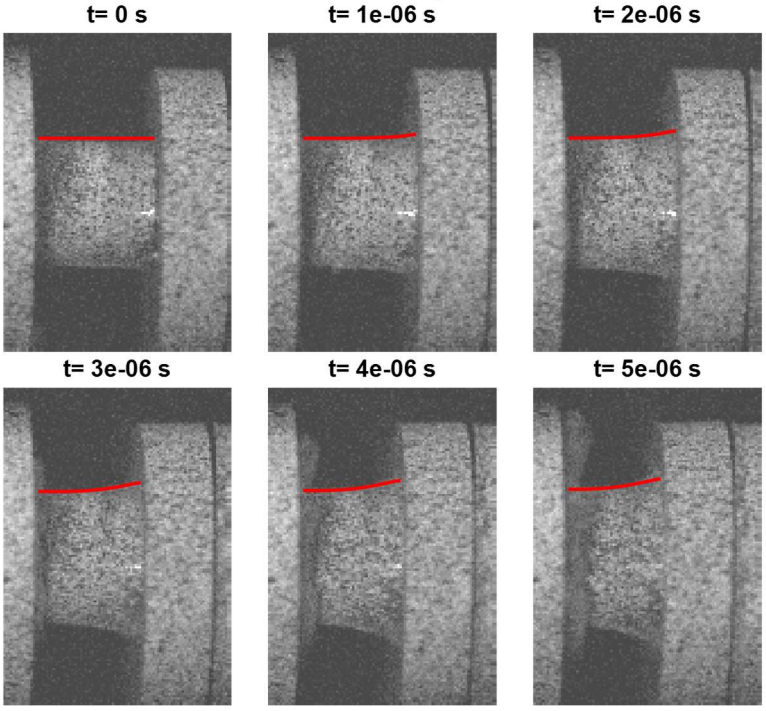

Figure 4.72 Comparison of Ti64 5.08 mm long specimen profile between test DIC images and FEA simulations (red line) using scaled peak stress-peak stress curve without thermal softening

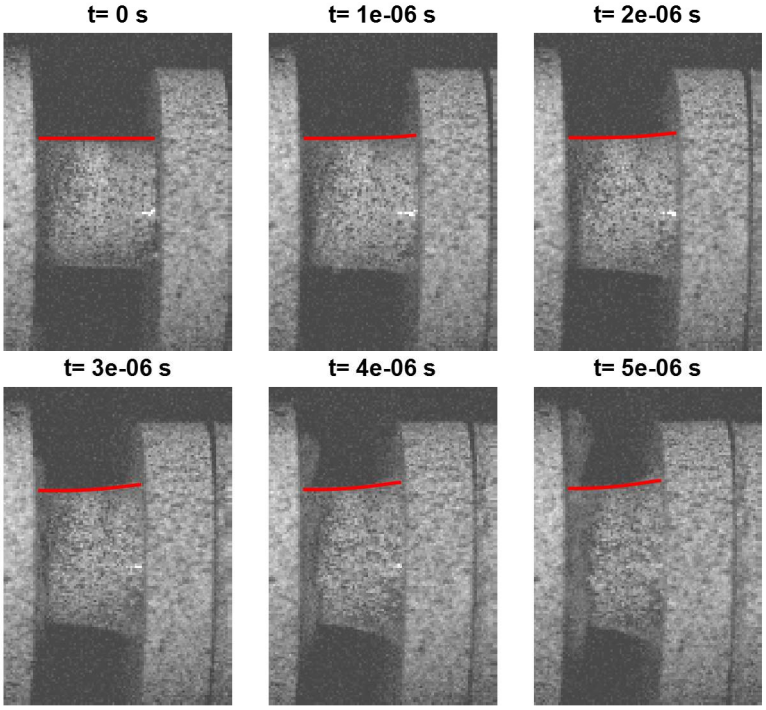

Figure 4.73 Comparison of Ti64 5.08 mm long specimen profile between test DIC images and FEA simulations (red line) using scaled peak stress-yield stress curve with thermal softening

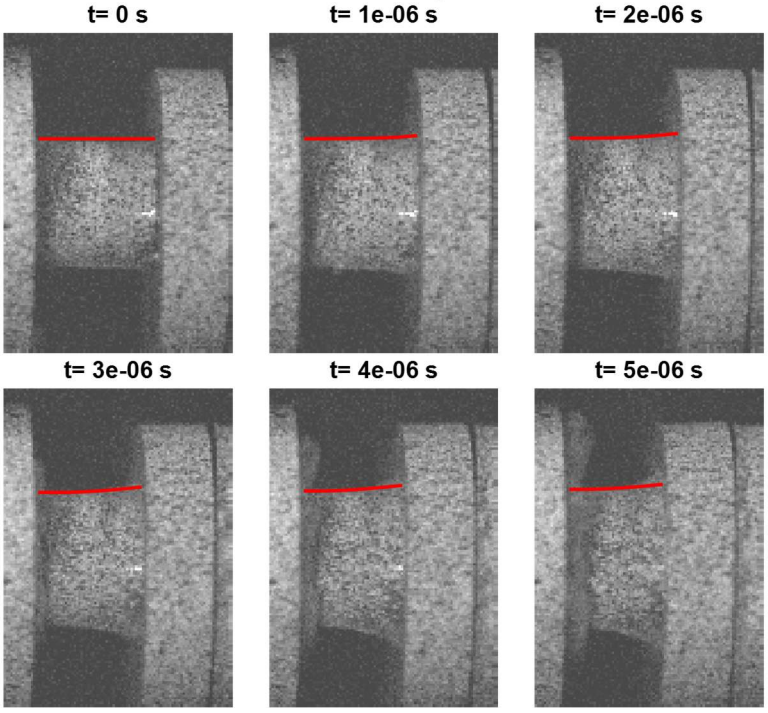

Figure 4.74 Comparison of Ti64 5.08 mm long specimen profile between test DIC images and FEA simulations (red line) using scaled peak stress-yield stress curve without thermal softening

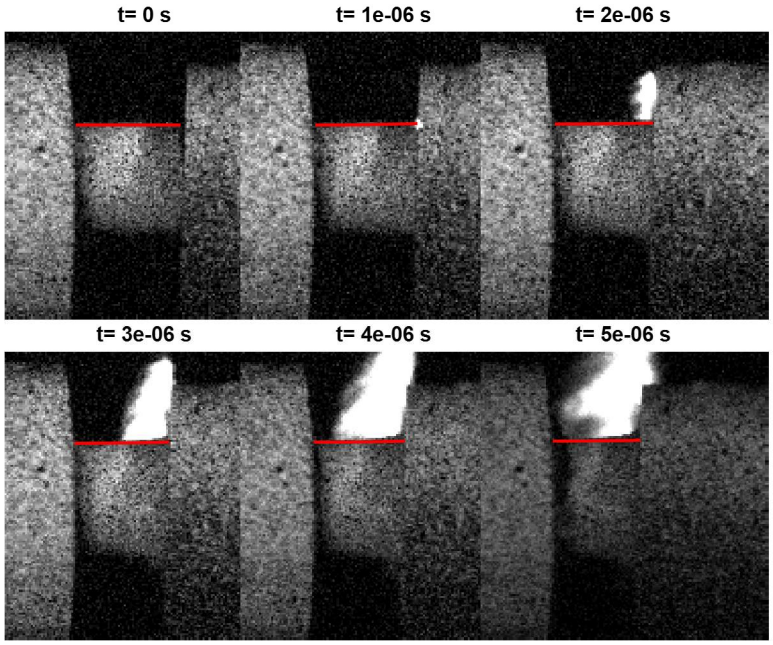

Figure 4.75 Comparison of In718 5.08 mm long specimen 5.08 mm between test DIC images and FEA simulations (red line) using AWG *MAT_224 model with thermal softening

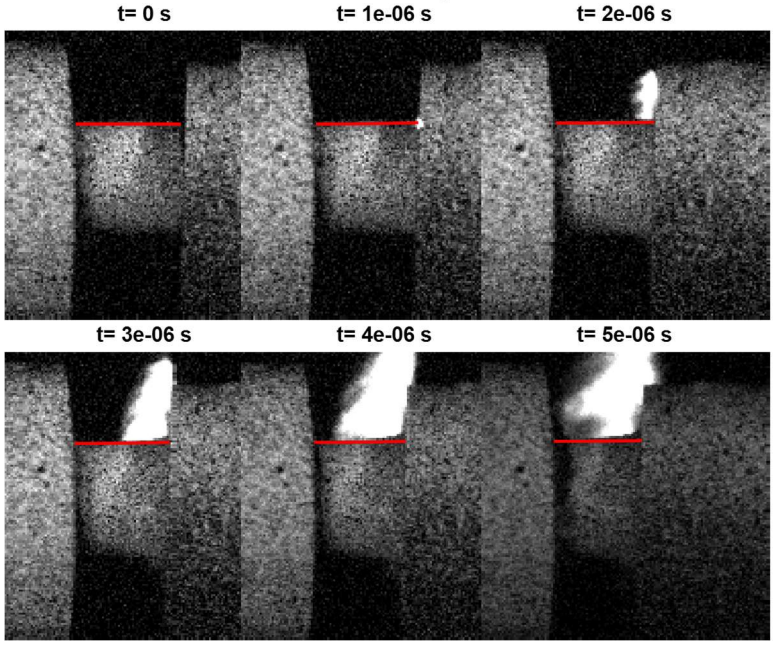

Figure 4.76 Comparison of In718 5.08 mm long specimen profile between test DIC images and FEA simulations (red line) using AWG *MAT_224 model without thermal softening

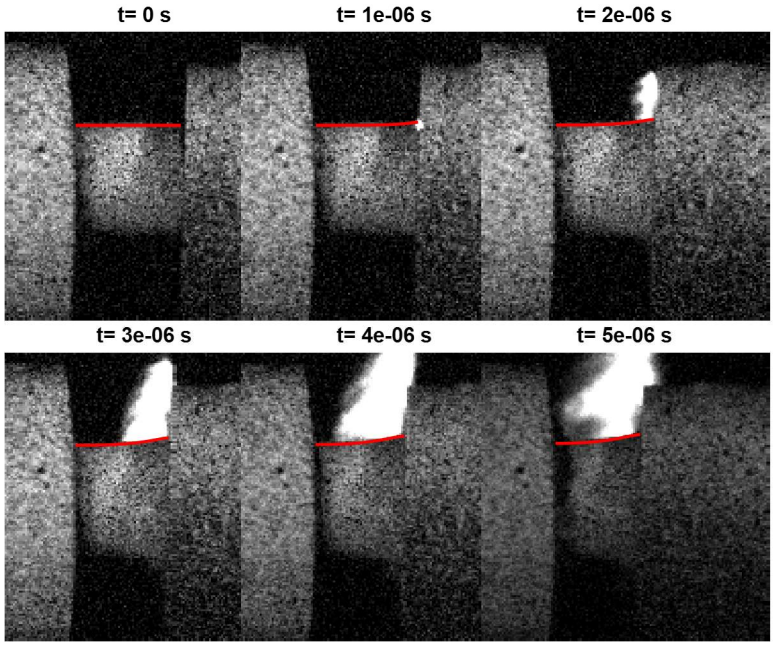

Figure 4.77 Comparison of In718 5.08 mm long specimen profile between test DIC images and FEA simulations (red line) using quasi-static curve with thermal softening

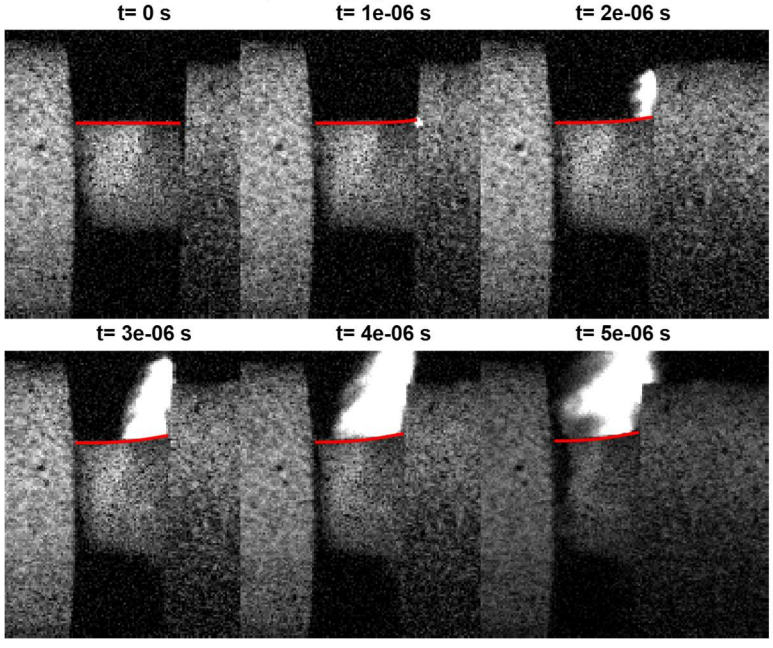

Figure 4.78 Comparison of In718 5.08 mm long specimen profile between test DIC images and FEA simulations (red line) using quasi-static curve without thermal softening

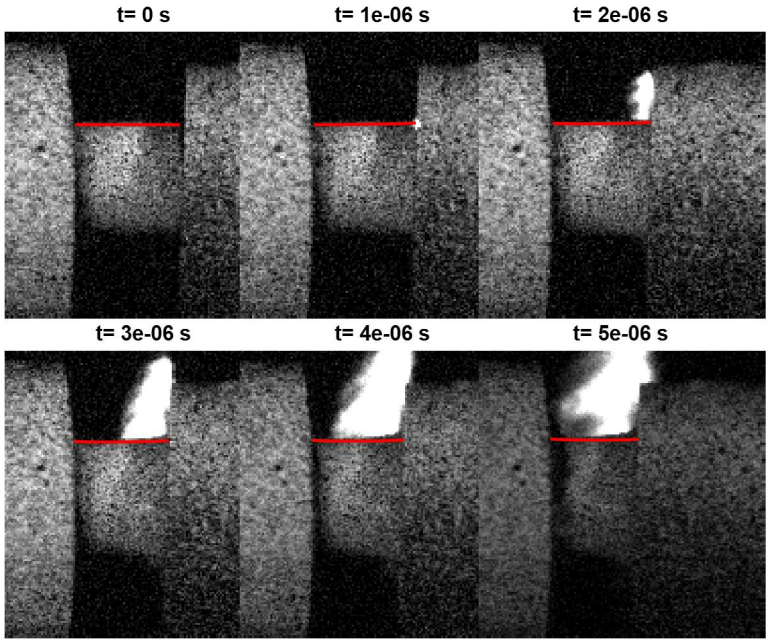

Figure 4.79 Comparison of In718 5.08 mm long specimen profile between test DIC images and FEA simulations (red line) using 40,000 s^{-1} with thermal softening

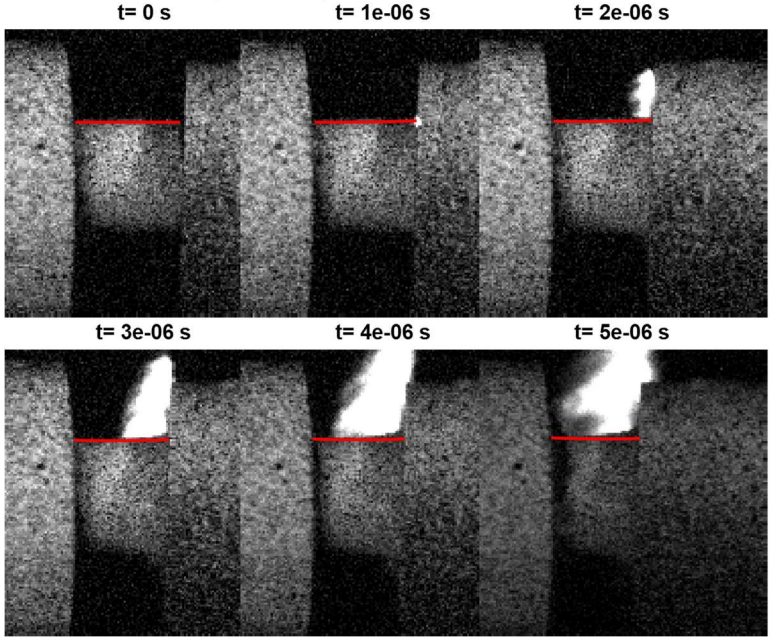

Figure 4.80 Comparison of In718 5.08 mm long specimen profile between test DIC images and FEA simulations (red line) using 40,000 s^{-1} without thermal softening

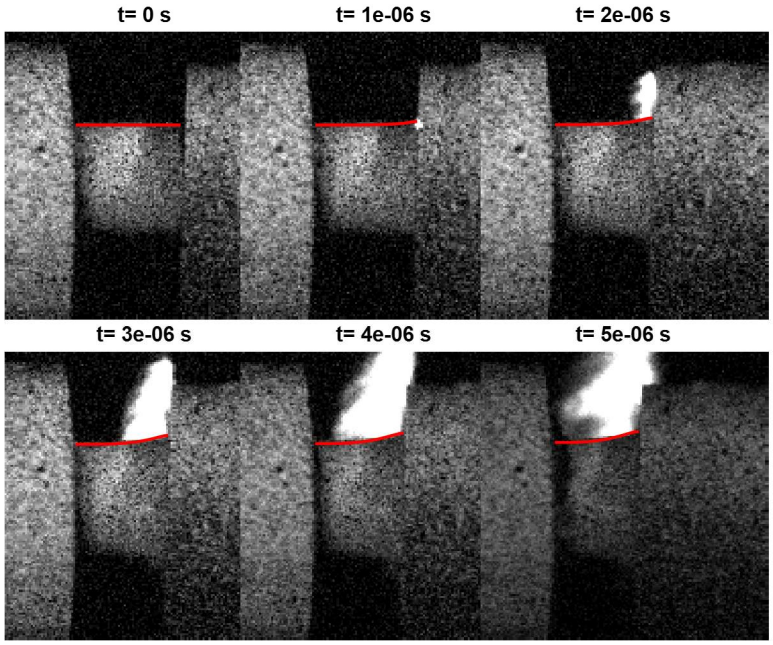

Figure 4.81 Comparison of In718 5.08 mm long specimen profile between test DIC images and FEA simulations (red line) using scaled peak stress-peak stress curve with thermal softening

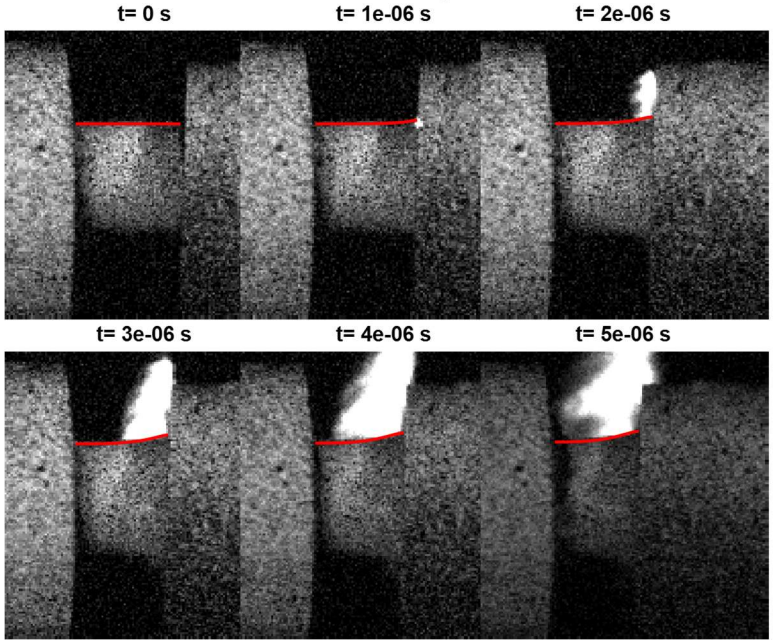

Figure 4.82 Comparison of In718 5.08 mm long specimen profile between test DIC images and FEA simulations (red line) using scaled peak stress-peak stress curve without thermal softening

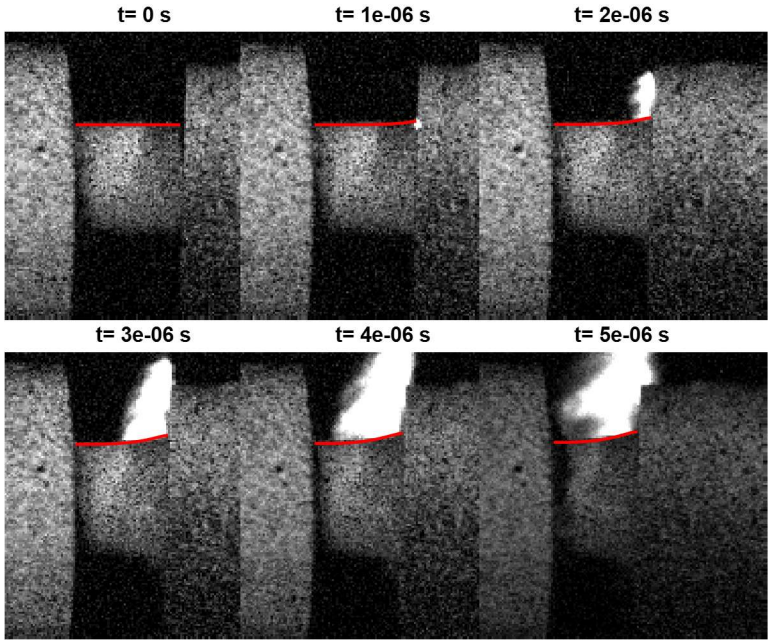

Figure 4.83 Comparison of In718 5.08 mm long specimen profile between test DIC images and FEA simulations (red line) using scaled peak stress-yield stress curve with thermal softening

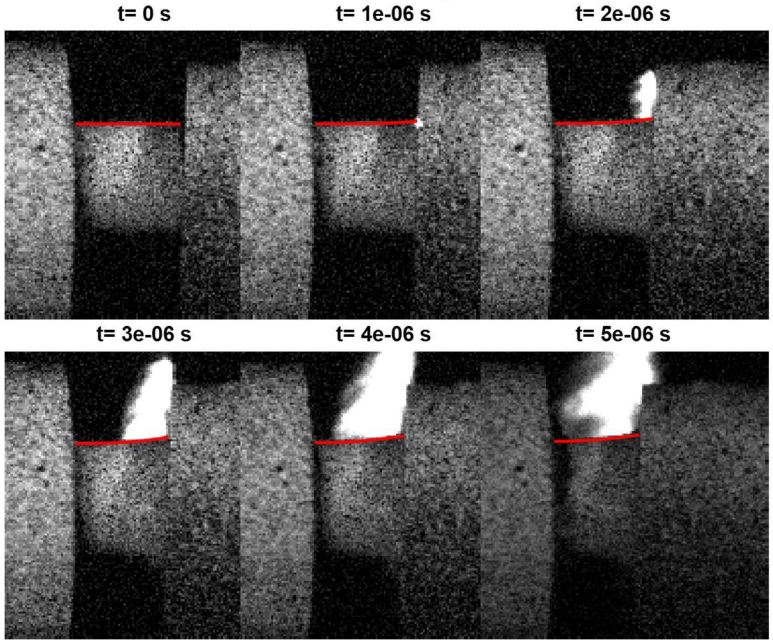

Figure 4.84 Comparison of In718 5.08 mm long specimen profile between test DIC images and FEA simulations (red line) using scaled peak stress-yield stress curve without thermal softening

Figure 4.41 shows that for the Al2024 5.08 mm specimens, all the simulation models generally agree with the force levels seen in the tests. The full *MAT_224 model, the quasi-static curve, and the 40,000 s^{-1} curve give the best matches to the measured experimental force. The simulation using the peak stress-to-peak stress curve shown in Figure 4.41(d) slightly under predicts the force level, and the simulation using the peak stress-to-yield stress curve in Figure 4.41(e) slightly over predicts the force level. Figure 4.45 - Figure 4.54 show that all the Al2024 5.08 mm specimen material models predict relatively similar deformation, and each generally agrees with the deformed specimen shape observed in the tests. These results indicate that Al2024 exhibits very little strain rate hardening during these tests.

A similar conclusion can be drawn from the Al2024 10.16 mm test and simulation results shown in Figure 4.42 and Figure 4.55 - Figure 4.64. The *MAT_224 model, quasi-static curve, 20,000 s^{-1} curve, and scaled peak stress-to-yield stress curve all predict the same force level seen in the experiments. The scaled peak stress-to-peak stress curve, however, dramatically under predicts the force level. This is not unexpected, as in Figure 4.40(b) it can be seen that the scaled peak stress-to-peak stress curve is much lower than the other stress-strain curves used to model the Al2024 10.16 mm specimen. Therefore it is not surprising that this curve under predicts the experimental force. In Figure 4.55 - Figure 4.64, there is no significant difference between the deformed specimen shape predicted by each material model, and all generally agree with the experimentally observed specimen shape. These results again indicate the Al2024 stress vs. strain response is not sensitive to the strain rate, even at these higher strain rates. It also indicates that the experimentally measured force is a more sensitive metric for comparing the test and simulation results. It is clear in Figure 4.42(d) that the scaled peak stress-to-peak stress curve does not

accurately capture the force from the experiments, yet it does seem to match the deformed specimen shape in Figure 4.61 and Figure 4.62.

The fact that these experimental results indicate that Al2024 exhibits no or very little rate sensitivity is in line with previous experiments, which have shown that Al2024 exhibits minimal strain rate sensitivity up to rates on the order of 10^3 s^{-1} [9]. It is also in line with the results determined by the FAA AWG in creating the Al2024 *MAT_224 material model and validating it against plate impact experiments, which indicate that Al2024 does not exhibit significant strain rate hardening until rates on the order of 10^5 s^{-1} are reached [11].

The simulation results for Ti64 and In718 show much more noticeable differences between the different material models than the Al2024 results. This is not unexpected, as the Ti64 and In718 input curves in Figure 4.40 have much greater differences in magnitude than the Al2024 input curves. Figure 4.43 shows that the Ti64 *MAT_224 model and the 40,000 s^{-1} curve dramatically over predict the amount of force compared to what is observed in the experiments. These same material models also under predict the amount of non-uniform deformation that occurs along the specimen length, as shown in Figure 4.65 - Figure 4.66 and Figure 4.69 - Figure 4.70. This indicates that the AWG *MAT_224 material model (from which the 40,000 s^{-1} curve is taken) over predicts the amount of strain rate hardening that occurs at these elevated rates. These simulated material models exhibit a stiffer response than what is observed in the experiments.

The Ti64 quasi-static curve slightly under predicts the force, and the scaled peak stress-to-peak stress dramatically under predicts the force in Figure 4.43. The scaled peak stress-to-yield stress curve shown in Figure 4.43(e) gives the best match to the experimental force. It can be seen that the quasi-static curve, scaled peak stress-to-peak stress curve, and scaled peak stress-to-yield stress curves all predict very similar non-uniform deformation of the specimen in Figure 4.67 -

Figure 4.68 and Figure 4.71 - Figure 4.74. Each of these material models generally matches the observed deformation of the specimen seen in the experiments.

The In718 simulations using the *MAT_224 model and 40,000 s^{-1} curve in Figure 4.44(a) and (c) also over predict the load compared to the experiments. This indicates that these models over predict the amount of strain rate hardening of In718 at elevated strain rates, similar to what is observed for the Ti64 simulations. Unlike the Ti64 simulations, the In718 model with the scaled peak stress-to-yield stress curve in Figure 4.44(e) slightly over predicts the force. The In718 model with the scaled peak stress-to-peak stress curve in Figure 4.44(d) under predicts the force. The quasi-static curve in Figure 4.44(c) gives the best match to the experimental force data. Similar to Ti64, the In718 *MAT_224 model and the 40,000 s^{-1} curve under predict the amount of non-uniform deformation that occurs along the specimen length, as shown in Figure 4.75 - Figure 4.76 and Figure 4.79 - Figure 4.80. The other In718 material models all generally agree with the observed specimen deformation, as seen in Figure 4.77 - Figure 4.78 and Figure 4.81 -Figure 4.84. The scaled peak stress-to-yield stress curve does appear to slightly under predict the amount of mushrooming and radial expansion at the impact edge. These results indicate that In718 exhibits either no strain rate hardening, or only a very slight amount of strain rate hardening at these elevated strain rates.

As noted, the results indicating Al2024 does not exhibit strain rate hardening is supported by prior research. However, the direct impact test results for Ti64 and In718 are contrary to previous research on these materials. While the analysis of the direct impact tests indicate that Ti64 exhibits a modest amount of strain rate hardening, it is lower than what is used in the Ti64 AWG *MAT_224 model. This model is calibrated to match the results of plate impact experiments [36]. It is doubtful that lowering the amount of strain rate hardening in the model so that the

simulation results match these direct impact SHB experiments would also yield simulation results that still accurately match to the plate impact experiments. Likewise while the In718 direct impact SHB experiments indicate this material exhibits very little or no strain rate hardening at these rates, this is contradicted by prior experiments that do show strain rate hardening [33] and by the In718 *MAT_224 model calibration that also requires strain rate hardening in order to match the plate impact experiments [38].

One hypothesis to explain this discrepancy is that the Ti64 and In718 specimens undergo premature fracture at the impact edge early on in the direct impact tests. This would create a weaker material response, as the fractured material cannot support the same amount of load compared to the material when it is still a continuum. This would result in a weaker material response and lower observed forces in the experiments. In addition, fracture and the creation of large cracks and voids within the material at the impact edge would cause the specimen to expand, potentially contributing to the non-uniform radial displacement and mushrooming effect seen in the DIC images.

Another hypothesis is that the Ti64 and In718 specimens experience significant temperature rise during the direct impact experiments, higher than what is predicted in the FEA simulations. If the temperature of the specimens were to significantly increase, the corresponding thermal softening would generate a weaker material response. This in turn would lower the force measured in the experiment, as well as increase the amount of mushrooming and non-uniform displacement compared to what would occur if the specimen temperature remained relatively low.

The simulated temperature rise along the axial length of the specimen is shown in Figure 4.85 for the Al2024 simulations using the AWG *MAT_224 material model, with the fraction of plastic work converted into heat taken to be $\beta = 0.4$. These simulations predict an uneven

temperature profile for the Al2024 specimens. There is a greater temperature rise at the impact edge compared to the rear edge, and a peak temperature increase of approximately 100°C for the 5.08 mm specimen and approximately 50°C for the 10.16 mm specimen at 14 μs after projectile impact.

The simulated temperature rise along the specimen length is shown in Figure 4.86 for Ti64 and in Figure 4.87 for In718. A value of $\beta = 0.8$ is used in the simulations for both materials. Figure 4.86(a) and Figure 4.87(a) shows the predicted temperature rise when the Ti64 and In718 AWG *MAT_224 material models are used. Recall that these material models did not match the experimentally observed specimen behavior. Therefore, the simulated temperature rise using the material model that gave the best match to the experiments for each material is also shown. Figure 4.86(b) shows the simulated temperature rise using the Ti64 scaled peak stress-to-yield stress curve, and Figure 4.87(b) shows the simulated In718 temperature rise using the quasi-static stress vs. strain curve.

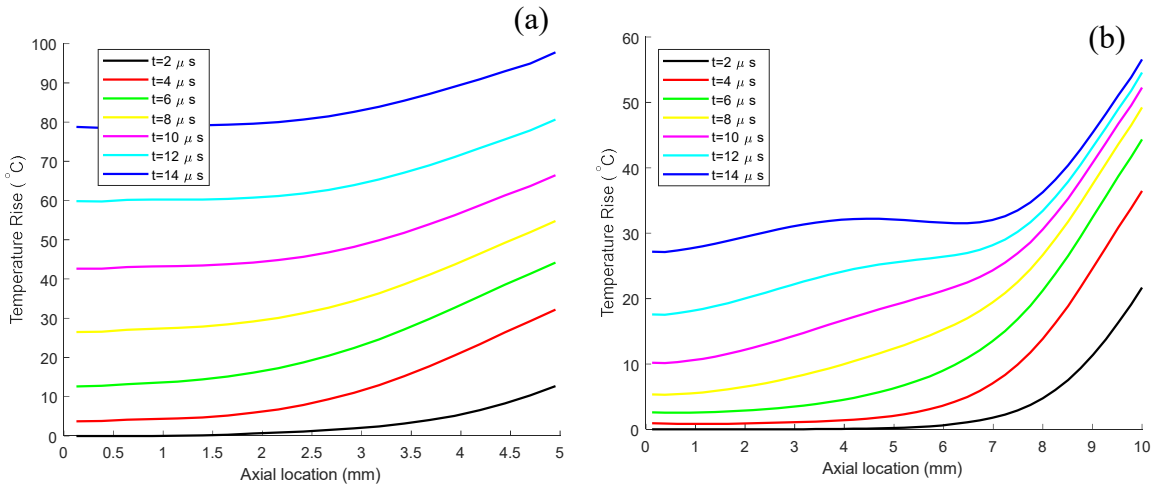

Figure 4.85 Simulated temperature rise along the Al2024 specimen length at various time steps after projectile impact for (a) 5.08 mm and (b) 10.16 mm specimen, using the Al2024 AWG *MAT_224 material model

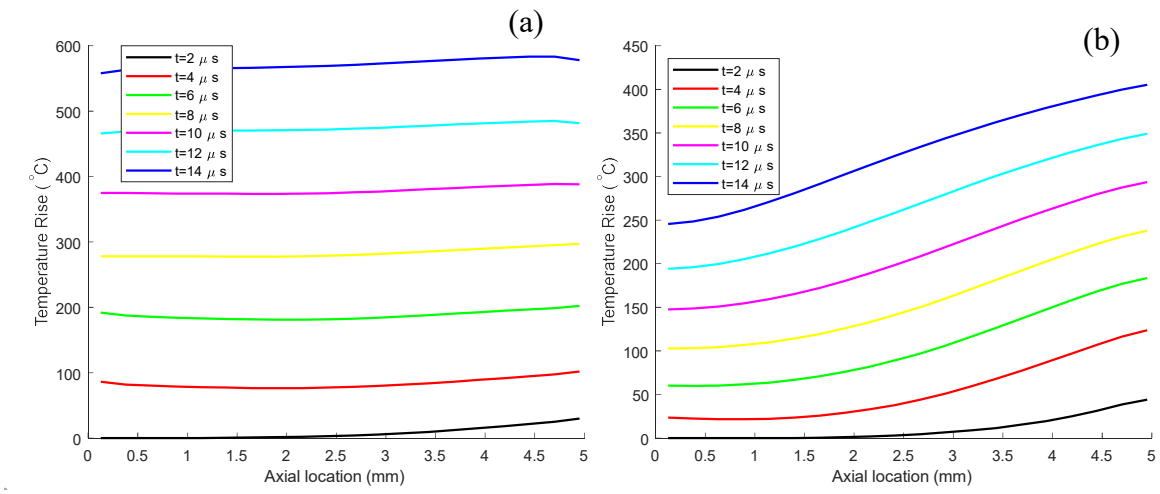

Figure 4.86 Simulated temperature rise along the 5.08 mm Ti64 specimen length at various time steps after projectile impact for (a) Ti64 AWG *MAT_224 material model and (b) Ti64 scaled peak stress-to-yield stress material model

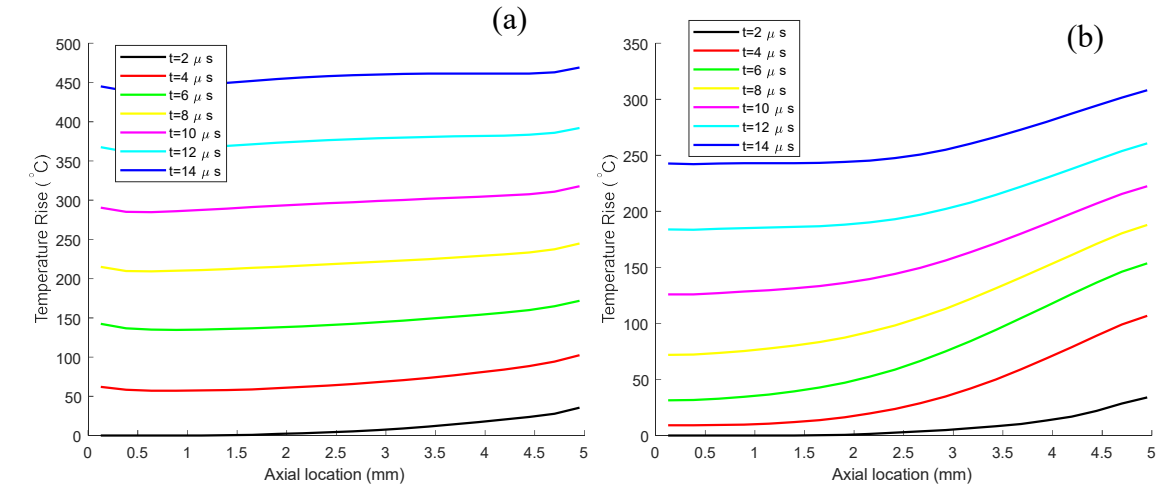

Figure 4.87 Simulated temperature rise along the 5.08 mm In718 specimen length at various time steps after projectile impact for (a) In718 AWG *MAT_224 material model and (b) In718 quasi-static model

The Ti64 and In718 simulations with the AWG *MAT_224 material models predict a fairly uniform temperature rise along the specimen length, and a peak temperature rise at 14 μs after impact of approximately 600°C for Ti64 and 450°C for In718. The Ti64 scaled peak stress-to-yield stress model in Figure 4.86(b) predicts a non-uniform temperature rise, as does the In718 quasi-static model in Figure 4.87(b). Both predict elevated temperatures at the impact edge compared to the rear edge, and a lower peak temperature rise compared to the *MAT_224 models.

Further experimental investigation with temperature measurements must be done in order to determine if any of the simulated temperature profiles match what physically occurs in the experiments.

Additionally, the simulated strain rate as a function of position along the axial specimen length can be determined. This is shown in Figure 4.88 for the Al2024 simulations with 5.08 mm and 10.16 mm long specimens, using the Al2024 AWG *MAT_224 material model. Figure 4.89 shows the simulated strain rate for Ti64, comparing both the Ti64 *MAT_224 and scaled peak stress-to-yield stress material models. The simulated strain rate for In718, using both the In718 AWG *MAT_224 and quasi-static material models, is shown in Figure 4.90.

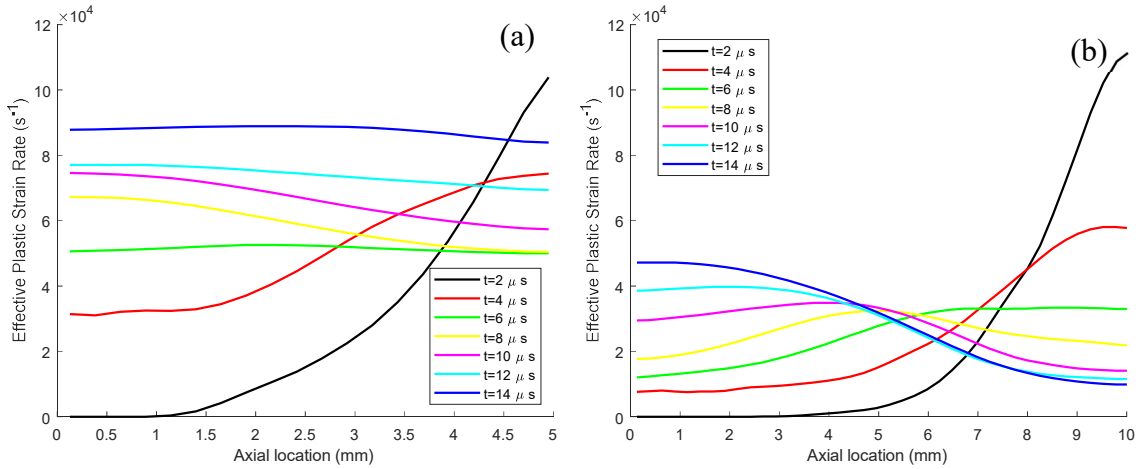

Figure 4.88 Simulated strain rate along the Al2024 specimen length at various time steps after projectile impact for (a) 5.08 mm and (b) 10.16 mm specimen, using the Al2024 AWG *MAT_224 material model

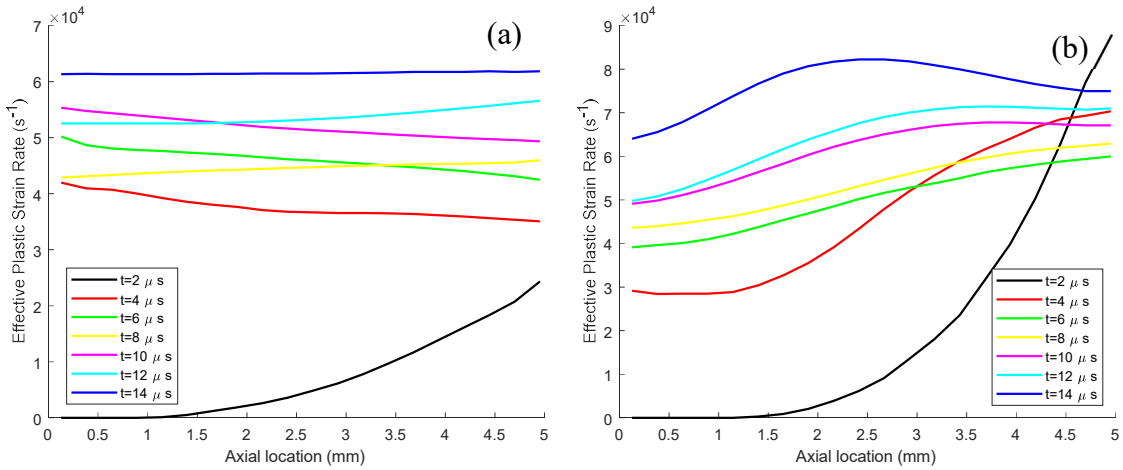

Figure 4.89 Simulated strain rate along the 5.08 mm Ti64 specimen length at various time steps after projectile impact for (a) Ti64 AWG *MAT_224 material model and (b) Ti64 scaled peak stress-to-yield stress material model

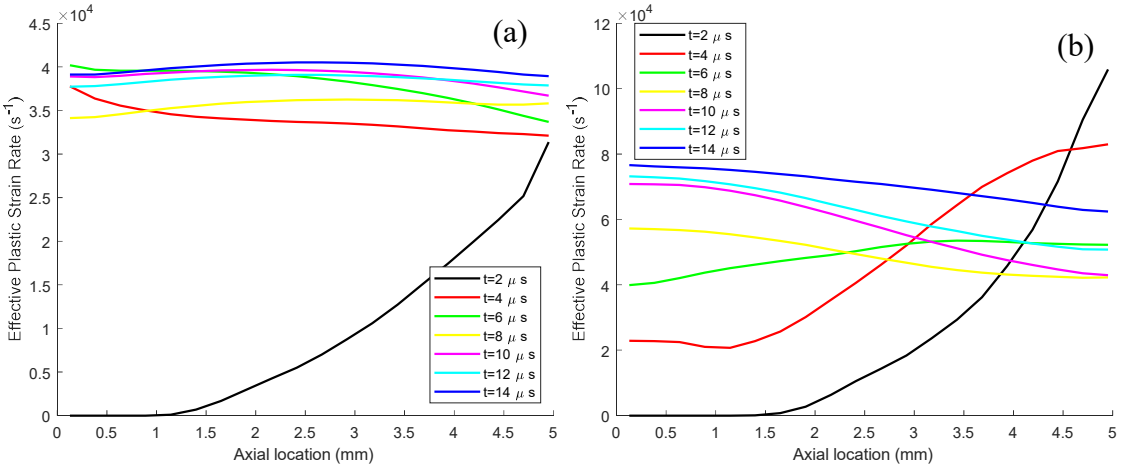

Figure 4.90 Simulated strain rate along the 5.08 mm In718 specimen length at various time steps after projectile impact for (a) In718 AWG *MAT_224 material model and (b) In718 quasi-static model

The Al2024 simulations for both specimen lengths predict very high initial strain rates at the impacted edge, upwards of 100,000 s^{-1}, even before the rear edge of the specimen has begun to deform. As the test progresses the strain rate for the 5.08 mm long specimen in Figure 4.88(a) is predicted to become more uniform. It is also predicted to steadily increase from a fairly uniform rate of approximately 45,000 s^{-1} (close to the nominal strain rate for this experiment) upwards to a strain rate of approximately 90,000 s^{-1}. The simulation of the 10.16 mm long Al2024 specimen in Figure 4.88(b) predicts that as the initial peak strain rate at the impact edge decreases, the strain

rate does not become uniform across the specimen length. Rather the strain rate at the rear edge of the specimen surpasses the strain rate at the impact edge at later time steps. This is likely due the unusual mushrooming behavior that occurs when these longer specimens are used, which causes rapid radial expansion at the rear edge of the specimen later on in the tests. After the initial peak due to the impact of the projectile, the strain rate for the Al2024 10.16 mm specimen remains lower than that of the Al2024 5.08 mm specimen. This is expected, as the nominal strain rate for the 10.16 mm specimen is lower (approximately 20,000 s^{-1}) than the nominal strain rate for the 5.08 mm specimens (approximately 40,000 s^{-1}). After the initial peak due to the projectile impact, some portion of the 10.16 mm specimen experiences a strain rate above this nominal value, while the remaining portion experiences a strain rate below the nominal value.

The simulation of Ti64 using the AWG *MAT_224 material model in Figure 4.89(a) predicts that the strain rate rises slightly faster at the impact edge but very quickly becomes uniform across the specimen length, in a range between 40,000 - 60,000 s^{-1} (close to the nominal strain rate). A very similar behavior is observed for the simulation of In718 using the AWG *MAT_224 material model in Figure 4.90(a). This is not unexpected, as the *MAT_224 models for both of these materials predicts fairly uniform deformation in Figure 4.65 and Figure 4.75, as well as uniform temperatures in Figure 4.86(a) and Figure 4.87(a). Therefore, it is not surprising that these same simulations predict a relatively uniform strain rate.

However when the material models that best match the Ti64 and In718 experimental data are used, the simulated strain rate along the specimen length is no longer uniform. The Ti64 peak stress-to-yield stress material model in Figure 4.89(b) predicts a high initial peak strain rate above 100,000 s^{-1} at the impacted edge. While the strain rate along the specimen length does decrease slightly and become more uniform as the test progresses, the impact edge continues to experience

a strain rate that is approximately 10,000 s^{-1} higher or more than the rear edge throughout the test. The simulation of In718 using the quasi-static material model in Figure 4.90(b) shows a similar peak strain rate on the order of 100,000 s^{-1} on the impact edge, before the strain rate becomes more uniform at strain rates between 40,000 - 80,000 s^{-1}. The strain rate is never entirely uniform across the specimen length, and actually becomes slightly higher at the rear edge than at the impacted edge later on in the test.

The above simulation analysis indicates that the specimen deformation during the direct impact experiments is likely highly complex, with the specimen experiencing different temperatures and strain rates at different locations along its axial length. It is doubtful that a simple material model utilizing a single stress-strain curve will be able to accurately capture the specimen behavior over this wide range of elevated strain rates (unless the material is relatively insensitive to the effects of the strain rate). Since multiple strain rates occur along the specimen length, these experiments could be used to determine the material behavior at multiple different strain rates from a single test.

The determination of localized strains (and therefore the strain rates) at various points along the specimen length requires higher quality DIC images. Higher quality images may also allow for the detection of premature fracture by identification of cracks in the images. Obtaining higher quality images requires brighter or more sophisticated lighting options than were available for these initial experiments. It may also be necessary to perform interrupted testing (where the projectile is stopped partway through the impact) so that the recovered specimen can be analyzed and the onset of initial fracture determined.

In addition, incorporating temperature measurements into future experiments can be used to determine the amount of thermo-mechanical temperature rise. The rise in temperature can then

be correlated to the amount of thermal softening that occurs. As shown in Figure 4.85 - Figure 4.87 it is likely that the specimen undergoes a non-uniform temperature rise. A non-contact temperature measurement technique such as those performed using as a commercial high-speed infrared imaging system [39] or infrared photon detectors [40] could be used.

To perform these additional experiments, a new high pressure gas gun has been designed to expand the testing capacity of the Dynamic Mechanics of Materials Laboratory at The Ohio State University. A generalized mock-up of this high pressure gas gun is shown in Figure 4.91. It consists of a 0.03 m^3 (30 liter) volume pressure vessel capable of generating pressures up to 1965 kPa, a 4.5 meter long barrel with a 50.8 mm diameter, and a vacuum containment chamber with internal volume of approximately 0.73 m^3 (0.9 m × 0.9 m × 0.9 m).

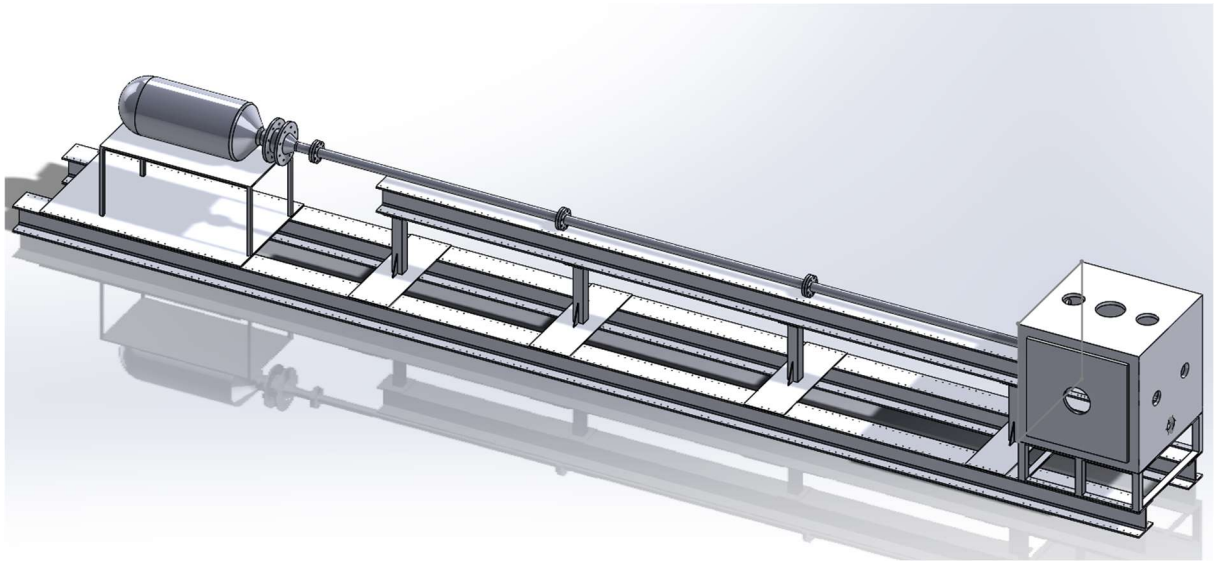

Figure 4.91 Schematic of new high pressure gas gun designed to expand the testing capabilities of OSU's Dynamic Mechanics of Materials Laboratory

The projectile velocity, v, that the gas gun can achieve is estimated through the following equations [41]:

$$v = \sqrt{\frac{p_1 aL}{m_p}} U_1, \tag{4-5}$$

$$U_1 = \sqrt{\frac{2C}{r(1+\delta)(\gamma-1)}\left[1 - \frac{1}{(1+r)^{\gamma-1}}\right] - \frac{2(1+W)}{1+\delta}} \ . \tag{4-6}$$

In Equation 4-5, p_1 is the downstream barrel pressure, a is the cross-sectional area of the barrel, L is the barrel length, m_p is the mass of the projectile, and U_1 is the dimensionless muzzle speed as defined by Equation 4-6. The dimensionless muzzle speed is defined by the following dimensionless variables: $C = \frac{P_o}{p_1}$ is the ratio of the initial pressure vessel pressure (P_o) to the down barrel pressure, $r = \frac{aL}{V_o}$ is the barrel volume divided by the pressure vessel volume (V_o), $\delta = \frac{\bar{m}_g}{2m_p}$ is the mean mass of the moving gas ($\bar{m}_g$) divided by the projectile mass, $\gamma = 1.4$ is the ratio of specific heats for air, and $W = \frac{w}{p_1 aL}$ where w is the work required by the gas in the pressure vessel to burst the diaphragm preventing the pressure vessel gas from expanding down the barrel. If an external valve or burst disk is used to release the gas down the barrel, it is assumed that $w = 0$.

Because a vacuum chamber is used, the downstream barrel pressure is very small, on the order of 0.7 kPa (approximately 0.1 psi). The above equations can be used to determine the relationship between the projectile velocity v, the projectile mass m_p and the initial pressure vessel pressure P_o of the designed gas gun (using the designed dimensions of initial pressure vessel volume V_o, barrel cross-sectional area a, and barrel length L). This relation is shown in Figure 4.92 below. Each line represents the relationship between the projectile mass and corresponding projectile velocity for a given initial pressure in the pressure vessel.

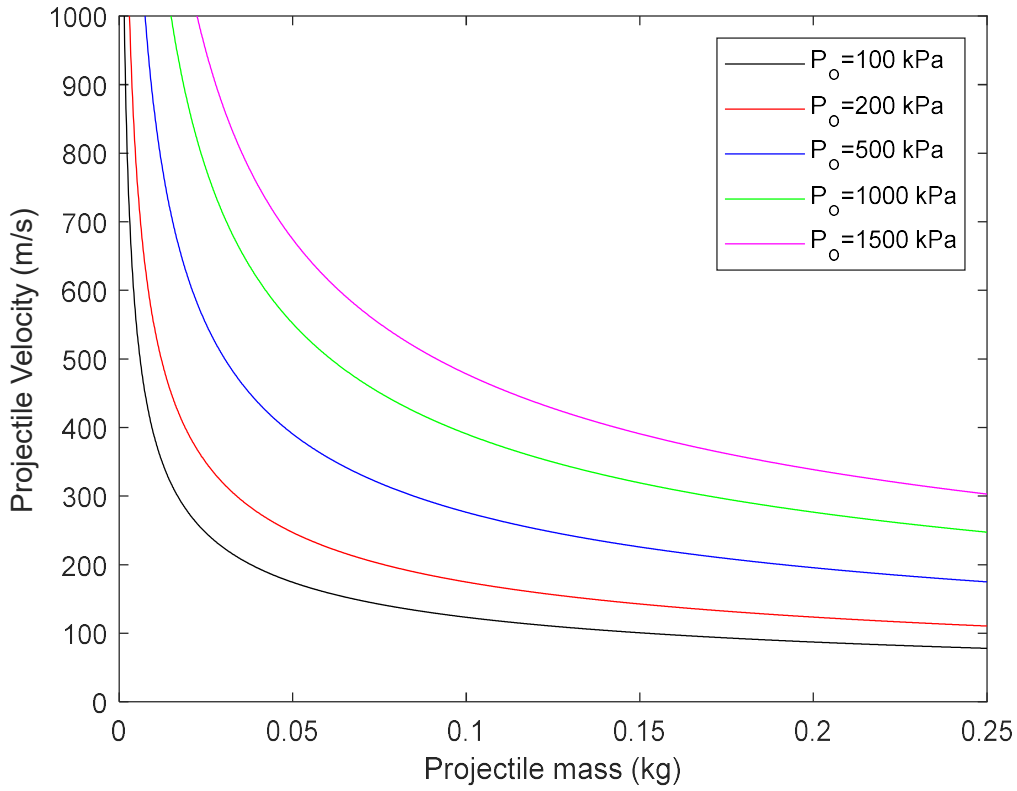

Figure 4.92 Comparison of projectile barrel exit velocity versus projectile mass for various firing pressures

Figure 4.92 shows that there are a wide range of predicted projectile velocities that the designed gas gun is capable of producing. Recall that for the direct impact experiments, the average projectile mass is 33.7 g and the average sabot mass is 79.7 g, for a combined total mass of 113.4 g. The average projectile velocity of the direct impact experiments is 215 m/s. It can be seen in the above figure that the new designed gas gun is capable of replicating the experiments conducted at the NASA Glenn Research Center using an initial pressure in the range of approximately 300 kPa.

Chapter 5 Summary and Conclusions

The equivalent plastic fracture strain of 2024 Aluminum, Titanium 6-Al 4-v, and Inconel 718 under stress states of in-plane biaxial tension and out-of-plane compression is determined at quasi-static loading rates. This is done through the development and implementation of novel small diameter backed punch tests. In addition, the deformation and stress-strain response of each of these materials is investigated at strain rates on the order of 20,000 - 40,000 s^{-1} through direct impact split-Hopkinson bar experiments. A combined experimental-numerical approach is used to investigate the material behavior. The experimental techniques are described in Chapter 2, and the numerical analysis utilizing the finite element analysis (FEA) software LS-DYNA is described in Chapter 3. The experimental and numerical results are presented and discussed in Chapter 4. The research has been funded by the FAA's Aircraft Catastrophic Failure Prevention Program, with the purpose of predicting and preventing uncontained airplane engine blade out events by developing accurate material deformation and fracture models. The results presented will be used to increase the accuracy of LS-DYNA *MAT_224 material models developed by the FAA Aerospace Working Group (AWG) for Al2024, Ti64, and In718.

5.1 Small Diameter Backed Punch Experimental Conclusions

Small diameter backed punch tests coupled with FEA analysis are used to determine the ductile fracture behavior of Al2024, Ti64, and In718 under combined biaxial in-plane tension and out-of-plane compression. Digital Image Correlation (DIC) is used in all experiments, and acoustic emissions sensing used in Al2024 elliptical backed punch tests to detect material fracture. A hemispherical shaped punch is used to induce equal amounts of in-plane tension along any two perpendicular in-plane axes, resulting in an average Lode parameter very close to $L_{avg} = -1$. An elliptical shaped punch is used to induce unequal amounts of in-plane tension, which results in the

average Lode parameter varying between $L_{avg} = -0.71$ in the unbacked tests to $L_{avg} = -0.28$ with the thickest (3.175 mm) backing plate. Backing plates are used to induce out-of-plane compression, which affects the value of the average triaxiality, σ^*_{avg}. The average triaxiality is approximately $\sigma^*_{avg} = -\frac{2}{3}$ when no backing plate is used and only in-plane biaxial tension is induced on the specimen. When a backing plate is used, the triaxiality increases with increasing backing plate thickness (increasing compression), and even reaches values close to or above zero in some experiments, which indicates a compression-dominated stress state.

The fracture strain values and corresponding average stress state parameters are reported in Chapter 4.1. The results show increasing fracture strain with increasing out-of-plane compression for each material. This trend is in line with previous work on ductile fracture, as compression tends to inhibit void growth and coalescence which leads to higher strains before fracture occurs. The Al2024 hemispherical punch tests and Al2024 elliptical punch tests show an increase in the fracture strain of 152% and 213%, respectively, between the unbacked tests (with no out-of-plane compression) and the tests with the thickest backing plates (highest amount of out-of-plane compression). The Ti64 hemispherical punch tests showed a 55.5% increase in the fracture strain between the unbacked and thickest backing plate experiments. For In718, the exact fracture strain in the backed tests could not be determined due to the extreme ductility of this material when out-of-plane compression is applied. However, a lower limit value of the fracture strain under these stress states is determined (below which the material is not expected to fracture), and In718 showed a 228% increase between the fracture strain in the unbacked tests and the lower limit fracture strain in the thickest backing plate experiment.

5.2 Direct Impact Split-Hopkinson Bar Experimental Conclusions

Direct impact split-Hopkinson bar (SHB) experiments are performed to investigate the plastic deformation behavior of Al2024, Ti64, and In18 at strain rates on the order of 20,000 s^{-1} - 40,000 s^{-1}. The material specimens experience non-uniform deformation and unequal forces at the impacted and rear specimen edges, making these experiments more difficult to analyze than conventional split-Hopkinson bar experiments. LS-DYNA simulations are performed, using various assumed plasticity models, and the force and deformed specimen shape is compared between these simulations and the experimentally measured values.

The analysis indicates that Al2024 does not exhibit significant strain rate hardening at these elevated strain rates when compared to the material behavior at quasi-static strain rates. This is in line with previous research that has shown Al2024 to be relatively insensitive to strain rate effects. The analysis also indicates that Ti64 exhibits a modest amount of strain rate hardening and that In718 exhibits very little or no strain rate hardening during the direct impact tests, which contradicts previous research on these materials. The fact that the Ti64 and In718 results are not in line with previous research, coupled with the difficulty of obtaining high quality data during the direct impact SHB tests, requires additional investigation. Possible reasons for this discrepancy are that these materials experience premature fracture or extremely high thermo-mechanical temperature rise. Either of these scenarios would cause a weaker aggregate material response during the experiments. The LS-DYNA simulations indicate the specimens experience non-uniform temperature rise along their axial length, with higher temperatures occurring on the impacted edge. These simulations also indicate that the specimens experience non-uniform strain rates, with the material experiencing strain rates in excess of 100,000 s^{-1} at the impact edge early on during these experiments.

5.3 Final Comments and Future Work

The experimental and numerical results presented here show the complexity exhibited by ductile materials. The fracture strain is clearly highly dependent on the applied state of stress, and the deformation at high strain rates is dependent on the combined effects of strain rate hardening, thermal softening, and localized material fracture. The data and analysis presented add to the understanding of how materials behave under complex conditions, and help in the development of more accurate material models in support of the FAA Uncontained Engine Debris Mitigation program. This in turn will enhance aircraft safety and protect human life.

Future work related to the backed punch experiments includes more in-depth analysis of the In718 experiments to determine the exact fracture strain instead of just the lower limit. This may include the use of acoustic emissions sensing during experiments loaded continuously until fracture for more accurate detection of initial fracture. Implementing advanced simulation techniques, such as adaptive remeshing, may circumvent the element distortion that occurs during the numerical analysis and aid in the determination of the In718 fracture strain. Additionally, elliptical backed punch tests on Ti64 and In718 should be carried out to determine the fracture strain of these materials under stress states of unequal in-plane biaxial tension coupled with out-of-plane compression.

Future work on the direct impact experiments includes repeating these experiments with brighter lighting so that higher quality DIC images can be obtained. This would allow for the detection of local strains and fracture along the specimen length with DIC. Additional experiments using shorter specimens can also be performed, in an attempt to mitigate the non-uniform deformation and force imbalance that occurs with the 5.08 mm and 10.16 mm long specimens. Interrupted experiments, where the projectile is stopped partway after impacting the specimen, can

be utilized to determine when fracture first occurs in these experiments. The implementation of thermal measurements, most likely using contactless methods such as infra-red imaging, can be incorporated into future experiments to determine the temperature rise in the specimens. To support these efforts, the design and construction of a new high pressure gas gun has begun to expand the testing capabilities of the Dynamic Mechanics of Materials Laboratory and enable future direct impact SHB experiments to be performed at The Ohio State University.

References

[1] National Transportation Safety Board. 1990. *Aircraft Accident Report-United Airlines Flight 232, McDonnell Douglas DC-10-10, Sioux Gateway Airport, Sioux City, Iowa, July 19, 1989*. Aircraft Accident Report NTSB/AAR-90/06.

[2] Frankenberger C.E., and Manchor J. 1999. *Engine Debris Penetration Testing*. Final Report to the U.S. Department of Transportation, Federal Aviation Administration, Report # DOT/FAA/AR-99/19.

[3] National Transportation Safety Board. 2019. *Left Engine Failure and Subsequent Depressurization, Southwest Airlines Flight 1380, Boeing 737-7H4, N772SW, Philadelphia, Pennsylvania, April 17, 2018*. Aircraft Accident Report NTSB/AAR-19/03.

[4] NTSB Aircraft Accident Investigate Update. Accident No. DCA21FA085. 3/5/2021. https://www.ntsb.gov/investigations/Pages/DCA21FA085.aspx

[5] Federal Aviation Administration (FAA), *§25.903 Engines*. 2011, pp. 135–139.

[6] Frankenberger, C.E. *Large Engine Uncontained Debris Analysis.* 1999. Final Report to the U.S. Department of Transportation, Federal Aviation Administration, *DOT/FAA/AR-99/11*.

[7] Menton, J., Gilbertson, D., and Iyer, K. 2021. *'I thought we were going down': United plane drops debris over Colorado, lands safely in Denver.* USA Today. [Online] 20th February. Available from: https://www.usatoday.com/story/travel/airline-news/2021/02/20/united-airlines-plane-debris-found-colorado-plane-lands-safely/4526251001/ [Accessed 1/28/2022]

[8] Hallquist, J.O. 2015. *LS-DYNA Keyword User's Manual, Volume II*.

[9] Seidt, J.D. 2010. *Plastic deformation and ductile fracture of 2024-T351 aluminum under various loading conditions*. Doctoral dissertation, The Ohio State University.

[10] Hammer, J.T. 2012. *Plastic deformation and ductile fracture of Ti-6Al-4V under various loading conditions.* Doctoral dissertation, The Ohio State University.

[11] Park, C.K., Kelly, C., Du Bois, P, Cordasco, D., and Kan, C.D. 2020. *Aluminum 2024-T351 Input Parameters for MAT_224 in LS-DYNA.* Final Report to the U.S Department of Transportation, Federal Aviation Administration, DOT/FAA/TC-19/41

[12] Lowe, R. L., Seidt, J. D., and Gilat, A. 2016. *Characterization of the Lode = -1 Meridian on the Al-2024 Failure Surface for *MAT_224 in LS-DYNA*. Proceedings of the 14th International LS-DYNA Users Conference.

[13] Hancock, J.W. and Mackenzie, A.C. 1976. *On the mechanisms of ductile failure in high-strength steels subjected to multi-axial stress-states.* Journal of the Mechanics and Physics of Solids, 24(2-3), pp.147-160.

[14] Mackenzie, A. C., Hancock, J. W., and Brown, D. K. 1977. *On the influence of state of stress on ductile failure initiation in high strength steels.* Engineering fracture mechanics, 9(1), pp.167-188.

[15] Rice, J.R. and Tracey, D.M. 1969. *On the ductile enlargement of voids in triaxial stress fields*. Journal of the Mechanics and Physics of Solids, 17(3), pp.201-217.

[16] Taylor, G.I. 1948. *The use of flat-ended projectiles for determining dynamic yield stress I. Theoretical considerations.* Proceedings of the Royal Society of London. Series A. Mathematical and Physical Sciences, 194(1038), pp.289-299.

[17] Kolsky, H. 1949. *An investigation of the mechanical properties of materials at very high rates of loading.* Proceedings of the physical society. Section B, 62(11), pp.676.

[18] Eldin, A.S., and Collins, S.C. 1951. *Fracture and yield stress of 1020 steel at low temperatures*. Journal of Applied Physics, 22(10), pp.1296-1297.

[19] Krafft, J.M., Sullivan, A.M., and Tipper, C.F. 1954. *The effect of static and dynamic loading and temperature on the yield stress of iron and mild steel in compression*. Proceedings of the Royal Society of London. Series A. Mathematical and Physical Sciences, 221(1144), pp.114-127.

[20] Johnson, G.R., and Cook, W.H. 1985. *Fracture Characteristics of Three Metals Subjected to Various Strains, Strain Rates, Temperatures, and Pressure*s. Engineering Fracture Mechanics, 21, pp. 31-48.

[21] Bao, Y. 2003. *Prediction of ductile crack formation in uncracked bodie*s. Doctoral dissertation, Massachusetts Institute of Technology.

[22] Bao, Y., and Wierzbicki T. 2004. *On fracture locus in the equivalent strain and stress triaxiality space.* International Journal of Mechanical Sciences, 46, pp. 81-98.

[23] Barsoum I., and Faleskog J. 2007 *Rupture mechanisms in combined tension and shear-Experiments*. International Journal of Solids and Structures, 44, pp. 1768-1786.

[24] Wierzbicki, T., Bao, Y. Lee, Y.W. and Bai, Y. 2005. *Calibration and evaluation of seven fracture models. International Journal of Mechanical Sciences, 47(*4-5), pp.719-743.

[25] Barsoum, I. 2008. *The effect of stress state in ductile failure*. Doctoral dissertation, KTH.

[26] Hopperstad, O.S., Børvik, T., Langseth, M., Labibes, K., and Albertini, C. 2003. *On the Influence of Stress Triaxiality and Strain Rate on the Behaviour of a Structural Steel. Part I. Experiments.* European Journal of Mechanics A/Solids, 22, pp. 1-13.

[27] Børvik, T., Hopperstad, O.S., and Berstad, T. 2003. *On the Influence of Stress Triaxiality and Strain Rate on the Behaviour of a Structural Steel. Part II. Numerical Study*. European Journal of Mechanics A/Solids, 22, pp. 15-32.

[28] Bai, Y., and Wierzbicki, T. 2010. *Application of extended Mohr–Coulomb criterion to ductile fracture.* International Journal of Fracture, 161, pp. 1-20.

[29] Mohr, D., and Marcadet, S.J. 2015. *Micromechanically-motivated phenomenological Hosford–Coulomb model for predicting ductile fracture initiation at low stress triaxialities.* International Journal of Solids and Structures, 67-68, pp. 40-55.

[30] Gilat, A., and Matrka, T.A. 2011. *A new compression intermediate strain rate testing apparatus.* Dynamic Behavior of Materials, 1, pp. 425-429.

[31] Dharan, C.K.H., and Hauser, F.E. 1970. *Determination of stress-strain characteristics at very high strain rates.* Experimental Mechanics, 10, pp. 370–376.

[32] Couque H. 2014. *The use of the direct impact Hopkinson pressure bar technique to describe thermally activated and viscous regimes of metallic materials*. Philosophical Transactions of the Royal Society A: Mathematical, Physical and Engineering Sciences, 372(2023), p.20130218.

[33] Liutkus, T. J. 2014. *Digital Image Correlation in Dynamic Punch Testing and Plastic Deformation Behavior of Inconel 718.* Doctoral dissertation, The Ohio State University.

[34] C. Solutions. 2018. *Inc. Correlated Solutions.*

[35] Sutton, M. A., Orteu, J. J., and Schreier, H. 2009. *Image correlation for shape, motion and deformation measurements: Basic concepts, theory and applications*. Springer Science & Business Media.

[36] Haight, S., Wang, L., Du Bois, P., Carney, K., and Kan, C.D. 2016. *Development of a titanium alloy Ti-6Al-4V material model used in LS-DYNA*. Final Report to the U.S Department of Transportation, Federal Aviation Administration, DOT/FAA/TC-15/23

[37] Sutton, M.A., Gilat, A., Seidt, J., Rajan, S. and Kidane, A., 2018. *Full field deformation measurements in Tensile Kolsky Bar experiments: studies and detailed analysis of the early time history*. Journal of Dynamic Behavior of Materials, 4(1), pp.95-113.

[38] Pereira, J. M., Revilock, D. M., and Ruggeri, C. R. 2020. *Impact Testing of Inconel 718 for Material Impact Model Development*. No. GRC-E-DAA-TN76157.

[39] Smith, J. L. 2019. *Full-Field Measurement of the Taylor-Quinney Coefficient in Tension Tests of Ti-6Al-4V, Aluminum 2024-T351, and Inconel 718 at Various Strain Rates*. Doctoral dissertation, The Ohio State University.

[40] Hodowany, J., Ravichandran, G., Rosakis, A. J., and Rosakis, P. 2000. *Partition of plastic work into heat and stored energy in metals.* Experimental mechanics, 40(2), pp. 113-123.

[41] Denny, M., 2013. *Gas gun dynamics*. European Journal of Physics, 34(5), p.1327.